A Reproduced Copy

Advanced Turboprop Vibratory Characteristics

Final Report

A.V. Srinivasan
G.B. Fulton

United Technologies Research Center
East Hartford, CT 06108

Contract NAS3-23533
April 1984

National Aeronautics and Space Administration

Lewis Research Center
Cleveland, Ohio 44135
AC 216 433-4000

1. Report No	2. Government Accession No.	3 Recipient's Catalog No
NASA CR 174708		

4. Title and Subtitle	5. Report Date
Advanced Turboprop Vibratory Characteristics	April 1984
	6 Performing Organization Code

7 Author(s)	8 Performing Organization Report No
Srinivasan, A. V., and Fulton, G.B.	R84-956627-1
	10 Work Unit No

9 Performing Organization Name and Address	11. Contract or Grant No
United Technologies Research Center East Hartford, CT 06108	NAS3-23533
	13 Type of Report and Period Covered
12 Sponsoring Agency Name and Address Science & Technology Section, MS500-305 NASA Lewis Research Center 21000 Brookpark Road, Cleveland OH 44135	Final
	14 Sponsoring Agency Code

15 Supplementary Notes

Point of Contact: Robert Kielb, NASA/Lewis Research Center
Cleveland, Ohio 44135 (216)-433-4000 x5104

16 Abstract

The results of an experimental program carried out on an assembly of SR5 advanced turboprop blades to develop a structural dynamic data base for swept props are reported. The data was gathered through a series of tests conducted in a vacuum at speeds up to 9000 rpm. Steady state blade deformations under centrifugal loading as well as vibratory characteristics of the rotor assembly have been measured and compared with analytical results supplied by NASA. Vibration was induced through a system of piezoelectric crystals attached to the blades. Data reduction procedures developed at UTRC were used to provide deformation, mode shape, and frequencies of the assembly at predetermined speeds.

17 Key Words (Suggested by Author(s))	18 Distribution Statement
Prop-fan, Vacuum spin test, Centrifugal deformation, Blade frequency response, Blade mode shape, Swept blades. Coupled vibration.	Unclassified/Same as Report. In accordance with distribution lists furnished by the NASA Contracting Off. or Proj. Mgr.

19 Security Classif. (of this report)	20 Security Classif. (of this page)	21 No of Pages	22 Price*
Unclassified	Unclassified	80	

* For sale by the National Technical Information Service, Springfield, Virginia 22151

NASA-C-168 Rev. 10-75

Advanced Turboprop Vibratory Characteristics

TABLE OF CONTENTS

TABLE OF CONTENTS (Cont'd)

ACKNOWLEDGEMENTS

The authors would like to thank Mr. D. G. Cutts for his efforts in formulating the test program, and Dr. R. A. Arnoldi for sharing his valuable experience in turbomachinery dynamics and providing data reduction support and guidance. The assistance of Mr. R. J. Haas and Dr. K. A. Stetson in setting up and interpreting the optical data is greatly appreciated. The efforts of Mr. J. Zucker in assembling the test hardware and assisting in the experimental activity contributed to the success of the program. Finally, thanks to Mrs. C. K. Obee for her assistance in the preparation of the report.

The authors would also like to express their appreciation to R. Kielb, the NASA Program Manager, and C. Lawrence, for their support in supplying the results of their NASTRAN analyses which provide the basis for comparison with experimental data.

I. INTRODUCTION

Prop-fan propulsion promises large reductions in fuel burned compared to advanced turbofan propulsion, with corresponding reduction in direct operating costs. Current predictions (Ref. 1) indicate that for a 120 passenger transport aircraft in the 1990's at a cruise Mach number comparable to that attainable from turbofans, a single rotation Prop-fan powered aircraft will burn 20% less fuel and result in a reduction of 10% in direct operating costs. Potentially greater benefits are expected with counter rotating Prop-fans which are predicted to burn 31% less fuel, yielding a 14% reduction in direct operating costs. Technology advances in several diverse fields are essential if these predicted gains in performance are to be realized. Prop-fan use is contingent upon advances in aerodynamics, acoustics, power transmission, and structural dynamics technologies.

The present report is a summary of results of a series of experiments carried out in the UTRC vacuum spin facility. Interest in the experimental program was raised, when differences between frequencies calculated by different finite element codes could not be resolved. Additionally, the calculated frequencies did not agree with the corresponding frequencies measured at zero speed. The test program was oriented towards acquisition of both steady and vibratory data at speeds which could be readily compared with analytical results.

Compared to conventional propellers, Prop-fan blades are thin and highly swept back which give rise to large bending and twisting deformations and complex vibratory characteristics. In addition to a strong correlation between aerodynamic performance and centrifugal deformation, the aeroelastic stability and forced response in the transonic Mach number range at which the blade operates is dependent upon both frequency and vibratory mode shape.

The test results reported herein present both steady deformations and vibratory frequencies and mode shapes of a model prop-fan in a vacuum centrifugal environment. Several unique measurement techniques were exploited during the program including determination of steady blade deformation by angular deflection of a laser beam reflected from mirrors bonded to the blades, and direct tip deflection measurements with high speed strobe photography. Use of piezoelectric crystal excitation provided smooth sinusoidal blade excitation of the assembly at arbitrary amplitude and interblade phase angle in the vacuum. Comparison between test results and corresponding analytical predictions is made and discussed.

Support for these tests was made through the NASA Advanced Turboprop project office as part of the overall program to develop turboprop technology.

II. SUMMARY

An experimental program was carried out on an assembly of SR-5 advanced turboprop blades to develop structural and dynamic data for swept props. The data was gathered through a series of tests conducted in vacuum at speeds up to 9,000 RPM. Steady state blade deformations under centrifugal loading were measured with a system comprising an externally mounted laser and blade mounted mirrors as well as by direct strobe photos of the blade tips. Vibratory characteristics of the system have been measured and compared with analytical results. Vibration was induced through the UTRC developed system of piezoelectric crystals attached to the blades. Data reduction procedures also developed at UTRC were used to provide deformation, mode shape, and frequencies of the assembly at predetermined speeds.

III. PROGRAM OBJECTIVES

This research program pertained to developing structural data aimed at serving the design process of prop-fans. Steady state blade deflections as well as vibratory characteristics of prop-fans were determined over a speed range from tests conducted in a vacuum on a model SR-5 prop-fan rotor. The specific objectives were to:

1. Measure the centrifugally induced steady blade twist and deflection up to the mechanical design speed of 9,000 RPM.

2. Measure frequency of the first five normal modes of vibration as it varies with speed.

3. Verify via measurements if the blades are mechanically coupled through the hub during vibration and determine the character and extent of that coupling.

4. Compare the experimental results with corresponding analytical predictions supplied by NASA.

The overall goals of the program were to (a) assess the extent of correlation between finite element analysis and corresponding test results, and (b) determine the extent of mechanical coupling among the blades through an examination of the response of the assembly in its system modes.

IV. TEST FACILITIES

The tests were carried out in the UTRC high speed spin facility, a 10 ft diameter by 3 ft high vacuum chamber (fig. 1). This chamber is a fabricated weldment with 3/4 inch thick shell and 2 inch thick top and bottom cover plates. A 3 inch thick ring 94 inches in diameter and 34 inches high is positioned inside the chamber to contain fragments from any unanticipated failures. The vacuum chamber is mounted on a platform 4 feet above the floor with the vertical axis drive system mounted on the bottom plate. This arrangement allows unobstructed visual access to the test piece from the top.

The drive system (fig. 2) is composed of a main drive shaft supported on two duplex ball bearings. At the top of the drive shaft in the plane of the chamber floor, is a squeeze film damper to control rotor vibrations during excursions through resonant speeds. At the lower end of the drive shaft is a flexible coupling which connects to an 8 inch Barbour-Stockwell air turbine, controlled by an electro-pneumatic servo throttle valve to within ±0.5% of the specified full speed. A safety interlock system protects against any loss of oil pressure, oil flow, or oil level in the reservoir. A remotely operated turbine brake control will function in the event of a power failure. An overspeed trip solenoid air valve will shut off the drive air when the selected value of maximum speed is attained. A balance air regulator allows a percentage (ten percent maximum) of the drive air pressure to support and unload the turbine bearings.

The vacuum pump system will evacuate a volume of 200 cubic feet to a vacuum of 20 microns or less with specified leak rate of less than 1.2×10^{4} standard cc/sec of helium. The pump system is sized to achieve this vacuum level in appropriately 20 minutes. An automatic vacuum valve will isolate the spin chamber and prevent loss of its vacuum should a power failure occur. The bottom flange of the turbine is fitted with a magnetic pick up and 60 tooth gear to provide the signal to the controller. Below the turbine through another flexible coupling, the 100 channel Electrotech slip ring is mounted. The slip ring is rated at 12,000 RPM and has specified max noise level of 6 mΩ at 100 ma current at 9,000 RPM.

V. DESCRIPTION OF ROTOR AND BLADE GEOMETRY

The test rotor comprises Ti 6-4 prop-fan blades mounted on a steel hub which retains the blades in the centrifugal field and has provision for fixing the pitch angle of the blades (fig. 3). The SR-5 rotor designed and fabricated by Hamilton-Standard Division of United Technologies Corporation as a 10 bladed rotor has undergone extensive wind tunnel testing under a variety of conditions to measure both its aerodynamic and structural characteristics. This report covers a five bladed version of the SR-5 rotor (fig. 4), with blades set at the nominal cruise flight pitch angle of 58.5 degrees at a reference radius of 3/4 span. Table I is a summary of the significant airfoil geometric parameters more completely given in Ref. 2. The individual blades were moment weighed after the instrumentation and leadwork was installed and then mounted in the hub in a sequence to minimize initial imbalance. Table II summarizes the results of this attempt to minimize unbalance.

The analytical results to which the test data is compared were obtained by NASA using the NASTRAN finite element model. This analytical program described in detail in Ref. 3 modeled the blade with 881 TRIA 3 elements. Both linear and non-linear solution procedures were used to properly simulate the large steady deflections and the stiffening effect of the centrifugal field. Vibratory modes of a single blade were calculated at several speeds with the NASTRAN. Additional details of the analytical modeling are given in Appendix IV.

The blade/rotor axis system is shown in Figure 5; the X-axis is coincident with the rotor axis (positive aft), Y is radial and coincident with center of the blade pitch change axis (positive outward) and Z is perpendicular to the XY plane (positive in the direction of rotation to complete the right hand coordinate system). Figure 6 shows the grid breakup used for the 517 node NASTRAN model. For purposes of surface identification, the pressure or face surface is the surface facing in the positive Z direction, and the suction or camber surface faces the negative direction.

VI. INSTRUMENTATION

A. Steady Centrifugal Blade Deformation

The technique of measuring propeller deflections by means of reflection from mirrors bonded to the blade surface was first reported in this country in NACA report No. 644 of January 18, 1938, Ref. 4. Realization of the full potential of this technique required development of an intense narrow beam light source and adhesives with high strength so that the mirrors would remain attached to the blade in the severe environment. Readily available and inexpensive lasers and epoxy adhesives led to the independent development and refinement of this technique reported in references 5 and 6. The method of using reflection of a laser beam from mirrors bonded to the blade was thus a logical choice to determine the complex deformation patterns of the prop-fan.

The location of the mirrors mounted on the blades is shown in Figure 7 and the schematic arrangement of the laser/mirror shown in Figure 8. One blade (S/N 10) has the full array of 11 mirrors as shown in the figure; each of the other four blades in the rotor have a single mirror at the A-2 location. Alignment and bonding of the mirrors were carried out with the blades mounted in the hub at the specified pitch angle, and the hub mounted in the spin-rig. The intense narrow beam light source is provided by a Hughes, Series 4000 HeNe laser. The first step required that the laser which was secured to an alignment frame mounted to the rim of the rig, be aligned so its axis is radial. The optical bench (fig. 9) assures that the two beam splitting and final fully reflective mirrors are fixed so that the incident beams are vertical along a radial line and at the specified radii (7.0 inches (17.78 cm), 9.5 inches (24.13 cm), and 11.5 inches (29.2 cm)). The D row of mirrors was added subsequent to fabrication of the mirror fixture, consequently, the laser/ mirror assembly had to be moved radially inward until the innermost beam engaged the D mirrors at 3.75 inches (9.53 cm) for measurements of these deflections. During the process of bonding the mirrors to the blades, the intensity of the laser was reduced by insertion of a 99% neutral density filter into the beam to protect personnel. The radial position of the mirrors on the blade was established by shimming the blade radially outward with Teflon shims between foil root and hub, then slowly rotating the blade through the incident beams and tracing the path of the spot with a pencil across the top surface. Cardboard templates were cut to match the arc in the blade surface and chordwise distances of 10, 50 and 90% for the A row; 10, 50 and 85% for the B row; 10, 40 and 85% for the C row; and 10 and 90% for the D row, were marked out along this arc. The template was then used to locate the chordwise position of the center of each mirror on the surface of the blade. A

1cm x 1cm Teflon block taped to the blade, supports the mirror epoxy mass during the time the epoxy is hardening (fig. 10). 3mm (1/8 inch) diameter x 1mm (0.04 inch) thick mirrors are supplied by Edmund Scientific Company. Actual mounting of the mirror was achieved by moving the rotor until the specified location is centered under a laser beam. A small bead of room temperature curing epoxy was placed on the bottom surface of the mirror and the mirror was then set on to the blade. After the epoxy hardened, a smooth fairing of epoxy was built up around the mirror to provide additional strength. This method of mounting the mirrors proved extremely effective and durable throughout the test program and no mirrors were lost due to centrifugal or vibratory forces.

Direct photographs of the blade tips to provide an independent displacement measurement was possible because of the availability of a high intensity short duration spark gap flash unit and the UTRC designed and fabricated digital phase shifter which operated from the 1 per rev and 60 per rev signals available from the spin rig drive shaft. A simple calculation shows that at maximum speed of 9,000 RPM, the blade tip will move only approximately 0.003 inches during the 1/4 μsec flash duration resulting in sharp, well-defined photographs.

For the high speed tip photographs, a 12 inch (30.5cm) x 12 inch (30.5cm) front surface mirror was placed at a 45 degree angle with its plane normal to a radial plane centered on the blade Y-axis plane (figs. 11 and 12). A small secondary lens assembly was located between the mirror and blades to bring the hub pointer and reference mark to focus at the same radius as the blade tips. The source of illumination is a 1/4 μsec air gap spark unit, located outside the vacuum chamber triggered by a UTRC designed digital phase controller driven by 1 per rev and 60 per rev signals from the drive shaft. The phase controller permits control of the trigger signal to illuminate any point on the circumference of the rotor.

The camera, a 35mm SLR, was mounted outside the vacuum chamber along side the flash unit.

B. Dynamic Instrumentation

The blade mounted dynamic instrumentation comprises two parts: the piezoelectric crystals used to induce vibration in a desired mode, and resistance strain gages to define blade response. Figure 13 shows the strain gage and crystal locations, and Table III gives the relationship between the strain gage locations and the corresponding NASTRAN grid number and coordinate. Crystal location was based on bench test experiments to give good vibratory response of the blades in their first five normal modes. Two lead zirconate-titanate crystals paralled electrically to increase force input were used to excite each blade. The crystals, Type G1356 supplied by Piezo Electric Products were 1.00 x 0.5 x 0.010 inches. Development of the crystal excitation technique is described in reference 7. Strain gage locations were chosen

on the basis of analytical stress distributions derived from NASTRAN (ref. 3) for the first five vibratory modes.

The two blades chosen to have the extensive instrumentation (blade S/N 2 with 15 strain gages, and blade S/N 10 with 11 mirrors) were selected on the basis of their having average frequencies as measured on the bench.

Micro Measurements constantan foil EA-06-062AP-120 single element strain gages, and EA-06-062RB-120 Rosettes were used in the program. Blade surface preparation was in accordance with Micro Measurements recommended procedures prior to bonding the gages with M Bond 610 adhesive. Because the blade itself forms one leg of the crystal excitation circuit, a spot conductive adhesive was used along with conventional epoxy to attach the crystals.

C. Blade Excitation, Data Acquisition Systems

A schematic of the overall blade excitation and data acquisition system is shown in Figure 14. The three leads from each strain gage (two signal and an independent excitation lead for temperature compensation) were routed through the center of the drive shaft and turbine to the 100 channel Electro Tech slip ring rated at 6 mΩ maximum noise at 100 ma current at 9,000 RPM. Bridge completion was accomplished with precision resistors mounted in terminal strips adjacent to the slip ring. Bridge excitation and signal conditioning made use of the front end portion of an Analog Data Recording System (ARES). This is a semi-portable system for the automatic acquisition of dynamic test data with oscillatory frequency rates from zero to 20 kHz. A maximum of 28 analog signals can be processed. Each channel incorporates independent signal conditioning and amplification. The signal conditioners are specifically designed for strain gage type transducers and provide regulated excitation up to 10 volts. The amplifiers provide voltage amplification of 1, 10, 100, or 1,000, and are each equipped with low pass signal filters with roll off frequencies of 10Hz, 100Hz, 1kHz, 10kHz, and 100kHz. Signal monitoring can be achieved through a single channel selectable digital display readout which includes RMS measurement capability for averaging dynamic signals.

Data recording was by the computer controlled UTRC Aeromechanical Transient Logging System (ATLAS) which prepares, digitizes and records the analog signal from the strain gages. For the present tests, sampling rates were chosen to record between 50 and 80 complete cycles of the mode of interest. Reduction of the data is discussed more fully in the section on test procedures (VII).

Also shown in Figure 14 is a schematic of the controls for the piezoelectric crystal blade excitation system. The UTRC designed and fabricated main control provides for independent level and phase control of the voltage to each of the five blades. This independent control of the phase angle between blades permits the rotor to be driven in any given circumferential wave (nodal diameter) pattern, and allows arbitrary selection of the direction of wave travel relative to the rotor. The control is driven with a Hewlett Packard HP3311A signal generator which allows fine frequency control with external DC voltage input. The five outputs are routed through the slip ring to the blade mounted crystals.

VII. TEST PROCEDURE

A. Steady State Deflections

Prior to recording data from the surface mounted mirrors, the initial positions of the spots on the marked screen were recorded by turning the rotor by hand with the chamber evacuated and marking the reflections from each mirror on the screen. A photograph of the marked screen was made and served as the zero speed reference location for each mirror. The rotor was then accelerated, allowed to stabilize at each required speed, and a photograph of the reflections was made. The exposure was chosen to give 10 to 20 repetitions of each reflection. Figure 15 shows a typical photograph of the screen which also shows the scales needed for length calibration and a repeating tachometer for measuring the speed. This procedure served well up to a certain speed beyond which most of the reflections had passed outside the field of the window and thus could not be recorded. Several attempts were made to rebond the mirrors to the blades to permit greater range of travel but the combination of blade bending, twisting angles, and the plane of the rotor relative to the window resulted in spot deflections at 9,000 RPM which exceeded the 12 inch diameter of the viewing window. To provide positive spot identification and eliminate ambiguity from spot crossings on the still photographs at increasing speeds, a real time video recording was made of a slow acceleration, and from this a continuous tracing of each spot (fig. 16) as a function of speed was prepared. Figure 16 shows the trajectories of the midchord tip mirror reflections from all five blades which represent a measure of how well the blades match each other in their twist. The observation that θ_Z for blade S/N 10 is larger than for the other four blades is attributed to the extra mass of the eleven mirrors and epoxy adhesive on that blade. The data points shown in Figure 16 at even 1,000 RPM increments are for convenience in comparing deflections among the blades, the shape of each curve, however, is determined by 6 to 10 speed points.

Data reduction was achieved by projecting the negatives on a microfiche reader and measuring relative spot displacements, which were then simply converted to angular displacements of the blade. Since the mirrors in general are situated a distance away from the blade Y-axis there is coupling between the measured Y and Z rotations. The curves for all the mirror data are shown in Appendix I, resolved into blade Y and Z coordinates and are thus directly comparable to similar quantities calculated from NASTRAN.

To obtain photographs of the tips, the rotor was brought up to a given speed and stroboscopically illuminated with a multiple flash strobotach triggered by the once per rev signal from the drive shaft. A digital phase shifter was used to adjust the time of flash relative to the once per rev pulse, thus the rotor could be "stopped" at any angular location. Each blade was lined up visually using the hub reference mark relative to the hub pointer. When the correct alignment had been achieved, the strobotach was removed from the circuit and replaced with the single pulse high intensity Microflash 599-11 light source and driver. Recording was achieved by opening the camera shutter, pulsing the flash unit and closing the shutter. In this manner, two independent photographs of each of the five blades were taken at each of six speeds.

Data reduction was accomplished by projecting the negatives onto vellum at an overall magnification of approximately 4X. The position of the blade leading and trailing edges was marked as were the position horizontal and vertical fixed reference lines. Blade deflections were determined by the variations in position from the reference marks.

It was determined that the circumferential, w, displacements are subject to significantly more scatter and error than the axial, u, displacements, and θ_Y rotations. Despite the availability of a reference at the hub, an error in determining the hub position was magnified by the ratio of tip to hub radii (a factor of approximately 3). Consequently the inherent scatter is magnified. For tip twist and axial displacements, however, the tip photos yielded satisfactory results.

B. Dynamic Testing

Prior to the determination of vibratory characteristics of the assembly at speed, the blades were individually characterized with the UTRC Genrad Modal Analysis System. With the hub clamped nose down on a granite block, each instrumented blade was mounted in its hub port and forced radially outward with a bolt between base and hub to simulate centrifugal loading. System output to force input ratio was recorded up to 1kHz for each of the 27 strain gages by means of an instrumented hammer.

The instrumented hammer is generally used to excite a structure transiently for use in modal analysis systems which employ the FFT techniques to determine modal parameters. This impulsive force technique utilizes short transient force inputs (with corresponding broad-band spectra) to excite all the modes in the structure simultaneously. A force transducer is mounted on the hammer and the strain gages are located on the blades at the specified locations. The structure is excited at a multiplicity of predetermined locations using the hammer and the response is picked up by the strain gages. The two transient time histories, i.e., force and response, are automatically

digitized and then Fourier transformed by a minicomputer to yield input and output spectra. The resultant ratio of the output to input spectra is the desired transfer function. By repeating this process at a number of points on the structure, the mode shapes at individual resonant frequencies can be determined. The results from these tests yielded the modal amplitude, frequency, and phase data for all the strain gages on all the blades, which provide the basis for comparison with corresponding results at speed.

For tests at speed, the rotor was mounted in the vacuum spin rig, and strain gages and crystals connected through the slip ring to the data system and excitation control respectively. During the initial functional check of the system at low speed, it was determined that an excessive amount of crystal excitation voltage was appearing on the strain gage channels, resulting in unacceptable crosstalk. The source of this crosstalk is discussed below.

During the process of routing the strain gage leadwires and crystal excitation wires from the slip ring up through the turbine and prop fan spindle, the small size of the spindle bore (3/8 inch diameter) precluded the possibility of properly isolating or shielding the 81 strain gage wires and the 5 crystal excitation leads. Consequently the crystal excitation wires were embedded within the strain gage lead bundle, and are constrained to 3/8 inch diameter for a length of approximately 30 inches. This arrangement resulted in unacceptably high crosstalk voltages appearing on the strain gage signal leads. Thus, the close proximity of the excitation and strain leads over a significant length, lack of isolation of shielding, the relatively high impedance of the strain gage circuit (120 Ω), and high crystal excitation voltages, generally between 50 and 100 volts peak to peak were identified as the important factors contributing to this problem. Further, the crosstalk is sinusoidal at or very close to the response frequencies of the blades and thus is not subject to filtering. The crosstalk was evaluated by driving the crystals at frequencies away from blade resonant frequencies so that physical blade response would be low and the signals appearing on the strain gage channels represent actual capacitively coupled crystal excitation. The effects of the crosstalk were by-passed by recording the decay of free vibrations and reducing data by a time domain analysis as outlined in Appendix III, and reference 8. To obtain a data record with the rig stabilized at a specified speed, the crystals were energized at a specified amplitude and interblade phase angle. To find the system frequency, a responsive strain gage channel was monitored visually on an oscilloscope as the excitation oscillator was swept slowly around the frequency of interest. Away from the resonant frequency the monitor signal was a constant amplitude sinusoid representing the crosstalk amplitude, as resonance was approached the amplitude increased to a maximum. When it was visually determined that the blade response was at a maximum, the excitation was switched off and data recording started simultaneously. This method proved satisfactory for data records in modes 1, 2, 4, and 5, but the 3rd mode proved to be very difficult

to excite. Table IV shows the array of speed, modes and interblade phase angle for which records were made. Vibratory testing was not carried out at speeds above 7,000 RPM because the earlier calculations had indicated a potential 100 ksi steady stress at the airfoil trailing edge. The combination of this high steady stress with vibratory stress suggested the risk of failure to be unacceptably high.

VIII. DISCUSSION

A. Steady State Deflections

The influence of the centrifugal field on the steady state blade twist for the SR-5 is summarized in Figures 17, and 18. Figure 17 shows the spanwise distribution of airfoil twist about the Y (radial) axis obtained from measurements at the midchord row of mirrors at three spanwise locations (A2, B2, C2). It is seen that the twist angle increases unformly with span up to about 80% from which point it decreases out to the tip. The interruption in the 8,000 RPM curve is caused by the fact that the spots reflected from the B row of mirrors were outside the range of the viewing window and consequently could not be photographed. Also shown in Figure 17 are the results of NASTRAN calculations at 7,000 RPM. NASTRAN results are in agreement to within 5% of the mirror data up to this spanwise position of maximum twist angle beyond which NASTRAN does not predict the decrease in twist clearly indicated by these data.

Figure 18 compares the difference in twist angle from leading to trailing edge along the span at 7,000 RPM. NASTRAN results at similar blade locations are also shown on the figure. It is seen that over most of the span the trailing edge twists much more than the leading edge resulting in the significant decrease in airfoil camber shown. Near the root and tip the sense of the camber change is reversed leading to a small camber increase particularly at the tip. NASTRAN results show a similar uncambering characteristic with span which agrees closely with the measured values up to about 60% span above which NASTRAN indicates larger uncamber than was measured. For the transonic Mach numbers at which the blade operates, it may be anticipated that (a) similar changes in airfoil camber will have a significant effect on overall rotor performance and (b) a precise knowledge of the blade twist and uncamber will be required to predict the aerodynamics.

Plots of all the individual mirror data θ_Y and θ_Z, corrected to NASTRAN axis system are given in Appendix I.

An attempt was made to obtain the blade deflection u (axial) by integrating the measured θ_Y and θ_Z slopes over the surface of the blade. An expression for differential u deflection was written in terms of the θ_Y and θ_Z slopes. The θ_X term is assumed zero because the plane of the mirrors on the blades are perpendicular to the X axis consequently insensitive to rotations about this axis. It was further assumed that u is independent of path. To facilitate integration, the data was fitted using a least squares fit with a two-dimensional polynomial expression in Y and Z.

Integration of these expressions along several straight line paths gave rise to deflection values that were strongly path dependent and were much larger in magnitude than would normally be acceptable. It was concluded that this method of calculation of displacements is not satisfactory. Among the alternate methods examined, the following was chosen.

It was decided to take strobe photos of the tip and measure tip displacement more directly. Figure 19 (a superposition of two photographs of the tip of blade number 5 taken at 1,600 and 9,000 RPM) shows clearly the large centrifugal twists and displacement that can occur. In the figure, the lower image of the tip (painted white to enhance visibility) was taken at 1,600 RPM and the upper image taken at 9,000 RPM.

A careful review of the data indicated that a single photographic image of the tip does not contain adequate information for twist angle to be compared directly with corresponding laser/mirror twist data. The tip chord has projections on the X, Y and Z axes, consequently, centrifugal deformation of the blade results in projection of rotation on all the axes. The camera records only one of these projections which is related to Θ_Y, and therefore will not admit to quantitative comparison because the other components of rotation which couple with Θ_Y cannot be recorded on a single photographic plane. A more complete description of this effect is given in Appendix II.

Linear displacement measurements, however, are comparable because the displacement is in the same plane as the photographic image, and the u (axial) displacement characteristics for the leading and trailing edge tip section are shown in Figure 20 as a function of speed. The points plotted represent an average of two photographs from each of four blades with the spread of data indicated by the vertical bars. The four blades used for averaging the data were Serial Numbers 1, 2, 5 and 8. Blade number 10 was not included in the averaging because it had a different mass distribution from the other blades caused by the full array of 11 mirrors bonded to its surface. Results from NASTRAN obtained for 7,000 RPM show excellent agreement with the averaged measured values. Correlation of w (tangential) deflections by means of the tip photos has met with little success. It may be recalled that the correction of small differences in timing the strobe flash was done by means of a reference mark at the hub. An error in applying the timing correction measured at the hub to a physical blade deflected position at the tip is magnified by the ratio of tip radius to hub radius (a factor of approximately 3). This correction is of the same order as the blade w deflection, consequently the scatter in the photographic w measurements is the same size as the w displacements.

B. Vibratory Tests

A summary of the individual blade frequencies measured from the bench impact tests including the effects of instrumentation is given in Table V. The mode shape data, amplitude, and phase, for blade number 2 which had the extensive array of strain gages, is shown in Figures 22 through 26. Also shown on figures 22 through 25 are some deflection mode shape holograms supplied by NASA from their bench tests. As discussed in Section VII, the piezoelectric crystal excitation system was used to excite the five blades of the SR-5 rotor system both individually and in a variety of nodal diameter patterns for the first five blade modes. However, crosstalk between crystal excitation voltage and strain gage signals prevented acquisition of steady state frequency response data. Therefore, vibratory decay data was recorded and analyzed through time domain procedures. This approach has proven to be capable of providing required dynamic information for the assembly.

The specific rotor characteristics which were evaluated include:

1. Frequency vs. speed for the first five blade modes

2. Extent and characteristics of mechanical coupling among the blades and the resulting coupled modes

3. Blade stress mode shape response with speed for the first five blade modes.

Results obtained from reducing the vibratory tests are presented and discussed below.

Frequency Response of the Rotor - The variation of the vibratory natural frequencies of the assembly with speed is shown in Figure 21. Although excitation was imposed on all the blades at a variety of prescribed nodal diameter patterns in both forward and backward traveling waves, amplitude decay signatures generally consist of a mixture of waves.

At several speeds and modes, pairs of frequencies very close together were observed as shown in Figure 21. In these data, the upper frequency represents a mode in which all the blades are exactly in phase in an "umbrella" mode, and the lower frequency exhibits a mixed nodal diameter pattern. While strong response was noted in modes one, two, four, and five, the third mode proved to be difficult to excite at speeds above 4,000 RPM. Therefore, little data could be obtained close to the third mode frequency. This characteristic was also observed in the bench tests, in which the third mode response was always significantly less than the response in the other four modes. Examination of the mode shapes in the fourth and fifth modes shows that there is an apparent crossover of modal frequencies. This will be discussed further in Section C.

Figure 21 shows results from NASTRAN, a blade alone frequency calculation, for the frequency of the first five modes as a function of speed. Superposed on the same figure are the test data which represent the frequencies of system modes measured at selected speeds. It is emphasized that the test data shown in Figure 21 represent system modes and therefore are not directly comparable with the blade alone calculations shown. The frequency of the system modes shown are approximately 10% higher than the individual blade above frequencies for the first two modes. This is possibly due to the predominance of inertial effects in the coupling mechanism.

All of the experimental modes shown on Figure 21 represent rotor coupled modes; i.e., the response frequency of each blade in the rotor is the same, and there is a fixed interblade phase angle between them. The frequency spread among blades due to normal manufacturing tolerances is shown along the zero speed axis as measured from bench tests. Whether one blade of the assembly or the complete assembly was subjected to forced vibration, the entire assembly responded indicating a significant level of mechanical coupling among the blades. Attempts to relate the nodal diameter patterns of the response with the nodal pattern of the excitation show that they are not simply related because the response modes contain contributions from many harmonics. It is noteworthy, however, that the various combinations of nodal diameters show small differences in frequency or mode shape.

The excitation of the assembly included both single blade as well as all blades at 0, 1, and 2 nodal diameters in forward and backward traveling waves. Decay patterns were characterized by either strong umbrella mode response and/or a mixture of the other patterns. Tables VI through IX compare the relative response amplitude of the waves for different patterns of excitation including the excitation where only a single blade was driven. As observed earlier, examination of these tables shows no consistent relationship between the pattern of excitation and correspondent patterns of response. A possible explanation for this lack of traveling wave correlation, is that the transient force induced by switching off the excitation induces a mixture of traveling waves. The specific mixture is related to the timing of the transient during the cycle. The detailed characteristics shown for the first mode are typical of the higher modes also. It is interesting to note, however, that when the umbrella mode is the major constituent of the rotor response, the decay frequency is approximately 9% higher than those cases where the response contains other nodal diameter patterns.

These results are based on time domain analysis of the signals from three strain gages located on each of the five blades of the rotor, all of which are responding at a constant frequency. In order to verify the strength of the coupling, it is instructive to examine the frequency content in the response

by performing time domain analyses of individual decays from the three strain gages located on each of the blades. Table X compares system mode frequencies as calculated by comparing the three strain gages at corresponding locations on each of the five blades, with the frequency calculated for each of the blades independently using the output of the same three strain gages. The results shown on Table X are for 1st, 2nd, 4th, and 5th system modes at 7,000 RPM and are typical. Table X also shows underneath the frequency of the blade for that mode as measured on the bench. It can be seen that the coupled mode frequency spread among the blades is much less than would be seen if the blades were not coupled through the hub.

C. Blade Strain Mode Shape

The variation in blade strain distribution for each mode and speed was also evaluated. In order to clarify the individual blade strain mode shapes, the information from the twelve active strain gages on blade number 2 is displayed as shown on Figure 22. In this figure, an outline of the pressure and suction surface of the blade is shown along with the location and orientation of each of the strain gages. Strain gage numbers 1 and 5 were not included in the data recording because their output during the bench test characterization was less than 5% of the maximum reading strain gage for all five modes of vibration, so it was felt that they would contribute little to mode identification. Below the blade outline is a bar chart where each bar represents the output from the corresponding numbered gage on the blade. The height of the bar represents strain amplitude normalized to the maximum (which varies for different modes) and the position above or below the axis shows whether the phase angle relative to gage number 2 is 0 or 180 degrees.

Figures 22 through 26 are the results of the modal analysis evaluation of the zero RPM bench impact tests. For the first four bench vibration modes, NASA acquired physical displacement mode shape data by means of holograms which are included as insets on Figures 22 through 25. This data allows qualitative comparison of physical deflection with local strain.

Results from time domain analyses of blade strain mode shape at speeds of 4,000, 5,000, 6,000 and 7,000 RPM, are shown on Figures 27 through 31, where rotational symbols have been superimposed on the bench test results to facilitate comparison.

Two groups of four symbols have been superimposed on each "bar" to show blade mode response for the two characteristic system modes with zero inter-blade phase angle (umbrella mode) having solid symbols, and the nonzero inter-blade phase (mixed nodal diameters) angle having open symbols. The speed at which the data were recorded is shown by the shape of the symbols. The displays are complete for the first and second modes, but only partial for the higher modes because there were fewer of these data with sufficiently high confidence factors. The third mode is particularly sparse, because of the difficulty in exciting it at speeds over 4,000 RPM.

Examination of the change of the mode shapes with respect to speed leads to the following observations.

a) The system mode with predominantly zero interblade phase angle (umbrella mode) and modes with nonzero interblade phase angle (mixed nodal diameters) show virtually no difference in blade strain mode shape despite the frequency difference on the order of 9%.

b) The modal distribution of strain from the zero RPM measurements is only an initial screen for modal identification because the data at speed may show a substantial difference and may reflect changes in blade root constraint.

c) The highest frequency mode at speeds above 4,000 RPM has a strain distribution resembling that of the fourth mode at zero RPM (fig. 30).

d) The fourth mode at speeds above 4,000 RPM has a strain distribution resembling that of 5th mode at zero RPM (fig. 31).

e) The third mode was difficult to excite at speeds above 4,000 RPM, consequently changes in strain distribution with speed could not be recorded.

The vibratory stresses at the strain gage positions calculated from NASTRAN, are also used for comparison with the corresponding experimental blade measurements. With the computed values of σ_x, σ_y, τ_{xy} for each finite element, the stress component oriented in the strain gage direction can be calculated, i.e.,

$$\sigma_\theta = \frac{\sigma_x+\sigma_y}{2} + \frac{\sigma_x-\sigma_y}{2} \cos 2\theta + \tau_{xy} \sin 2\theta$$

These values were averaged arithmetically for the elements immediately adjacent to the nodal point identified with a particular strain gage. These results are shown superimposed on the bench test results in Figures 32 through 36.

The first two modes showed satisfactory correspondence between experimental bench test mode shapes and the NASTRAN predictions at both zero and 7,000 RPM. The third NASTRAN mode, in contrast, showed no relationship to any of the three higher bench modes. The fourth bench test mode showed significant similarity to the fifth mode of the NASTRAN predictions. The fifth bench test mode and the fourth NASTRAN modes showed a limited similarity to each other.

The NASTRAN model used a mesh size which gave undesirably large variations in σ_θ among the elements surrounding a nodal point, in the higher modes. For modes above the lowest two, a locally refined grid might be used to advantage.

IX. MAJOR CONCLUSIONS AND RECOMMENDATIONS

Based on (a) the test data obtained by testing the five blade configuration of the SR-5 assembly, and (b) the NASTRAN analytical results that were made available by NASA/LeRC, the following major conclusions can be drawn.

1. Centrifugal loads acting on the assembly cause large reductions in airfoil camber over most of the blade surface.

2. Maximum twist due to centrifugal loads occurs inboard of the tip at approximately 80% span.

3. For the first five modes of vibration, the rotor responds as a system with all blades vibrating at the same frequency.

4. Blade strain mode shapes exhibit small changes between 4,000 and 7,000 RPM for the first five modes of vibration.

5. NASTRAN blade alone frequencies generally agree to within 10% of the measured system mode frequencies.

6. NASTRAN calculation of blade tip axial deflection in the centrifugal field agrees with the measured values.

7. Significant differences exist between results calculated from NASTRAN and corresponding measurements for twist and uncamber distribution.

8. Significant differences exist between results calculated from NASTRAN and corresponding measurements of vibratory stress distributions at both zero and 7,000 RPM. The biggest discrepancy occurs for the 3rd, 4th, and 5th modes of vibration.

9. Mechanical coupling among the blades can arise due to either the inertia of the hub and/or the elasticity of the hub and pitch change mechanism. The relative strengths of these contributions need to be assessed.

10. The major conclusions in regard to the modal characteristics of the SR-5 assembly were drawn from analysis of vibration decay data. Further confirmation of these conclusions may be needed through data obtained from measurements of frequency response characteristics.

11. The added mass of the blade mounted mirrors is apparent in the centrifugal deflection measurements.

X. REFERENCES

1. Dugan, J. F., Miller, B. A., Grabear, J. J., Sagerser, D. A.: The NASA High Speed Turboprop Program. National Aeronautics and Space Administration, NASA TM 81561, October 1980.

2. Mehmed, O., Kaza, K. R. V., Lubomski, J. F., Kielb, R. E.: Bending Torsion Flutter of a Highly Swept Advanced Turboprop. NASA TM 82975, October 1982.

3. Lawrence, C., Kielb, R.: Finite Element Analysis of an Advanced Turbo-Prop Blade. NASA TM (To be published).

4. Hartman, E. P., D. Biermann: Torsional and Bending Deflection of Full Scale Aluminum Alloy Propeller Blades Under Normal Operating Conditions, NACA Report 644, Langley Memorial Aeronautical Laboratory, January 1938.

5. Stargardter, H.: Optical Determination of Rotating Fan Blade Deflections. Journal of Engineering for Power, April 1977, pp. 204-209.

6. Stargardter, H.: U. S. Patent 4,080,823: Vibration Measurement.

7. Srinivasan, A. V., Cutts, D. G.: Basic Study of Bladed Disk Structural Response. United Technologies Research Center, AFWAL TR-83-2075, November 1983.

8. Ibraham, S. R., Mikulcik, E. C.: A Method for the Direct Identification of Vibration Parameters from the Free Response, Shock and Vibration Bulletin, Vol. 47, Part 4, pp. 183-198, September 1977.

9. Brand, L.: Vector and Tensor Analysis. Wiley, New York 1947.

TABLE I

Number of Blades in Rotor: 5	(10 in prototype)
R_{Tip}	12.1 in (31 cm)
R_{Hub}	2.83 in (7.19 cm)
t/b_{Root}	.105
t/b_{Tip}	.018
Mechanical Design RPM	9000
Tip Speed at Design	950 ft/sec (290 m/sec)
Material	Ti 6-4
Reference angle at 3/4 radius 58.5 deg relative to tangential plane	
Max sweep back angle at tip	63 degrees
LE Radius Tip (nominal)	.003 in (.0076 cm)
LE Radius Root (nominal)	.0614 in (.156 cm)

Table II Moment Weight Results

BLADE NUMBER	BLADE WEIGHT gms	MOMENT WEIGHT gmcm
5	387.6	5009.6
1	388.9	5051.8
2	392.5	5062.6
8	396.0	5153.3
10	399.2	5245.7

INCLUDING INSTRUMENTATION

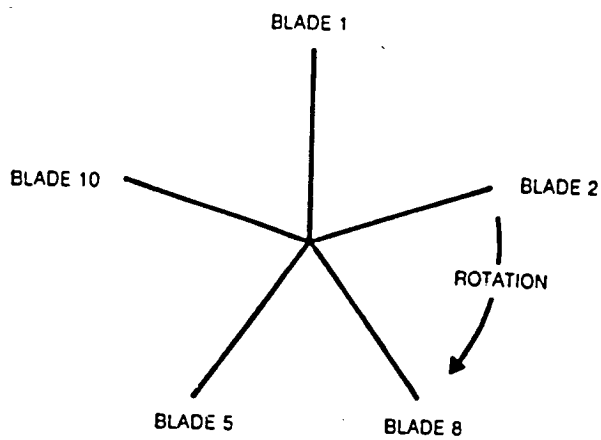

ORDER OF BLADES IN ROTOR

VIEW LOOKING DOWN STREAM

84-4-7-8

TABLE III

PROP-FAN STRAIN GAGE LOCATION

Gage No.	Surface	Gage Type	Grid No.	X	Y	Z	Orien. of Grid
8,9,10	Pressure	Rosette	317	0.2403	6.9958	-0.0128	0-90-45°
11	Pressure	Uniaxial	155	-1.0962	9.4786	0.5885	Parallel to LE
12	Pressure	Uniaxial	206 Between 67 & 78	0.5046	11.0547	-0.8096	Parallel to LE
13	Pressure	Uniaxial	202 Between 23-34	1.2244	11.6501	-1.5318	- LE
14	Pressure	Uniaxial	176	1.8833	9.2321	-1.1797	Parallel to TE
7	Suction	Uniaxial	105	1.1116	10.5534	-1.1412	40° to YZ Plane
4,5,6	Suction	Rosette	150	0.8160	9.7245	-0.7130	0-90-45°
1,2,3	Suction	Rosette	316	-0.1186	6.9958	0.1698	0-90-45°
15	In Fillet	Uniaxial	435	0.5397	3.1003	-0.1820	

TABLE IV

Speed	Mode	Blade Excited	Interblade Phase Angle
4000	1	#2	
		All	0
			+72
			+144
			-144
			-72
	2	All	0
	3	#2	
		All	0
			+72
			+144
			-144
			-72
	4	#2	
	5	#2	
		All	0
			+72
			+144
			-144
			-72
5000	1	#2	
		All	0
			+72
			+144
			-144
			-72
	2	#2	
		All	0
	3	#2	
		All	0
			+72
			+144
			-144
			-72
	4	#2	
	5	#2	
		All	0
			+72
			+144
			-144
			-72

Speed	Mode	Blade Excited	Interblade Phase Angle
6000	1	#2	
		All	0
			+72
			+144
			-144
			-72
	2	#2	
		All	0
			+72
			+144
			-144
			-72
	3	#2	
		All	0
			+72
			+144
			-144
			-72
	4	#2	
		All	0
	5	#2	
		All	0
			+72
			+144
			-144
			-72
7000	1	#2	
		All	0
			+72
			+144
			-144
			-72
	2	#2	
		All	0
			+72
			+144
			-144
			-72
	3	#2	
		All	0
			+72
			+144
			-144
			-72
	4	#2	
	5	#2	
		All	0
			+72
			+144
			-144
			-72

TABLE V

BENCH TEST RESULTS

Summary of Individual Blade Frequency
Including Instrumentation

MODE	BLADE SERIAL NUMBER				
	1	2*	8	5	10**
1	110 Hz	112 Hz	109 Hz	113 Hz	112 Hz
2	274 Hz	281 Hz	277 Hz	283 Hz	277 Hz
3	472 Hz	476 Hz	495 Hz	492 Hz	462 Hz
4	596 Hz	604 Hz	607 Hz	617 Hz	594 Hz
5	633 Hz	638 Hz	641 Hz	649 Hz	646 Hz

* 15 Strain Gages on Blade
** 11 Mirrors on Blade

TABLE VI

NODAL DIAMETER RESPONSE PATTERN DURING
DECAY VS. TYPE OF EXCITATION

4,000 RPM
First Mode
Strain Gage No. 12 on All Blades

EXCITATION PATTERN

Strength of Harmonic Present During Decay	Single Blade Excitation	0 Nodal Dia. (umbrella)	1 Nodal Dia. Forward	2 Nodal Dia. Forward	2 Nodal Dia. Backward	1 Nodal Dia. Backward
0 Nodal Dia. (umbrella)	1.00	1.00	.15	.15	.10	.10
1 Nodal Dia. Forward	.25	.25	.65	.65	.10	.65
2 Nodal Dia. Forward	.20	.20	.60	.75	1.00	.70
2 Nodal Dia. Backward	.20	.20	1.00	1.00	.45	1.00
1 Nodal Dia. Backward	.30	.30	.35	.75	.60	.40
System Frequency	148.23 Hz	148.39 Hz	135.01 Hz	135.10 Hz	134.56 Hz	134.86 Hz

TABLE VII

NODAL DIAMETER RESPONSE PATTERN DURING
DECAY VS. TYPE OF EXCITATION

5,000 RPM
First Mode
Strain Gage No. 12 on All Blades

EXCITATION PATTERN

Strength of Harmonic Present During Decay	Single Blade Excitation	0 Nodal Dia. (umbrella)	1 Nodal Dia. Forward	2 Nodal Dia. Forward	2 Nodal Dia. Backward	1 Nodal Dia. Backward
0 Nodal Dia. (umbrella)	.35	.35	.30	.35	.35	.40
1 Nodal Dia. Forward	.70	.75	.65	.75	.70	.60
2 Nodal Dia. Forward	.85	.30	.65	.85	.95	.95
2 Nodal Dia. Backward	1.00	.40	1.00	1.00	1.00	1.00
1 Nodal Dia. Backward	.85	1.00	.60	.95	.80	.60
System Frequency	145.82 Hz	145.97 Hz	145.72 Hz	145.76 Hz	144.81 Hz	145.73 Hz

TABLE VIII

NODAL DIAMETER RESPONSE PATTERN DURING
DECAY VS. TYPE OF EXCITATION

6,000 RPM
First Mode
Strain Gage No. 12 on All Blades

EXCITATION PATTERN

Strength of Harmonic Present During Decay	Single Blade Excitation	0 Nodal Dia. (umbrella)	1 Nodal Dia. Forward	2 Nodal Dia. Forward	2 Nodal Dia. Backward	1 Nodal Dia. Backward
0 Nodal Dia. (umbrella)	1.00	1.00	.40	.15	No Data	.15
1 Nodal Dia. Forward	0	0	.65	.30		.40
2 Nodal Dia. Forward	.10	.10	.25	.90		1.00
2 Nodal Dia. Backward	.05	.05	.30	1.00		.95
1 Nodal Dia. Backward	.05	.05	1.00	.45		.35
System Response Frequency	173.99 Hz	174.43 Hz	158.8 Hz	157.18 Hz		157.71 Hz

TABLE IX

NODAL DIAMETER RESPONSE PATTERN DURING
DECAY VS. TYPE OF EXCITATION

7,000 RPM
First Mode
Strain Gage No. 12 on All Blades

EXCITATION PATTERN

Strength of Harmonic Present During Decay	Single Blade Excitation	0 Nodal Dia. (umbrella)	1 Nodal Dia. Forward	2 Nodal Dia. Forward	2 Nodal Dia. Backward	1 Nodal Dia. Backward
0 Nodal Dia. (umbrella)	0	1.00	.05	.15	.10	0
1 Nodal Dia. Forward	1.00	0	1.00	.25	.10	.60
2 Nodal Dia. Forward	.20	.05	.15	.85	1.00	.40
2 Nodal Dia. Backward	.20	.05	.20	1.00	.45	.10
1 Nodal Dia. Backward	.45	.05	.45	.35	.30	1.00
System Freq. of Delay	172.33 Hz	188.31 Hz	173.39 Hz	170.70 Hz	170.42 Hz	172.03 Hz

TABLE X

COMPARISON OF SYSTEM FREQUENCY WITH BLADE FREQUENCY
AT THE SAME TEST POINT

	System Mode Frequency	Blade 1 Freq.	Blade 2 Freq. All Gages/2 Gages	Blade 8 Freq.	Blade 5 Freq.	Blade 10 Freq.
First Mode 7,000 RPM Excite Single Blade	172.4 Hz	172.3 Hz	172.5/172.5 Hz	172.1 Hz	172.4 Hz	172.3 Hz
First Mode 0 RPM Bench Test		110 Hz	112 Hz	109 Hz	113 Hz	112 Hz
Second Mode 7,000 RPM Excite Single Blade	291.8 Hz	292.1 Hz	292 Hz	291.5 Hz	305 Hz*	291.7 Hz
Second Mode 0 RPM Bench Test		274 Hz	281 Hz	277 Hz	283 Hz	277 Hz
Fourth Mode 7,000 RPM Excite All Blades $\varphi = 144°$	620.5 Hz	620.4 Hz	621.0/620.8 Hz	621.2 Hz	623.3 Hz	619.9 Hz
Fourth Mode 0 RPM Bench Test		596 Hz	604 Hz	607 Hz	617 Hz	594 Hz
Fifth Mode 7,000 RPM Excite All Blades $\varphi=72°$	711.2 Hz	711.7 Hz	710.7/712.0 Hz	712.9 Hz	704 Hz*	712.7 Hz
Fifth Mode 0 RPM Bench Test		633 Hz	638 Hz	641 Hz	649 Hz	646 Hz

* Analysis showed low confidence factor

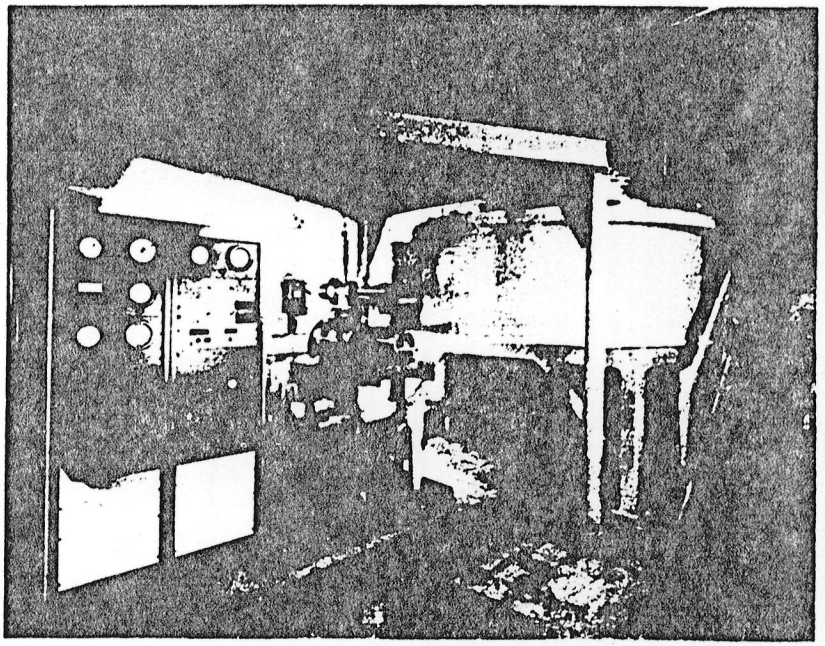

Fig. 1 UTRC Centrifugal Testing Facility

82-12-73-27

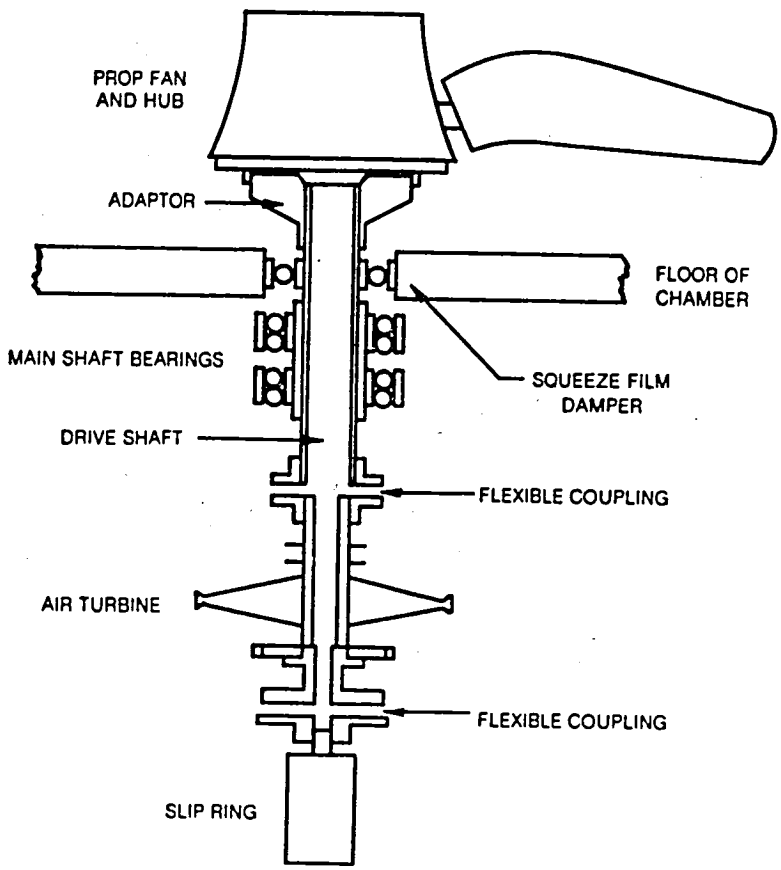

Fig. 2 UTRC Spin Rig Drive System

84-4-7-9

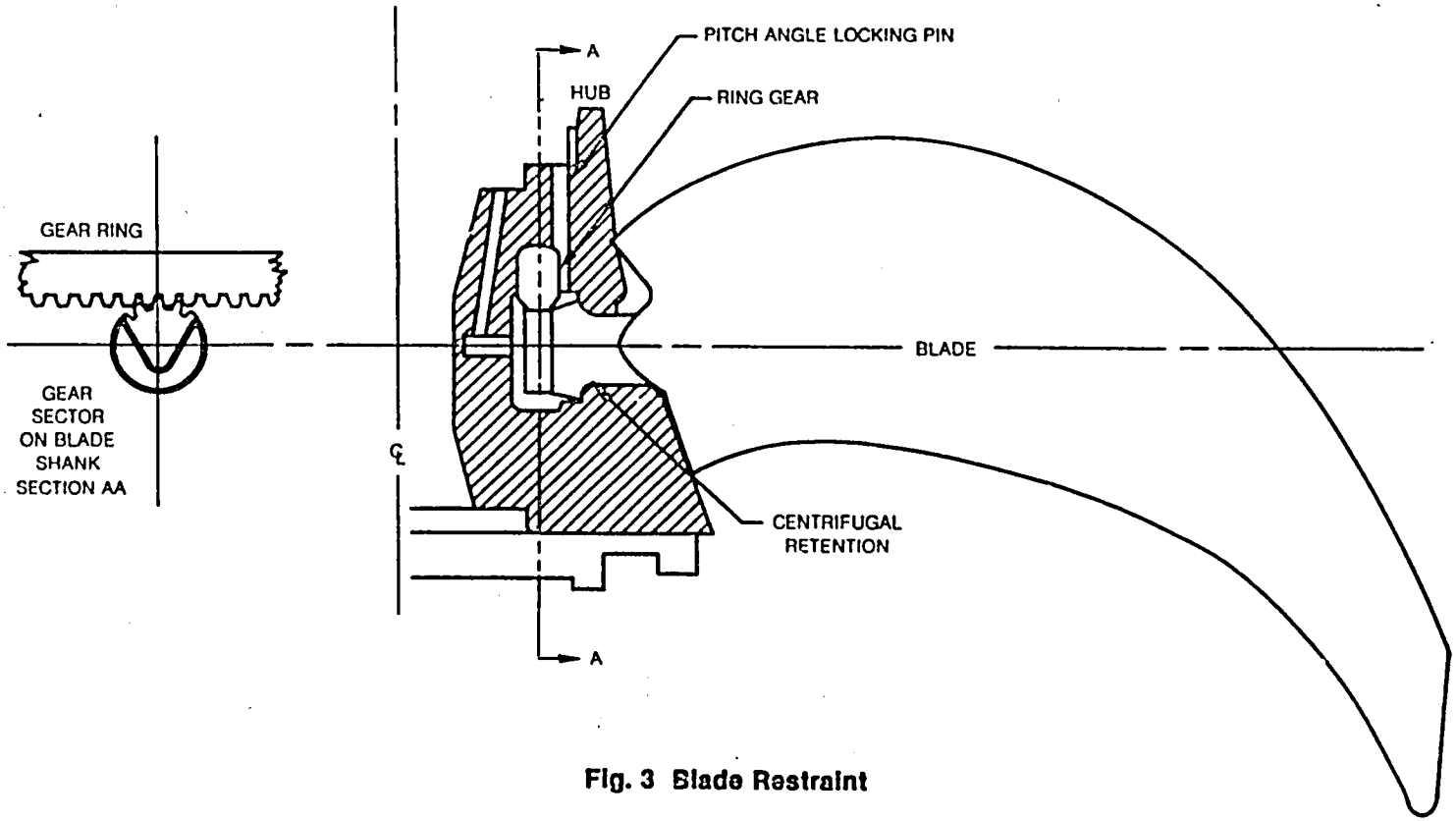

Fig. 3 Blade Restraint

Fig. 4 Photograph of Instrumented SR5 Assembly in UTRC Spin Rig

84-4-7-2

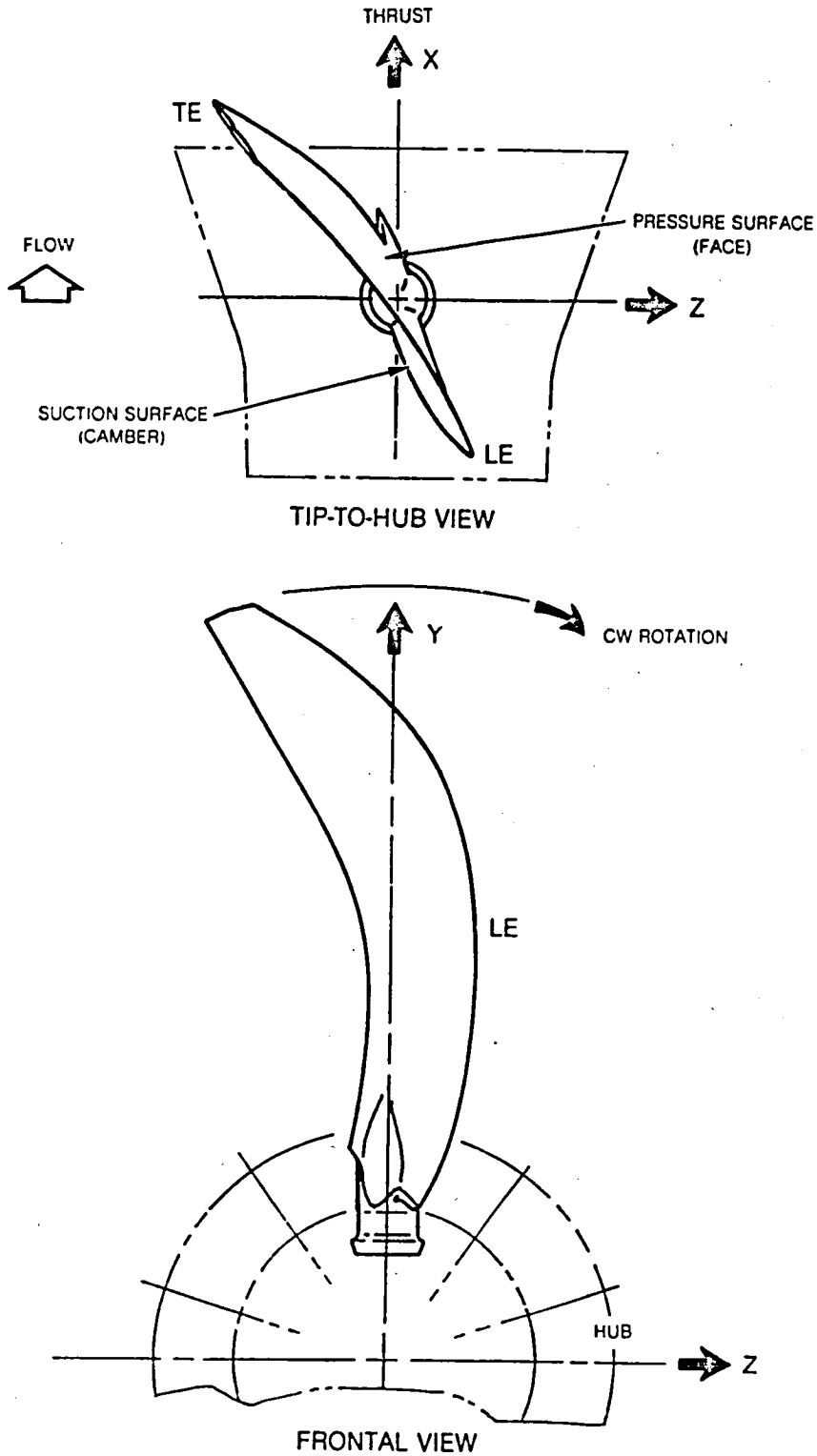

Fig. 5 Blade Coordinate System

84-4-7-38

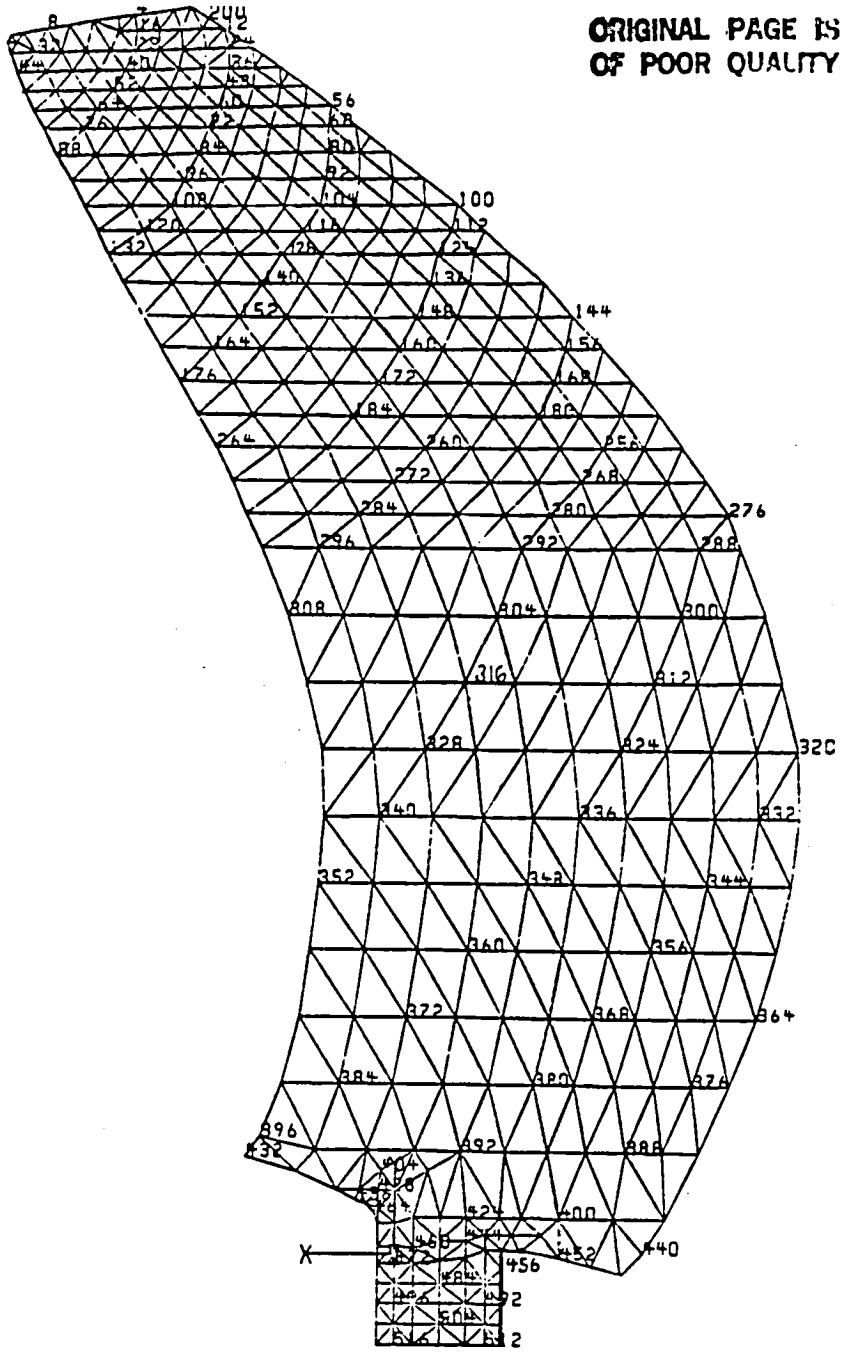

Fig. 6 NASTRAN Grid Breakup of SR5 Blade

84-4-7-39

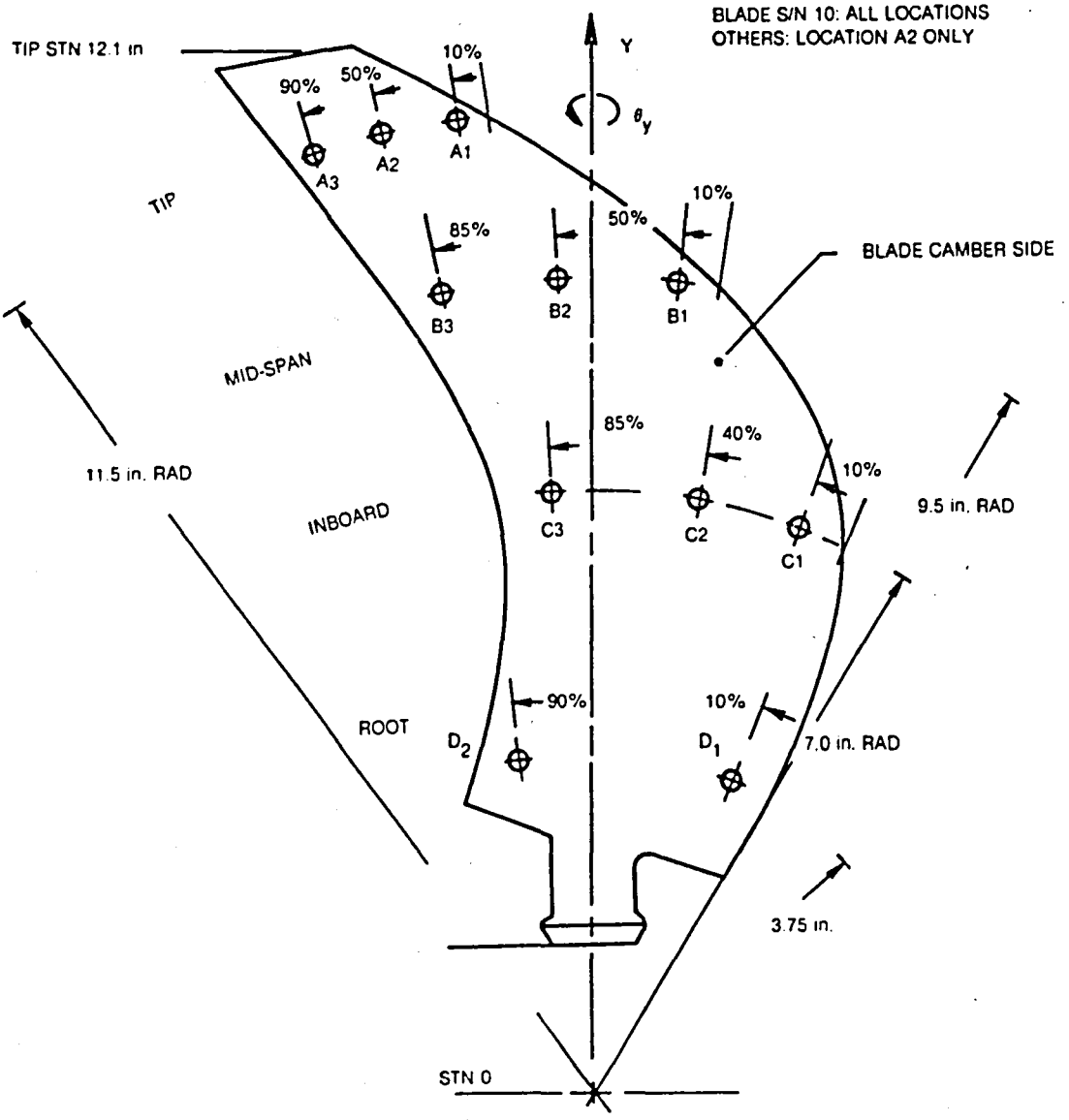

Fig. 7 SR-5 Model Prop-Fan Blade Mirror Locations

84-A-7-12

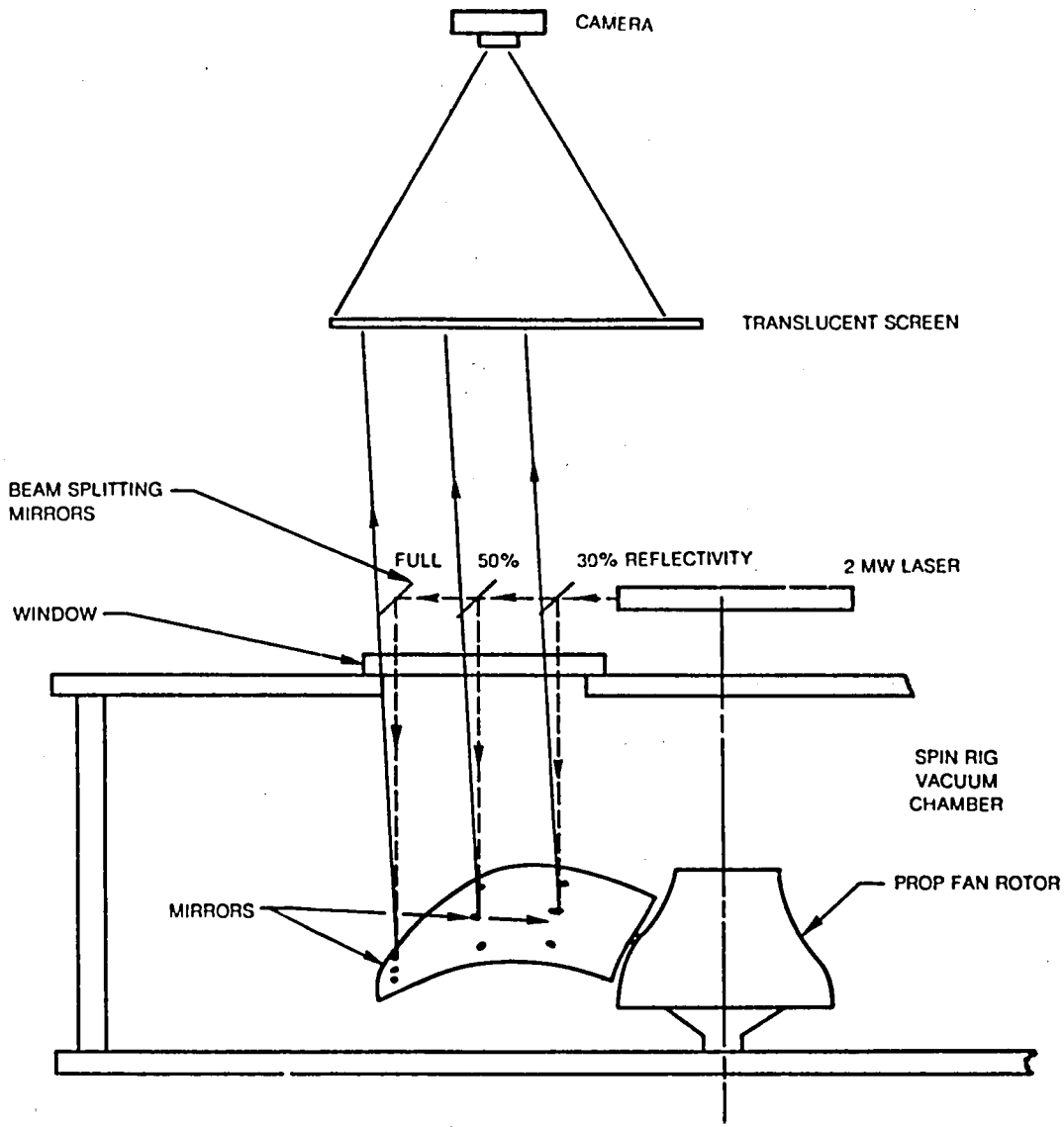

Fig. 8 Schematic of Laser Mirror Set-Up for Blade Deflection Measurement

ORIGINAL PAGE IS
OF POOR QUALITY

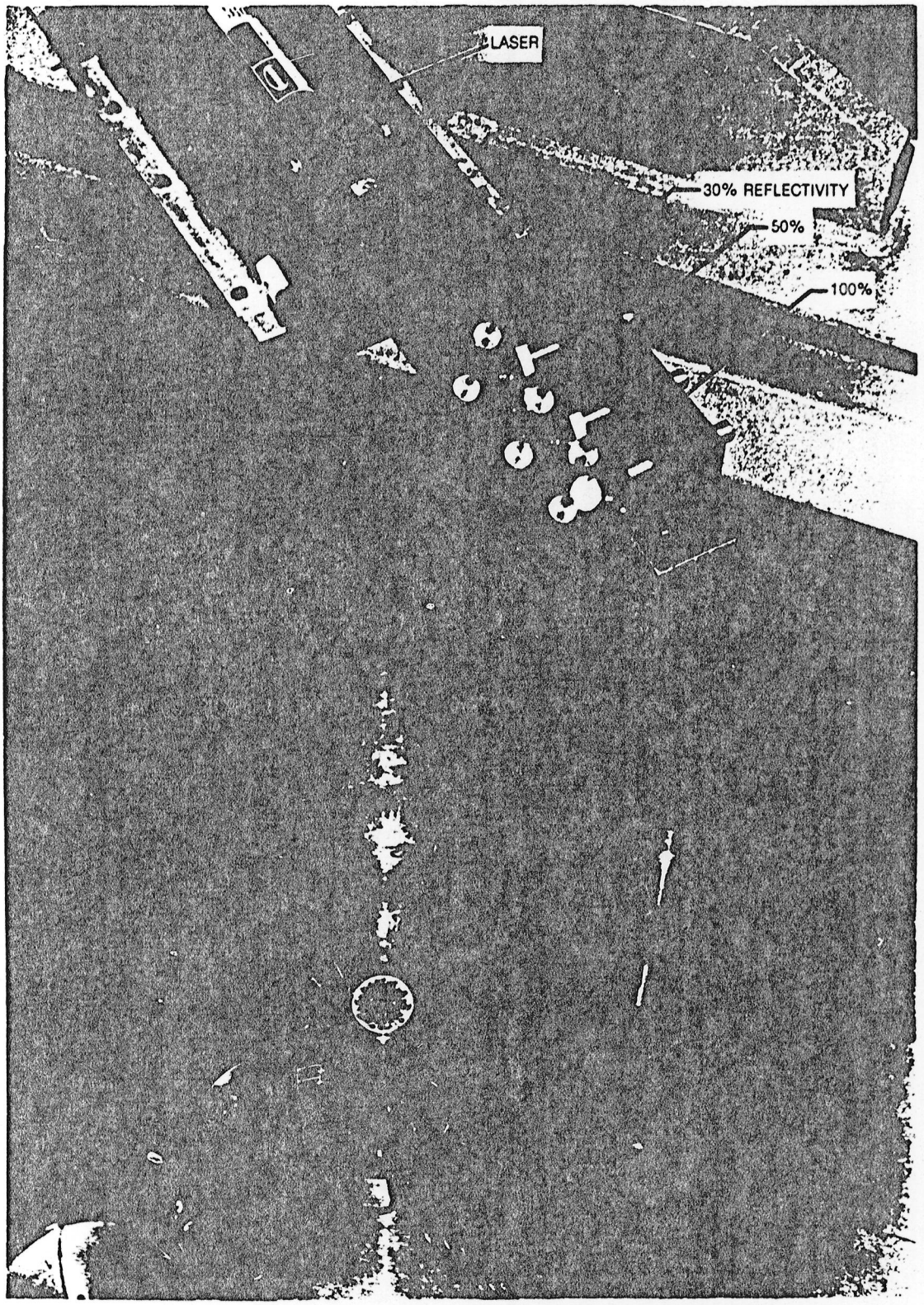

Fig. 9 A Close-Up Photograph of Optical Bench

84-4-7-5

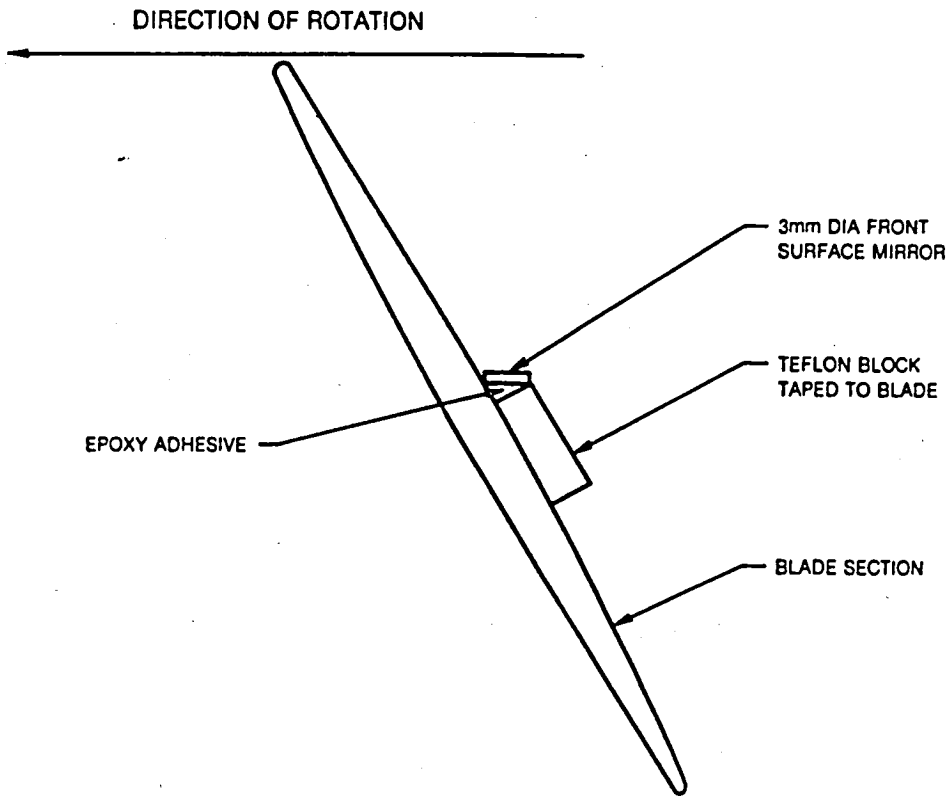

Fig. 10 Scheme for Bonding Mirrors to Blade

84-4-7-32

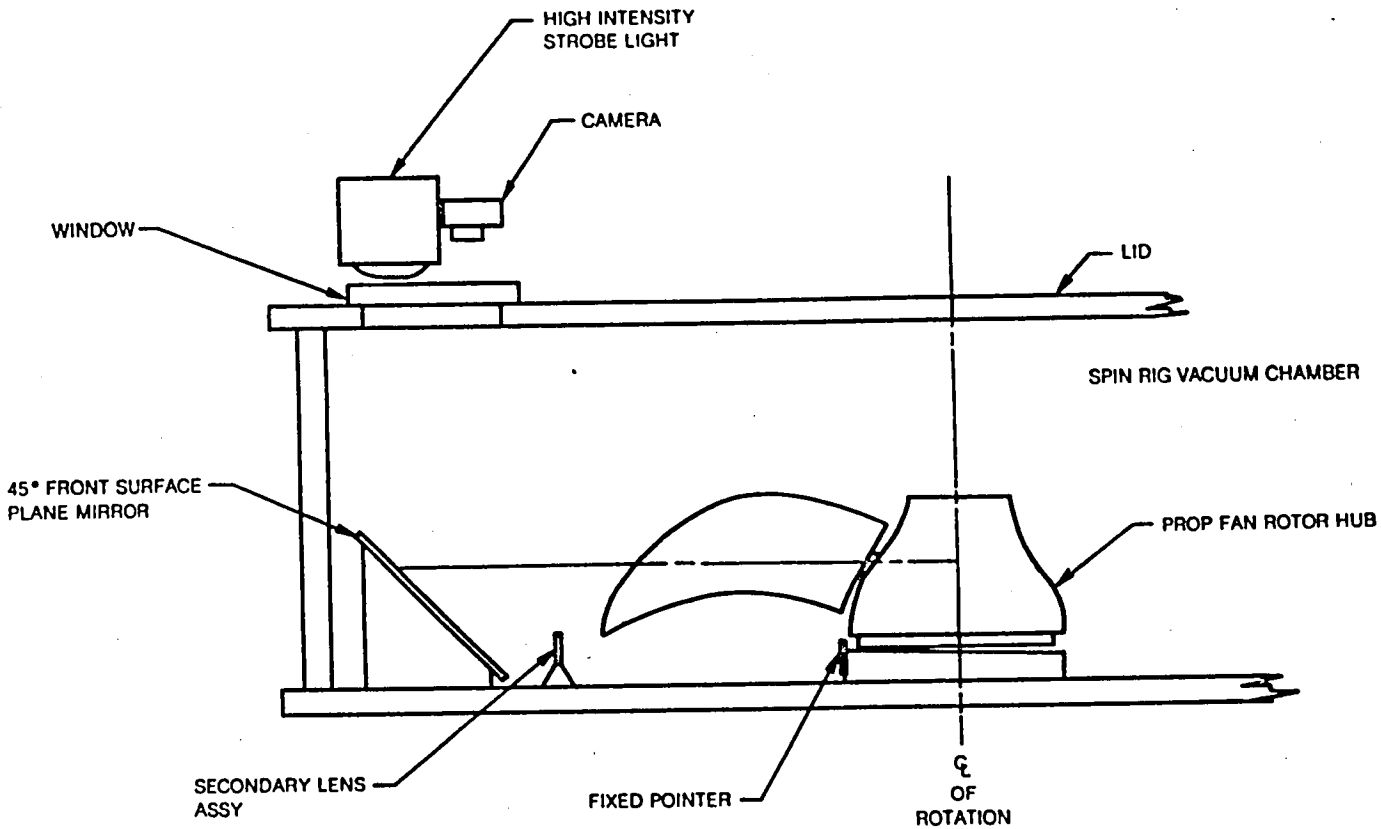

Fig. 11 Schematic of Tip Photograph Set Up

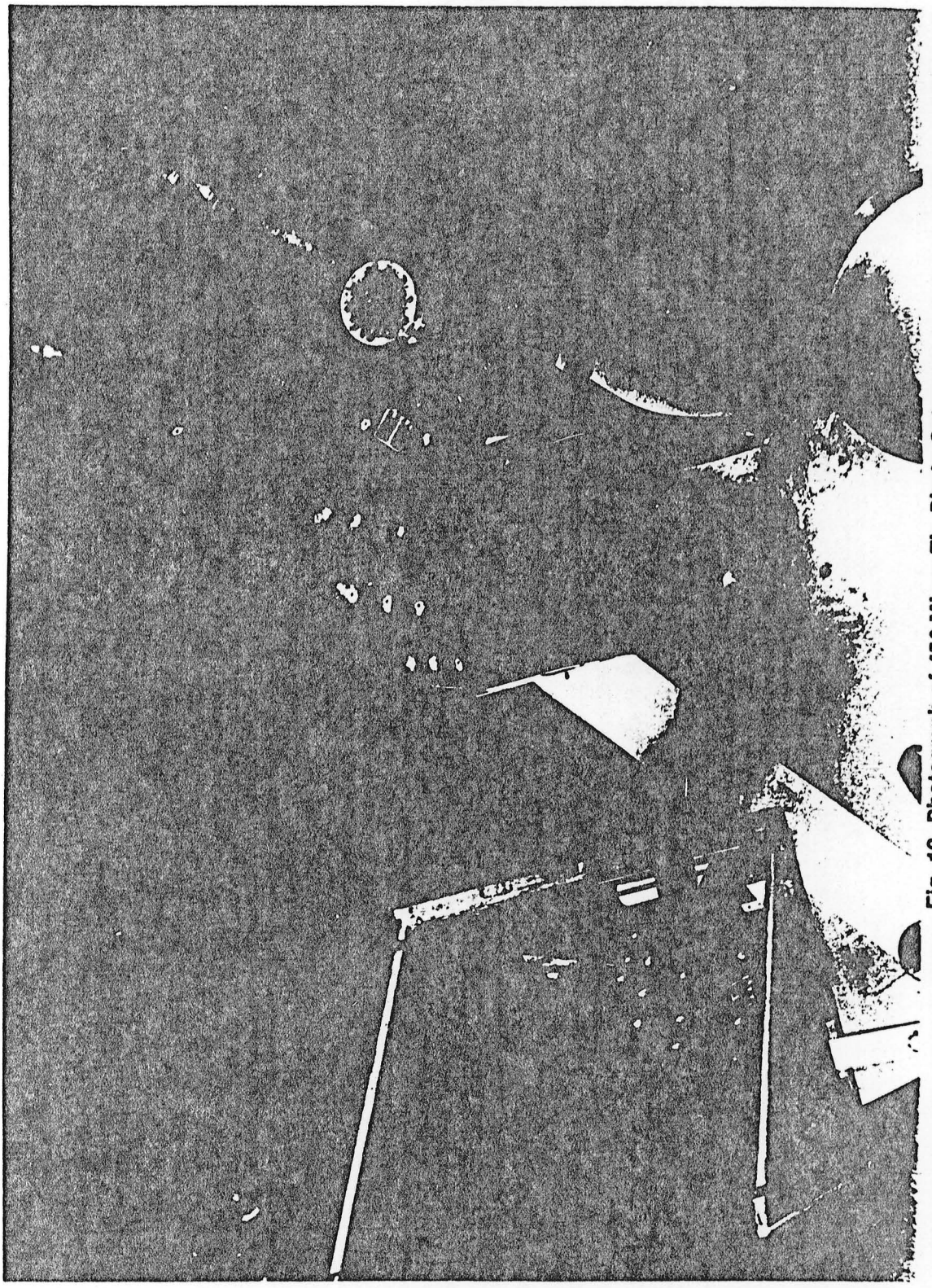

Fig. 12 Photograph of 45° Mirror-Tip Photo Setup

84-4-7-3

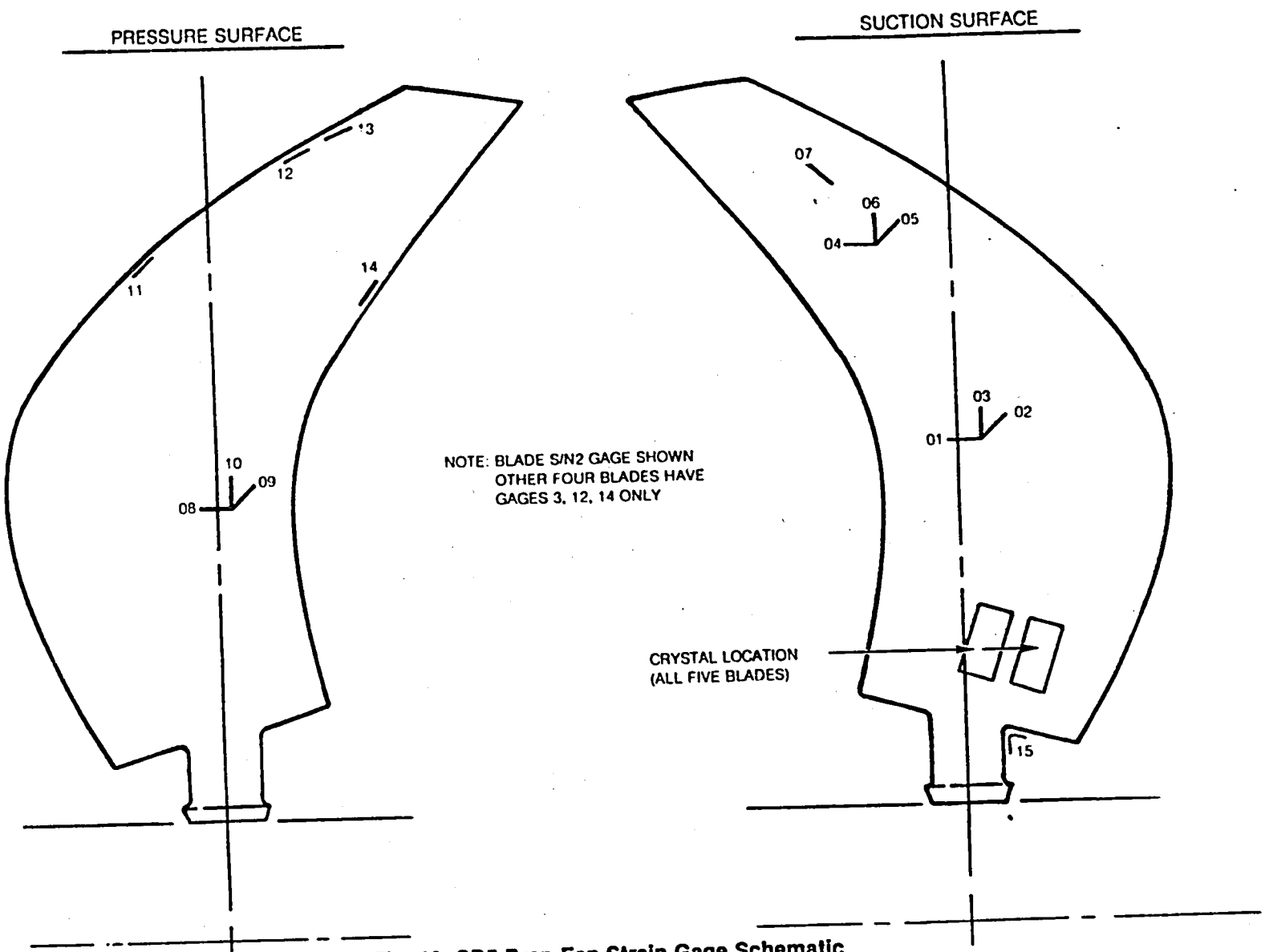

Fig. 13 SR5 Prop Fan Strain Gage Schematic

84-4-7-20

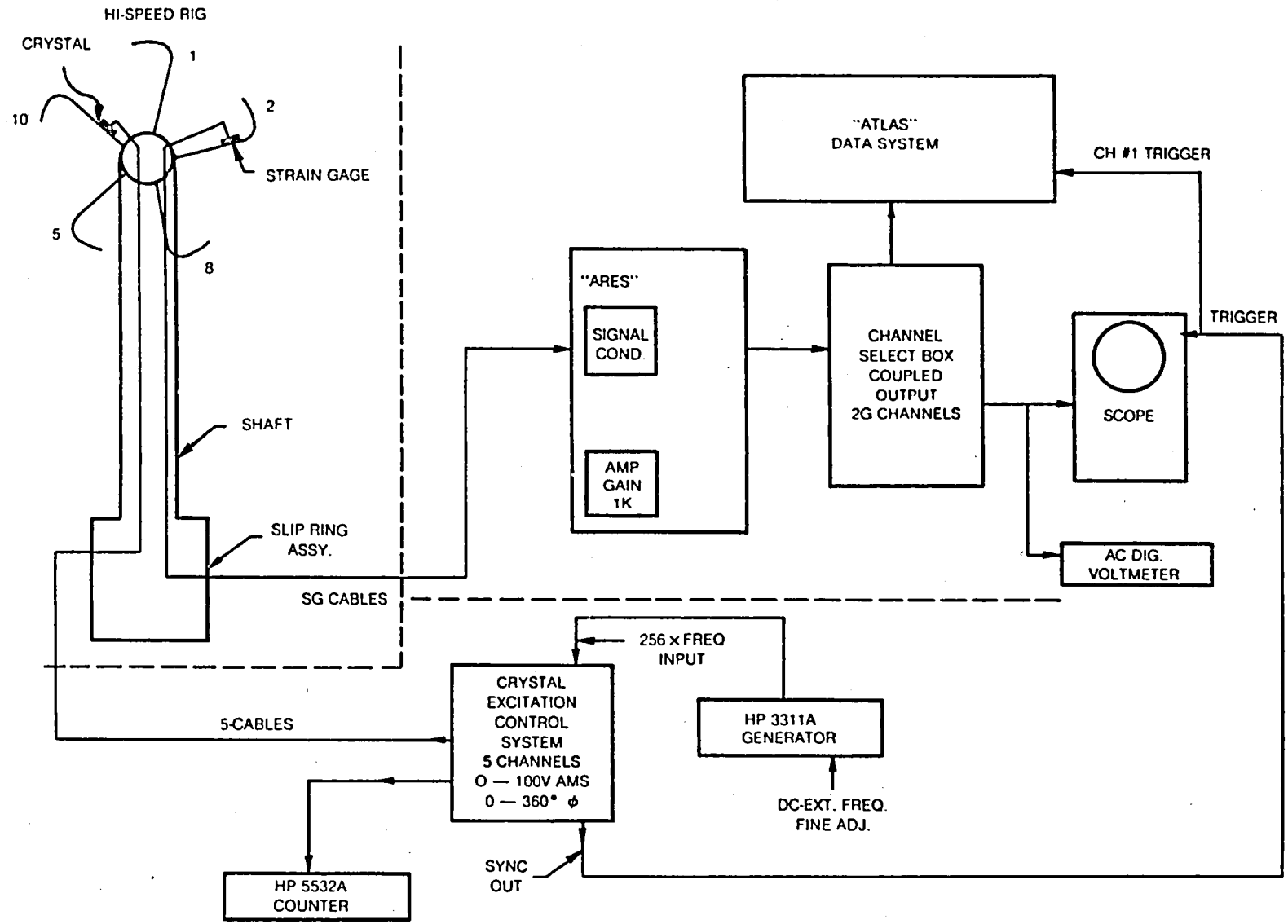

Fig. 14 Diagram of Excitation System, Data Acquisition and Recording System

84-4-7-1

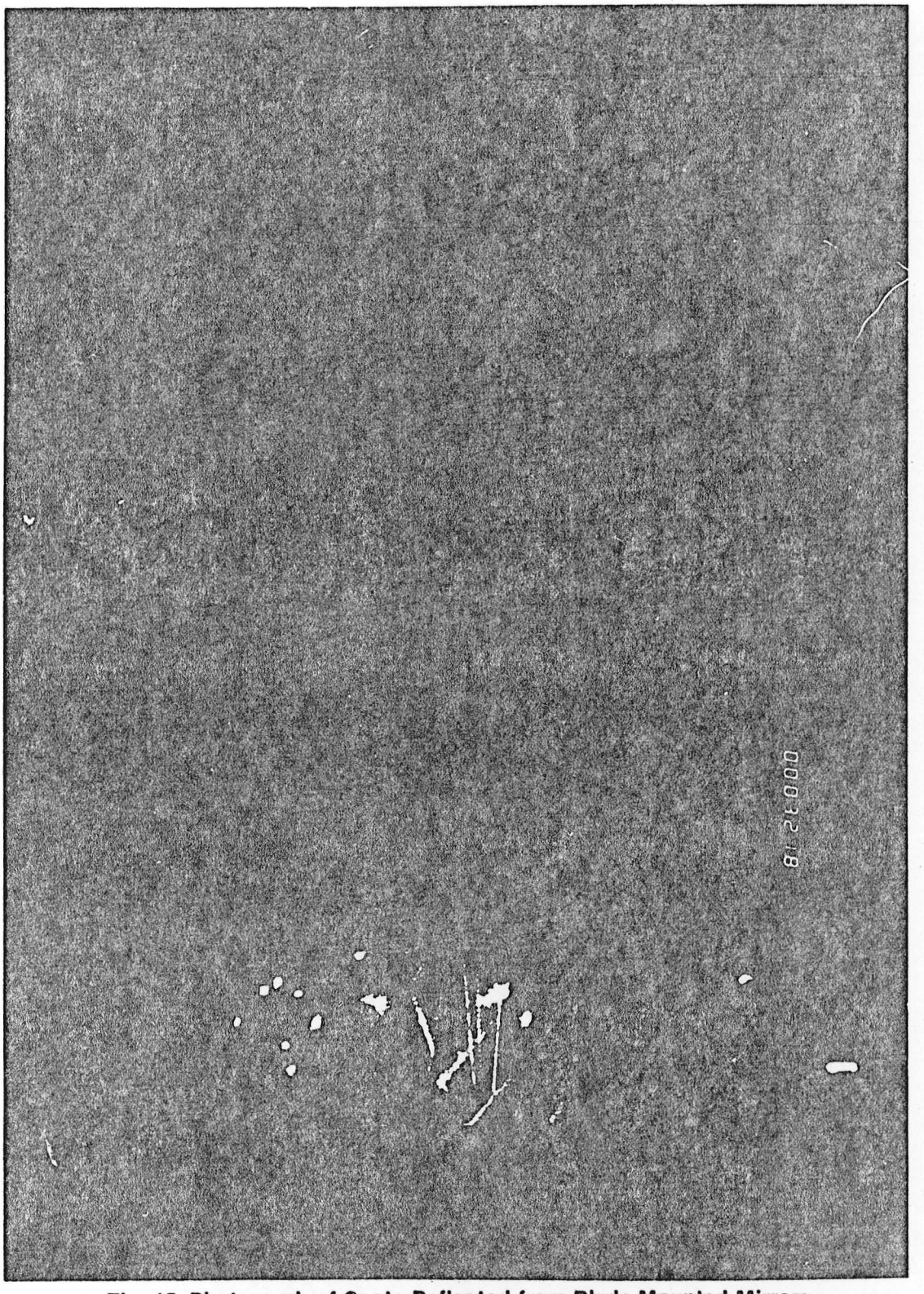

Fig. 15 Photograph of Spots Reflected from Blade Mounted Mirrors

84-4-7-4

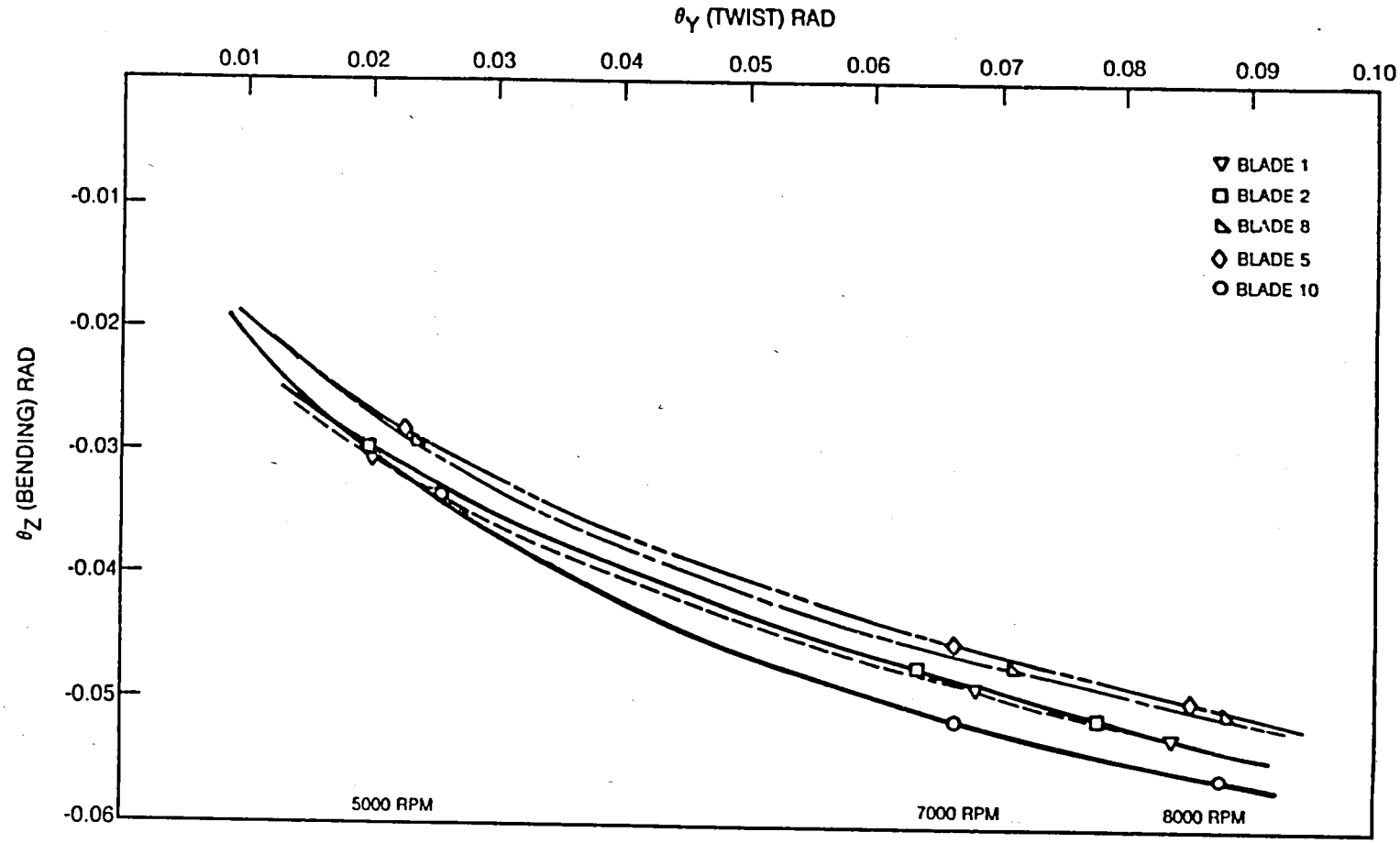

Fig. 16 SR5 Steady State Bending (θ_Z) and Twist (θ_Y) at Midchord Tip

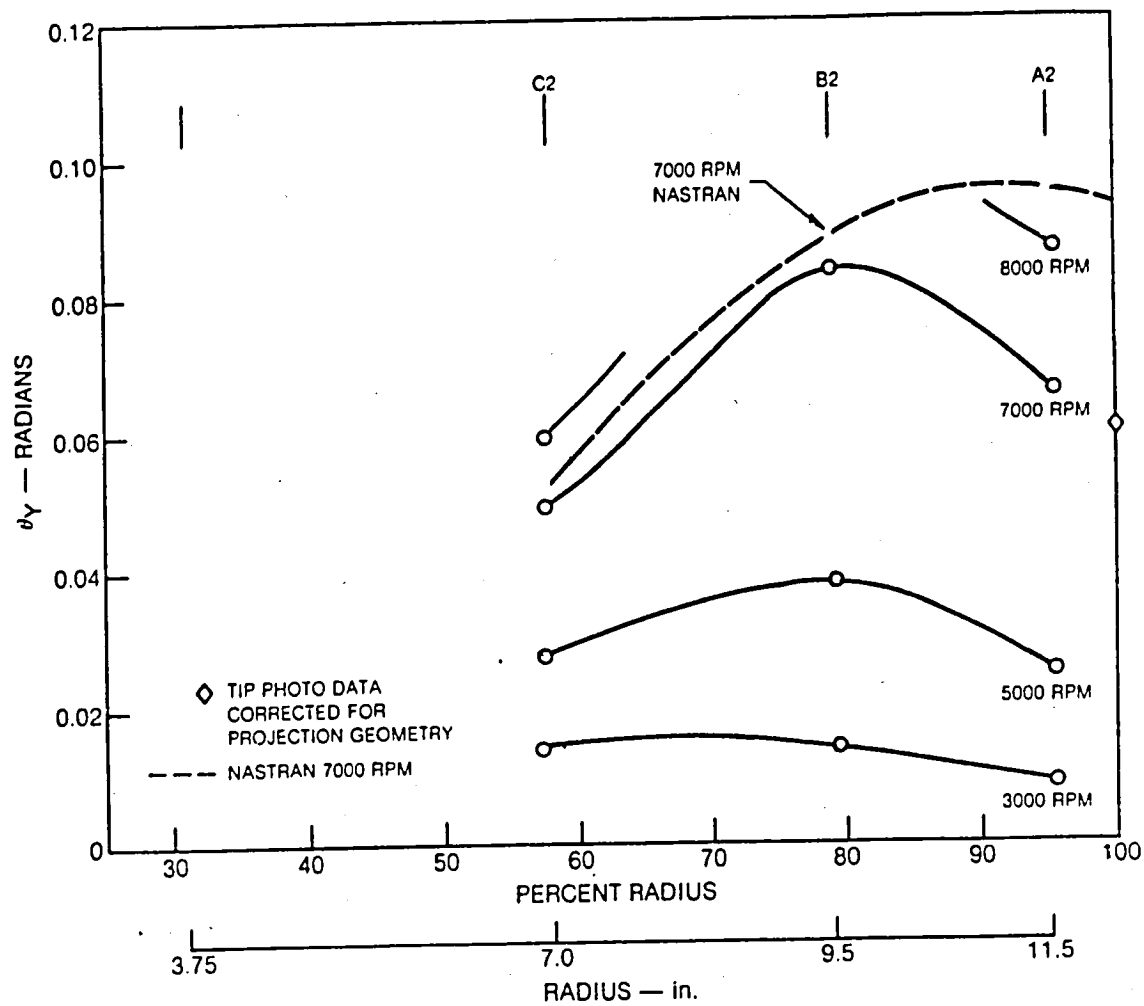

Fig. 17 Blade Twist θ_Y vs % Radius

84-4-7-14

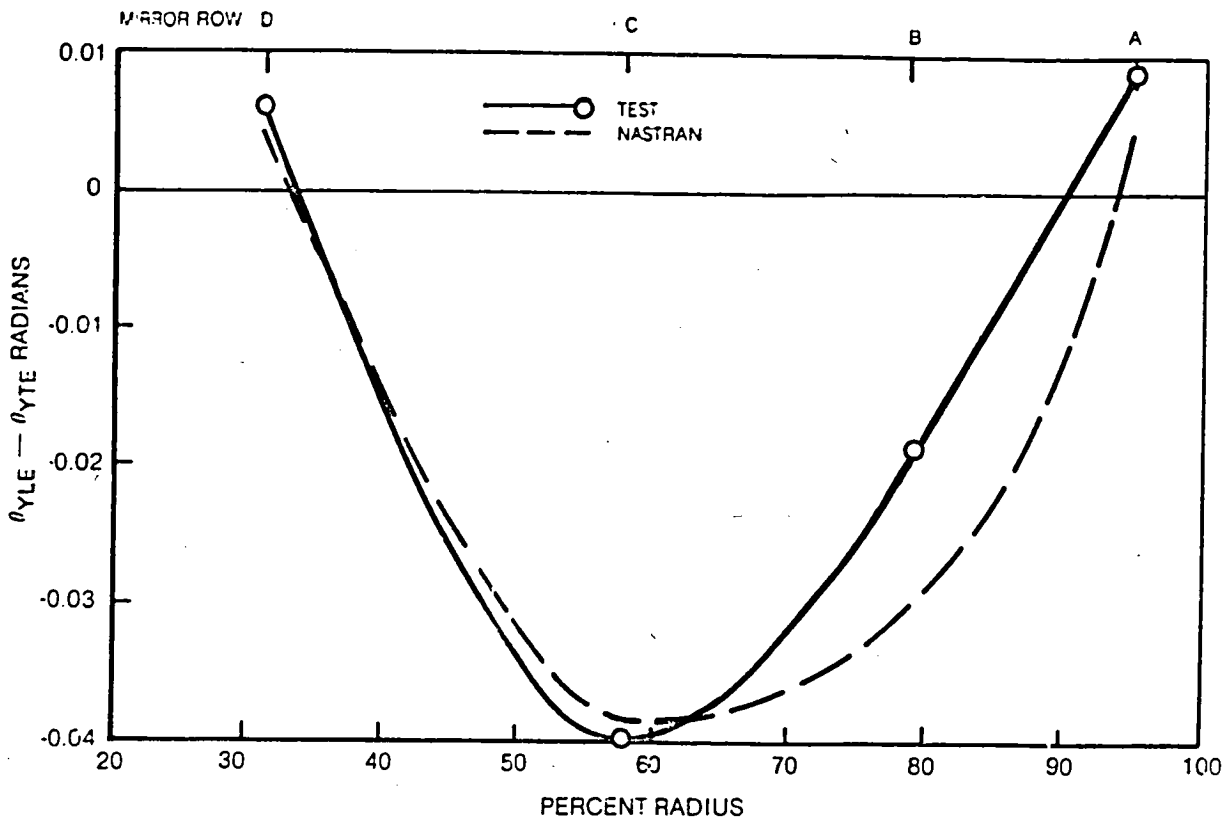

Fig. 18 Blade Uncamber vs Span at 7000 RPM

84-4-7-13

ORIGINAL PAGE IS
OF POOR QUALITY

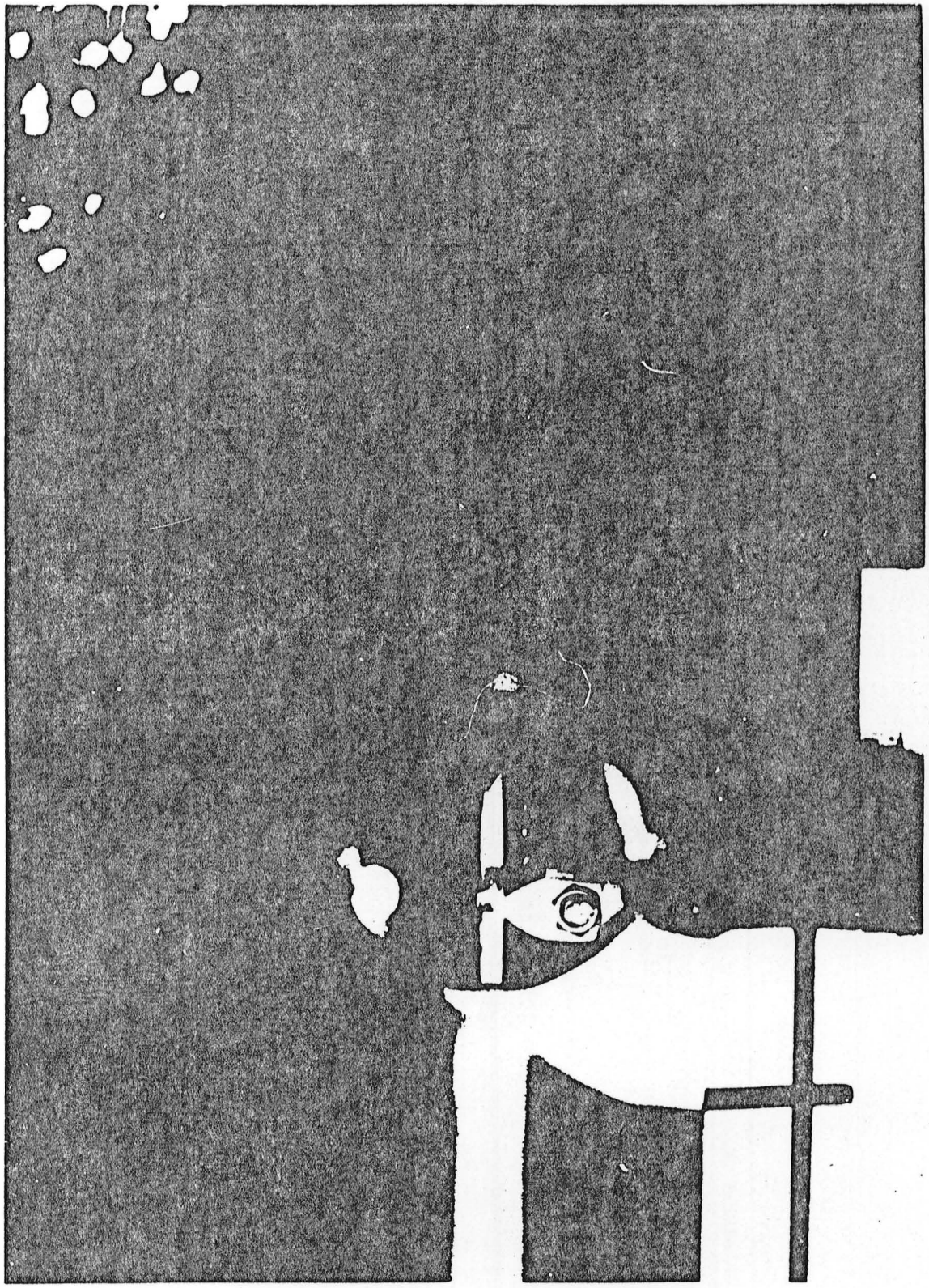

Fig. 19 Tip Photos — Superposition of 9000 RPM (Upper) on 1680 RPM (Lower)

84-4-7-6

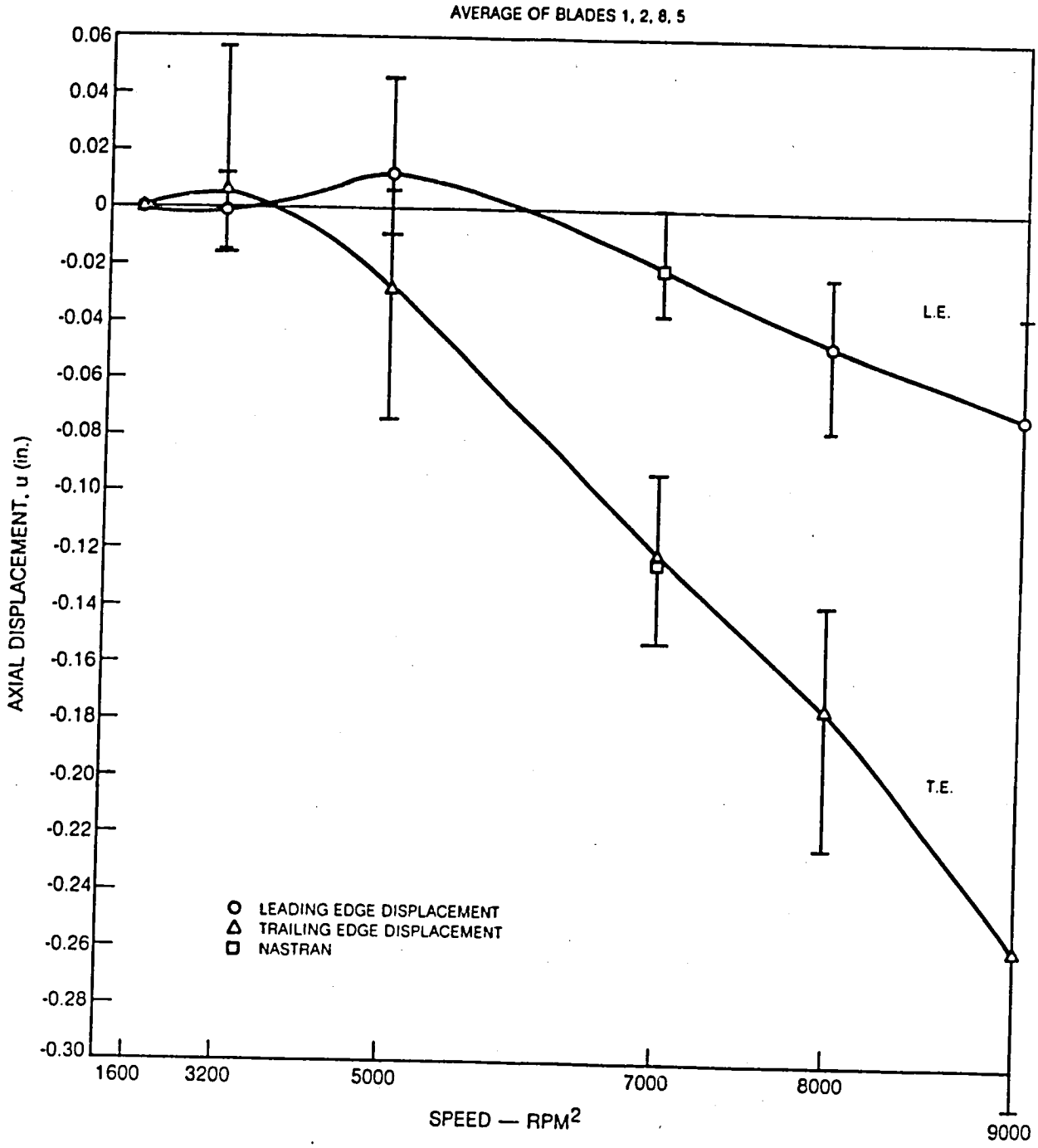

Fig. 20 SR5 Prop Fan Tip Photo Results — Based on Averaging — Axial Displacement

84-4-7-19

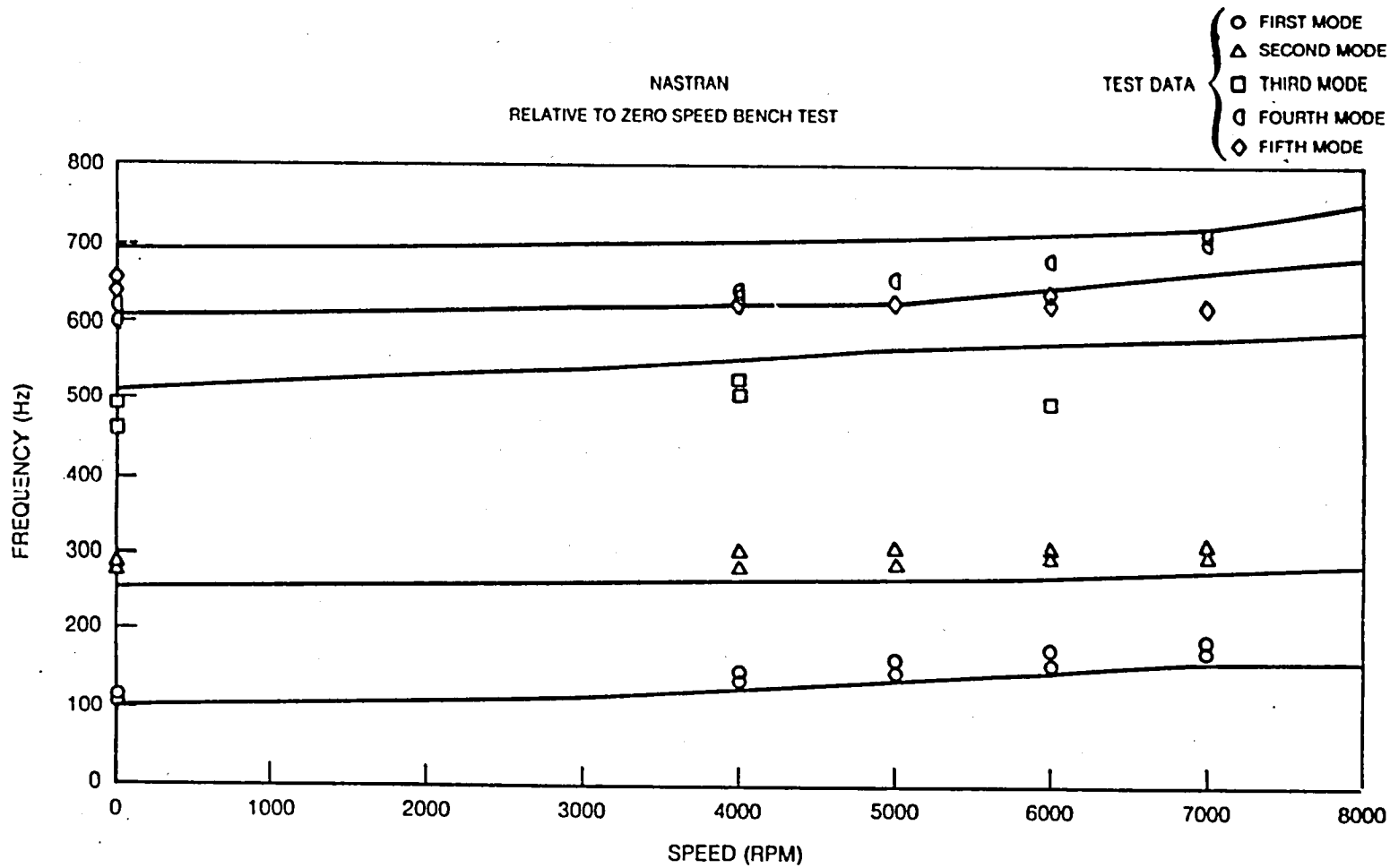

Fig. 21 SR5 Frequency vs Speed

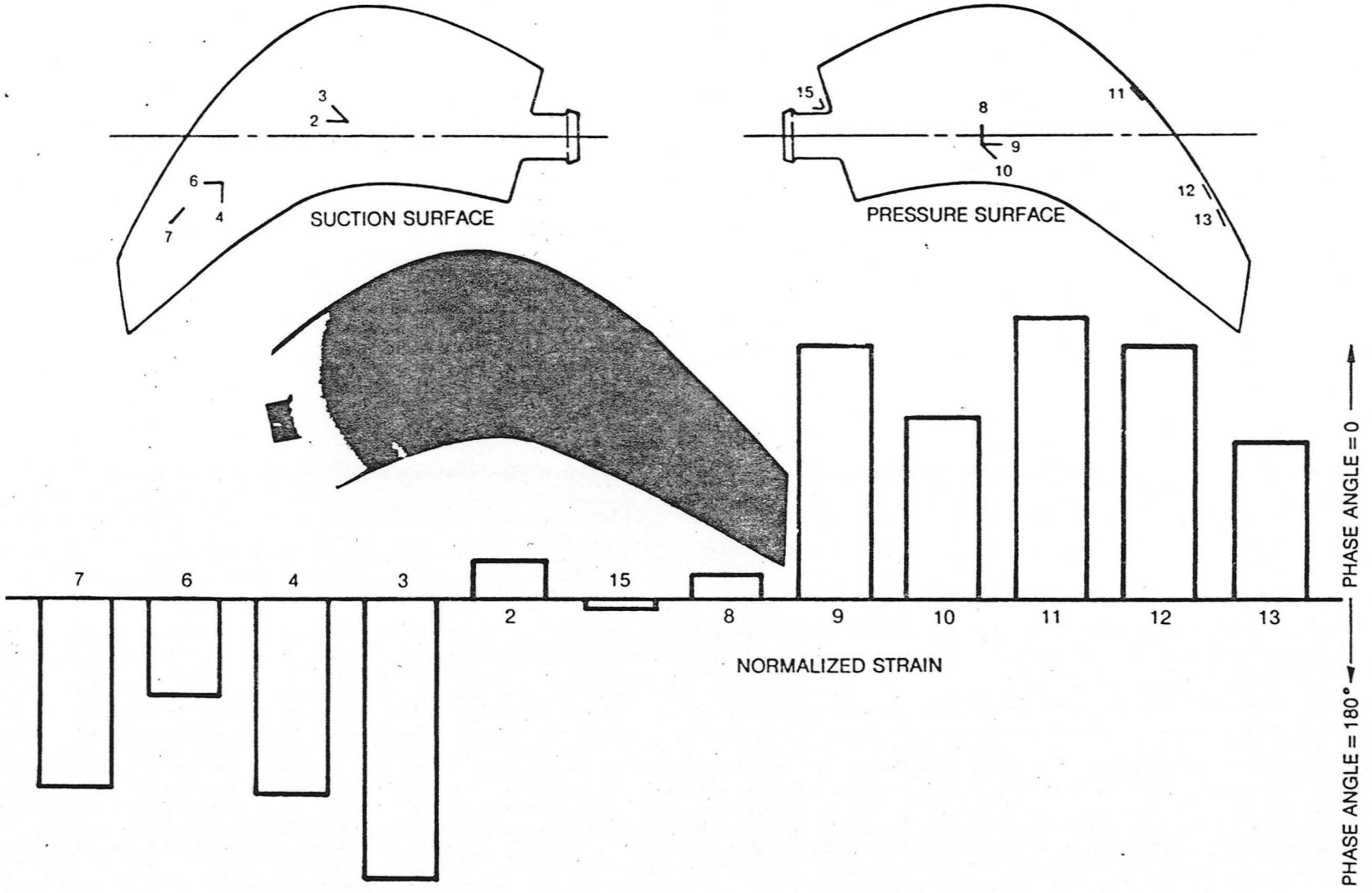

Fig. 22 SR5 Blade Vibratory Strain Distribution Bench Test Results — Mode 1

84-4-7-50

Fig. 23 SR5 Blade Vibratory Strain Distribution Bench Test Results — Mode 2

84-4-7-49

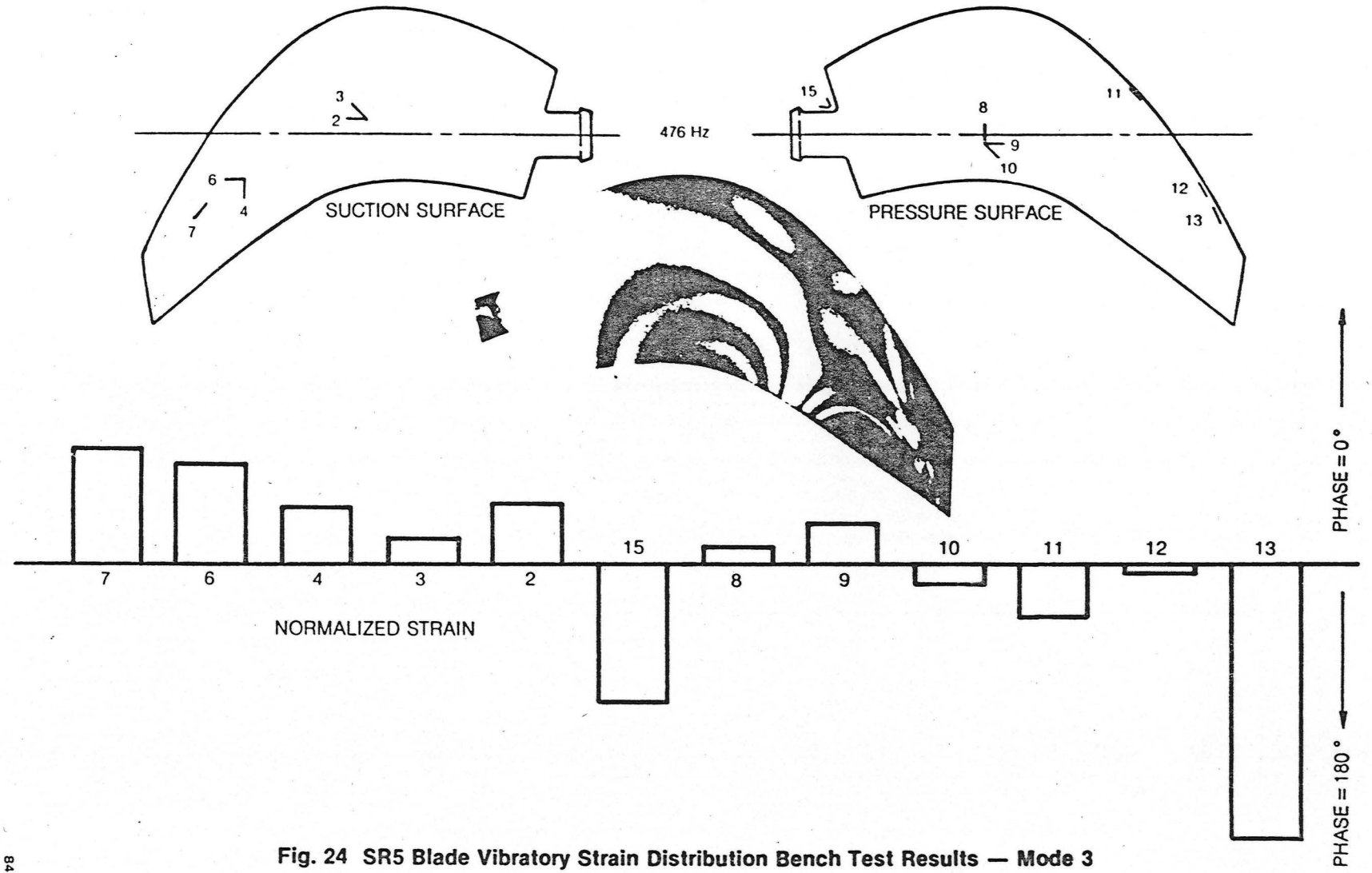

Fig. 24 SR5 Blade Vibratory Strain Distribution Bench Test Results — Mode 3

Fig. 25 SR5 Blade Vibratory Strain Distribution Bench Test Results — Mode 4

84-4-7-47

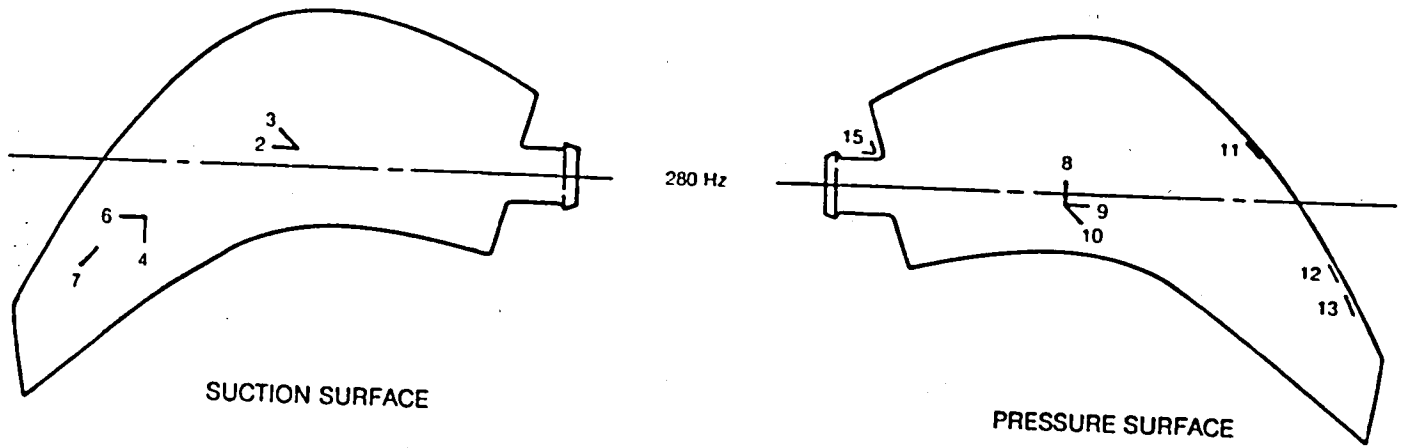

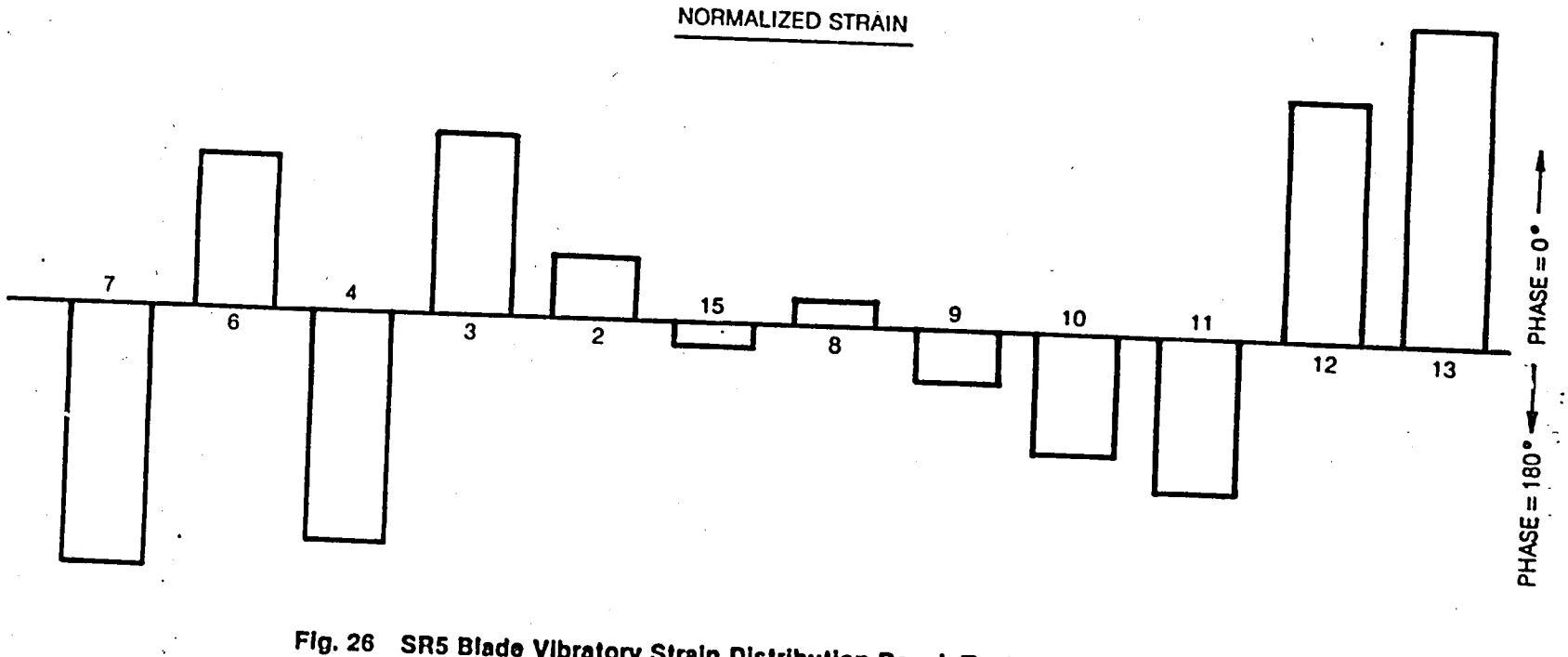

84-4-7-46

Fig. 26 SR5 Blade Vibratory Strain Distribution Bench Test Results — Mode 5

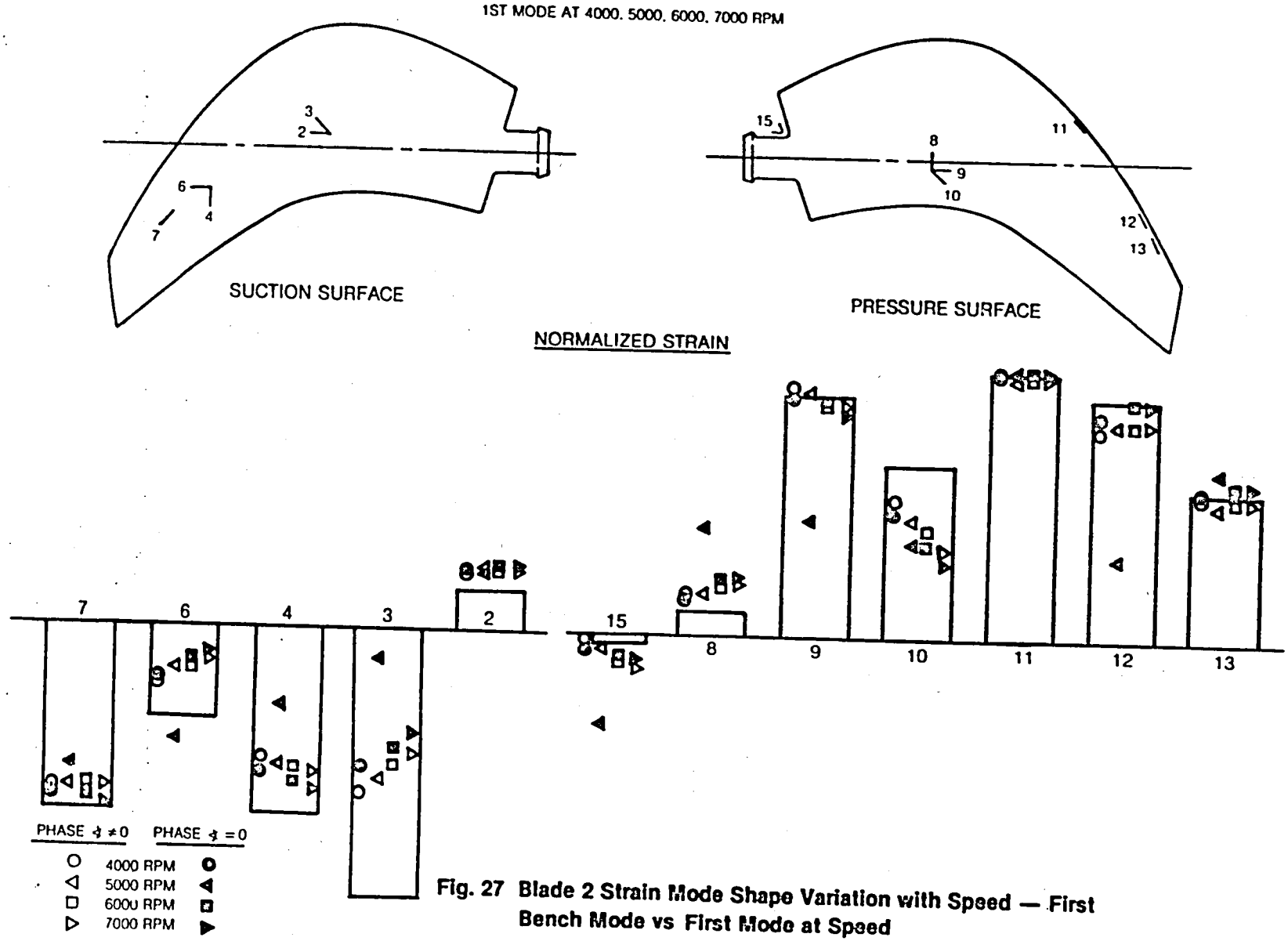

Fig. 27 Blade 2 Strain Mode Shape Variation with Speed — First Bench Mode vs First Mode at Speed

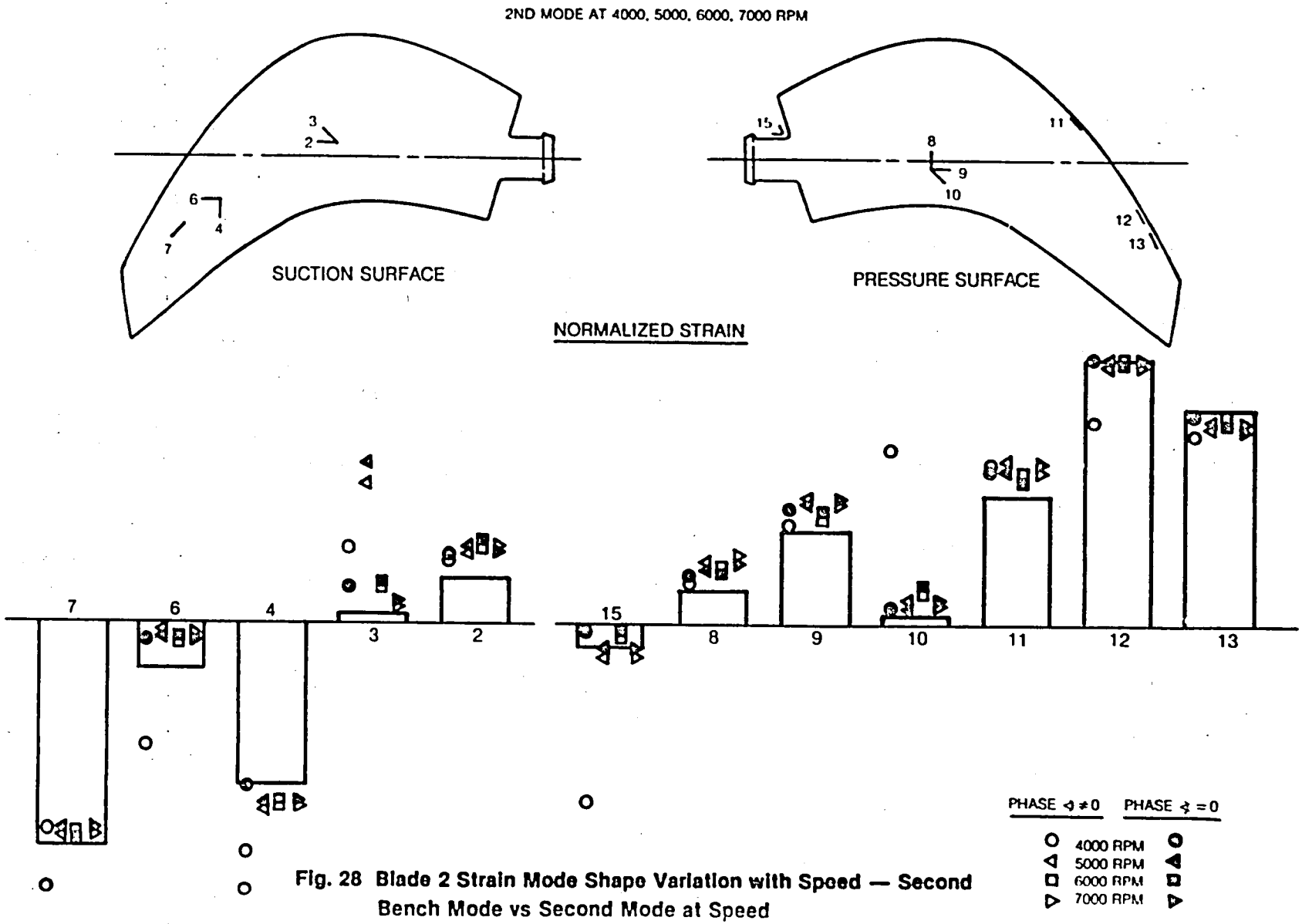

Fig. 28 Blade 2 Strain Mode Shape Variation with Speed — Second Bench Mode vs Second Mode at Speed

84-4-7-34

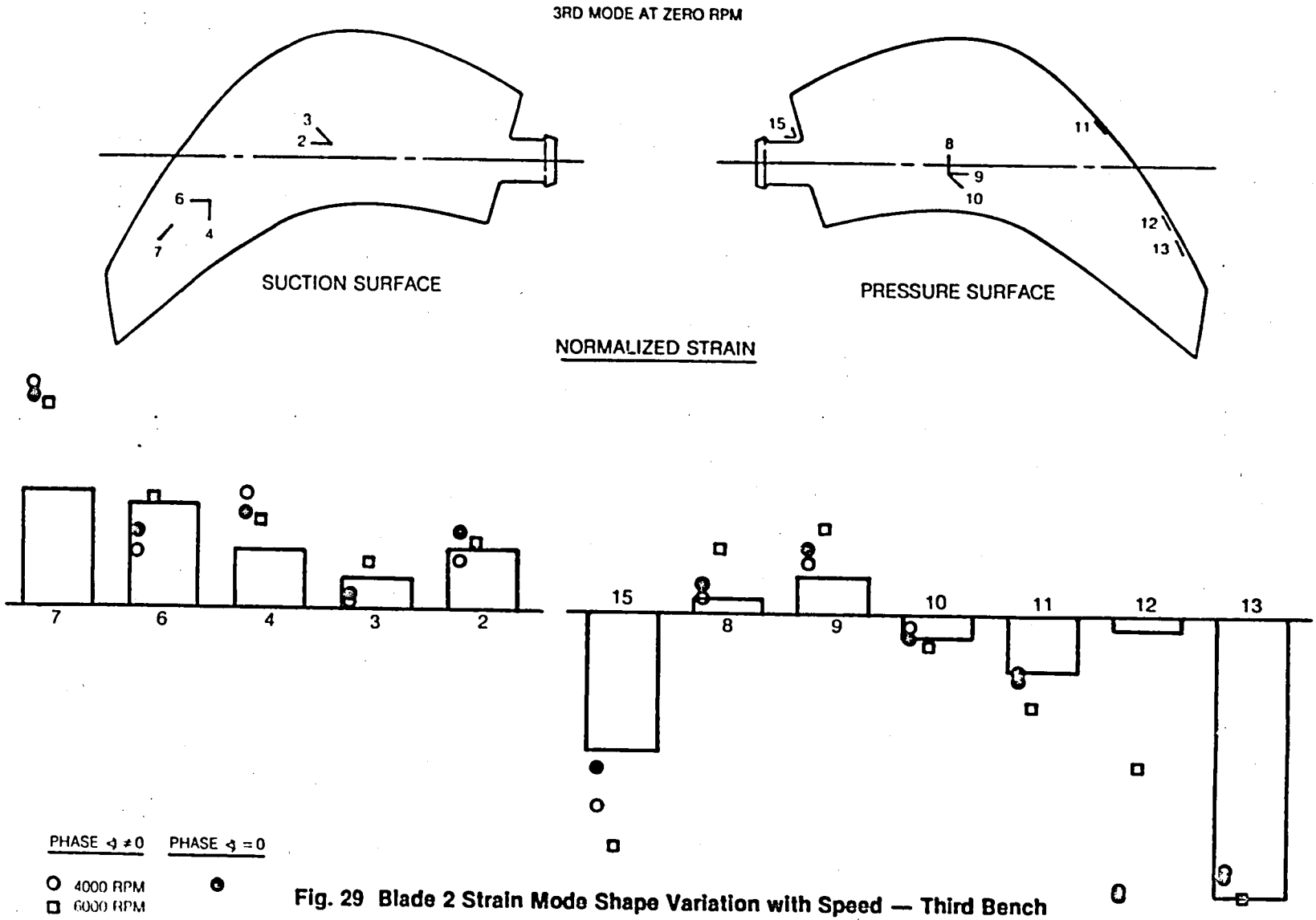

Fig. 29 Blade 2 Strain Mode Shape Variation with Speed — Third Bench Mode vs Third Mode at Speed

84-4-7-35

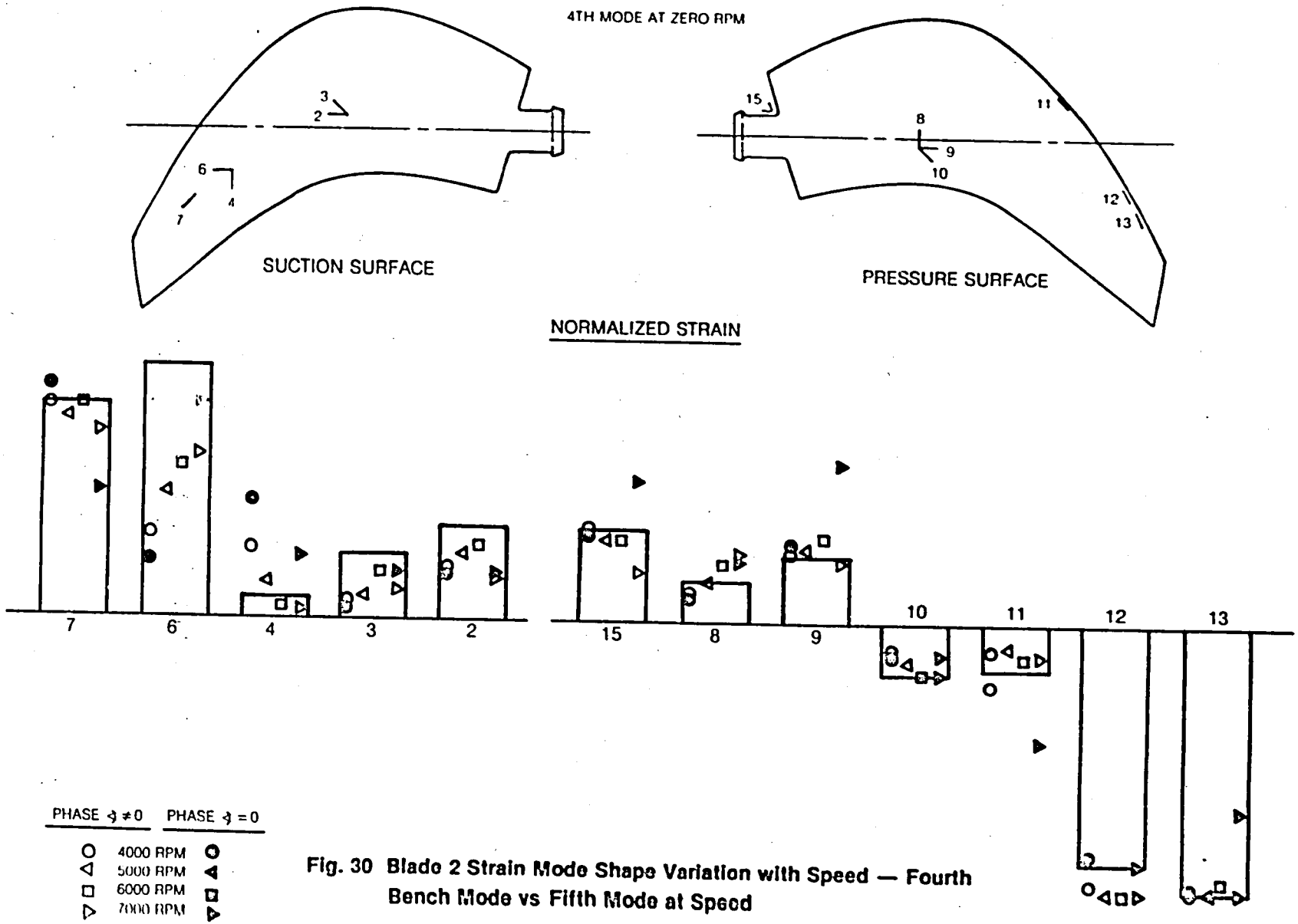

Fig. 30 Blade 2 Strain Mode Shape Variation with Speed — Fourth Bench Mode vs Fifth Mode at Speed

84-4-7-33

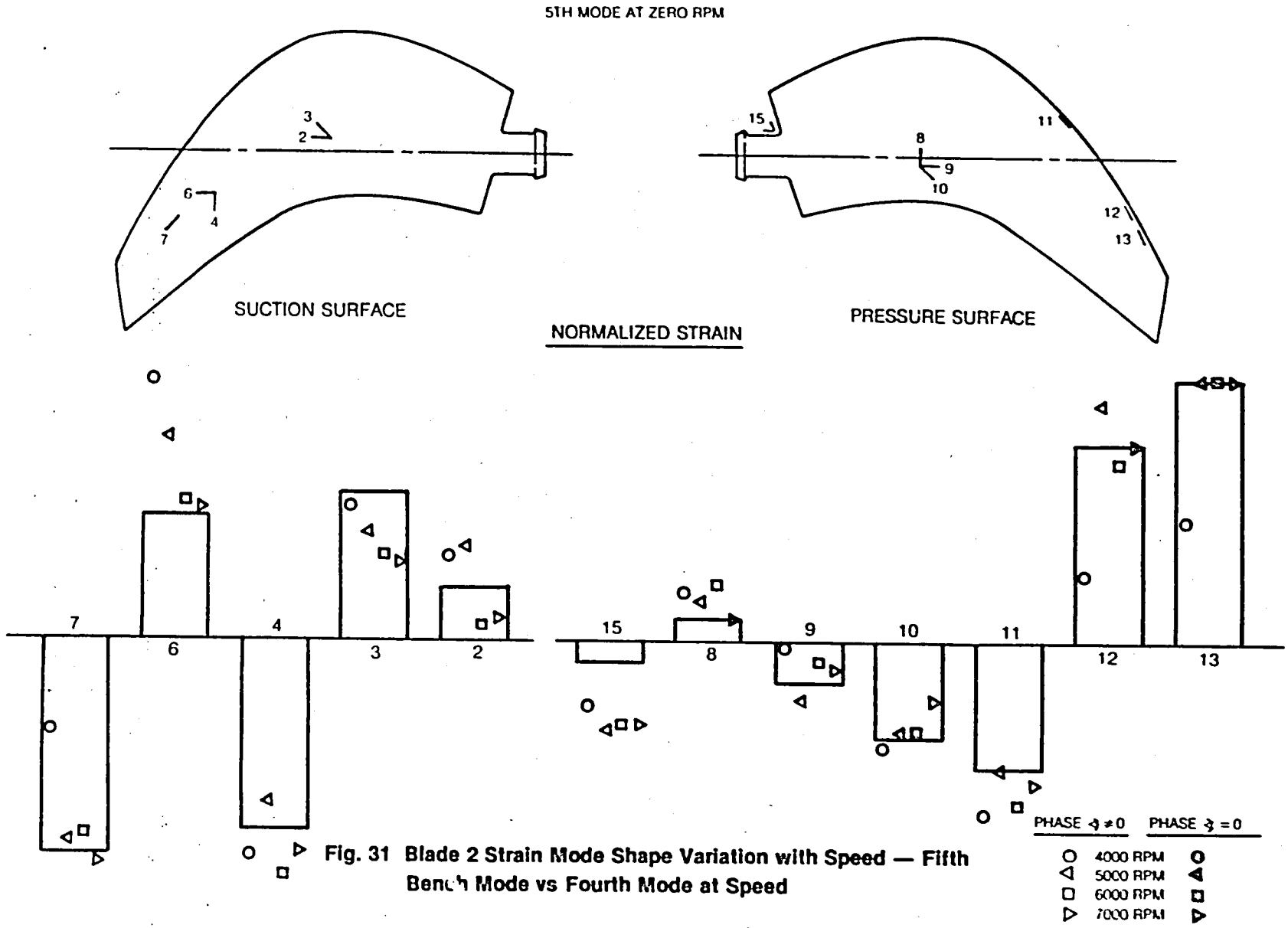

Fig. 31 Blade 2 Strain Mode Shape Variation with Speed — Fifth Bench Mode vs Fourth Mode at Speed

84-4-7-37

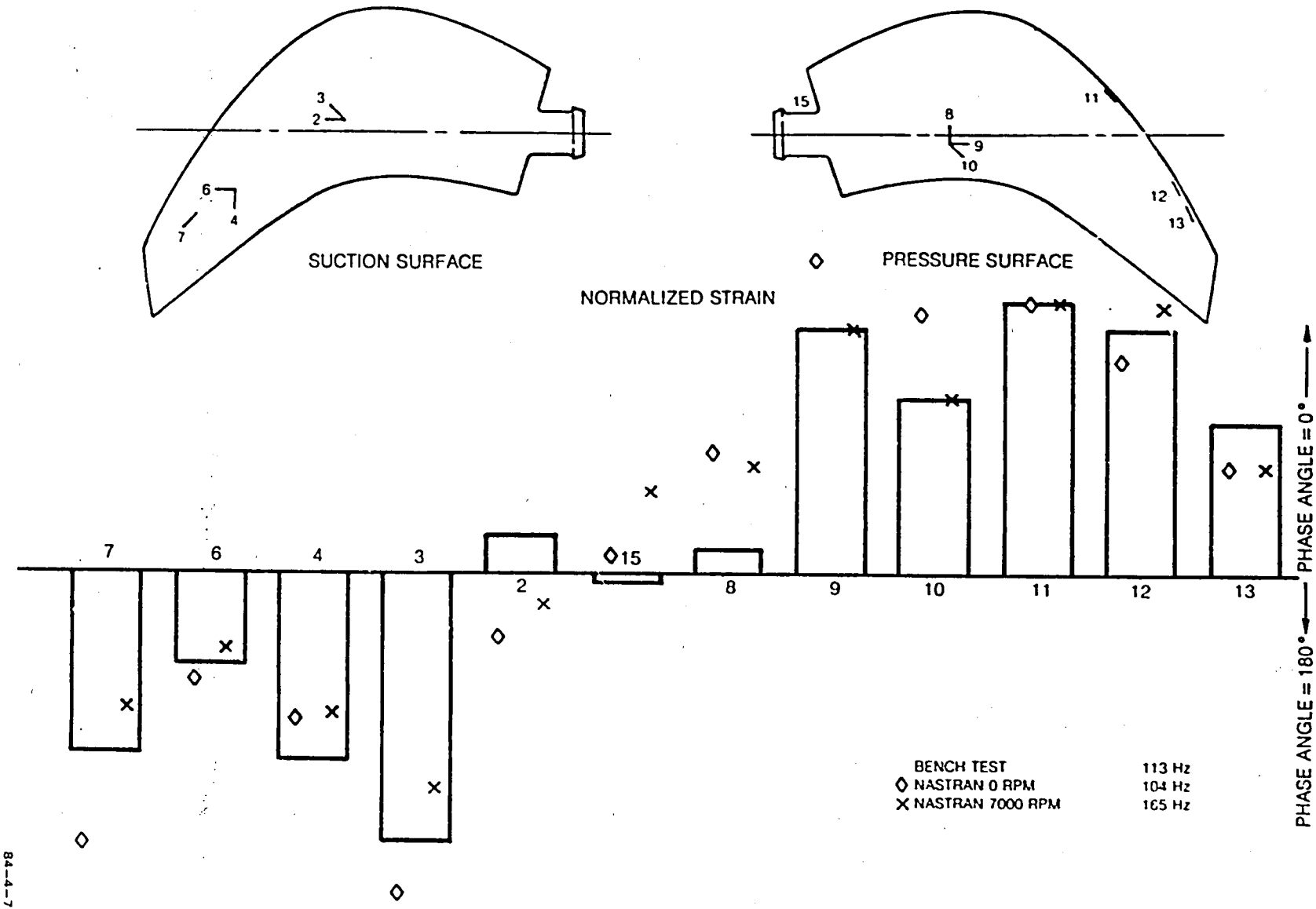

Fig. 32 SR5 Blade Vibratory Strain Distribution Comparison — Mode 1

84-4-7-11

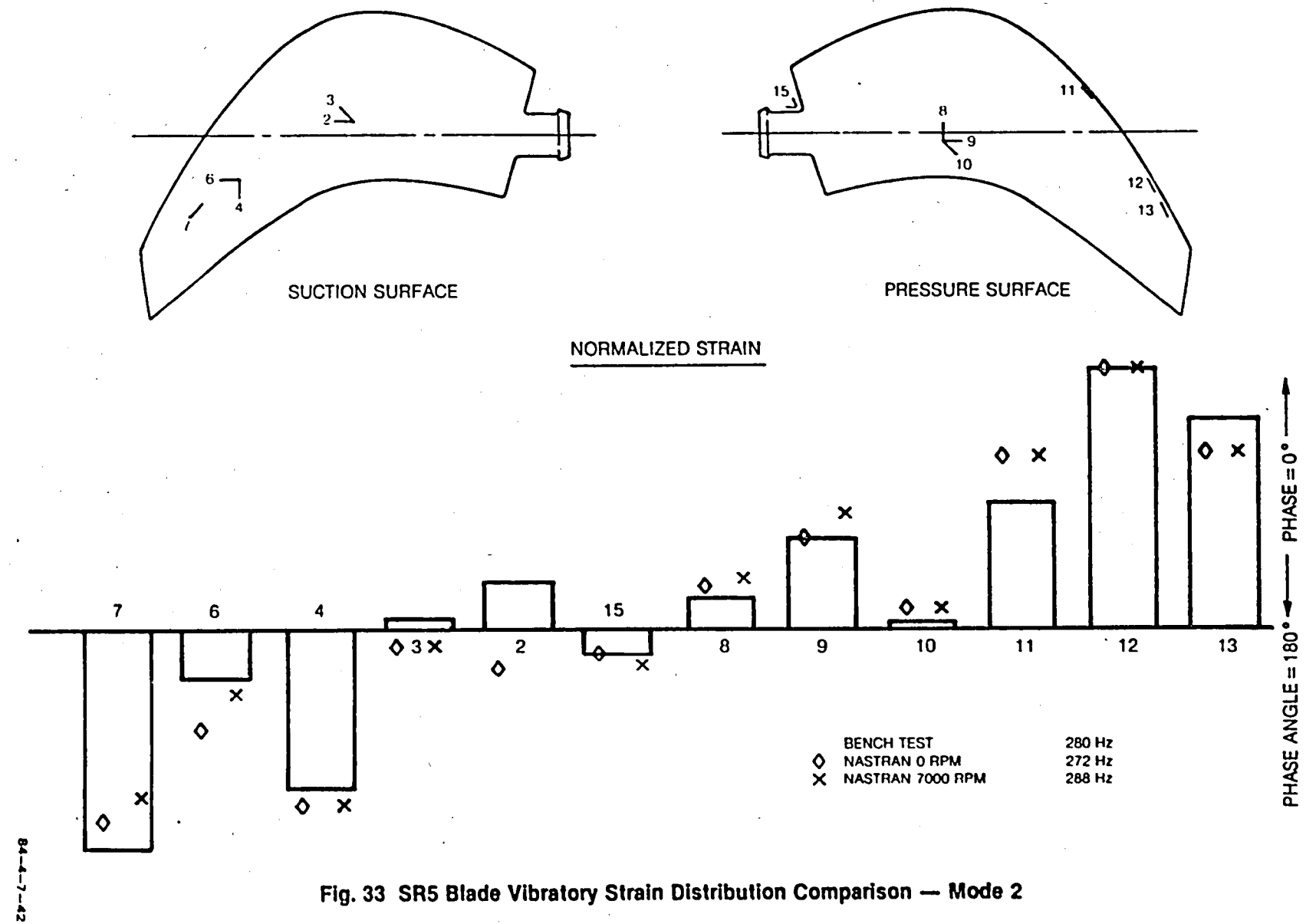

Fig. 33 SR5 Blade Vibratory Strain Distribution Comparison — Mode 2

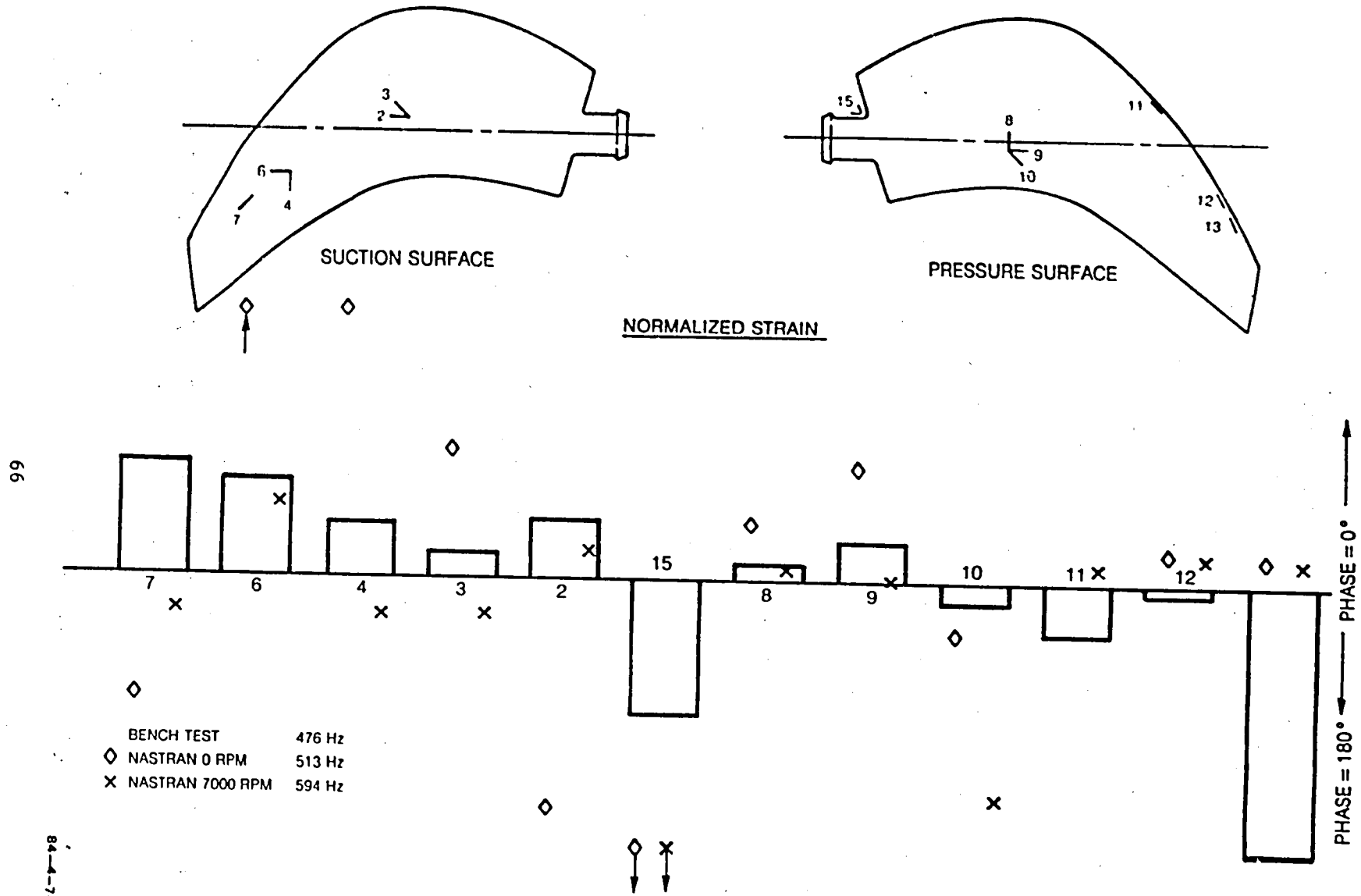

Fig. 34 SR5 Blade Vibratory Strain Distribution Comparison — Mode 3

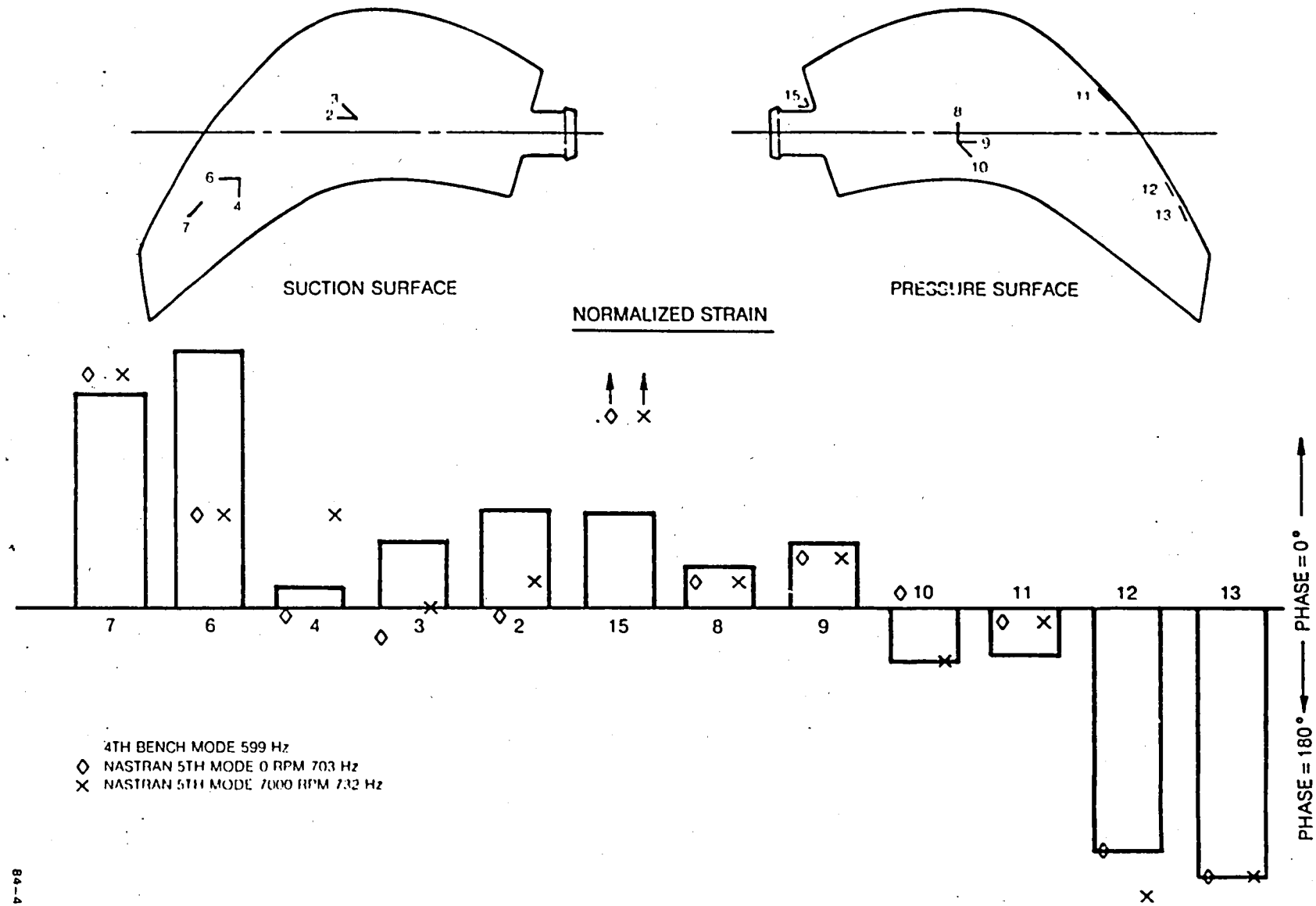

Fig. 35 SR5 Blade Vibratory Strain Distribution Comparison — Mode 4

84-4-7-44

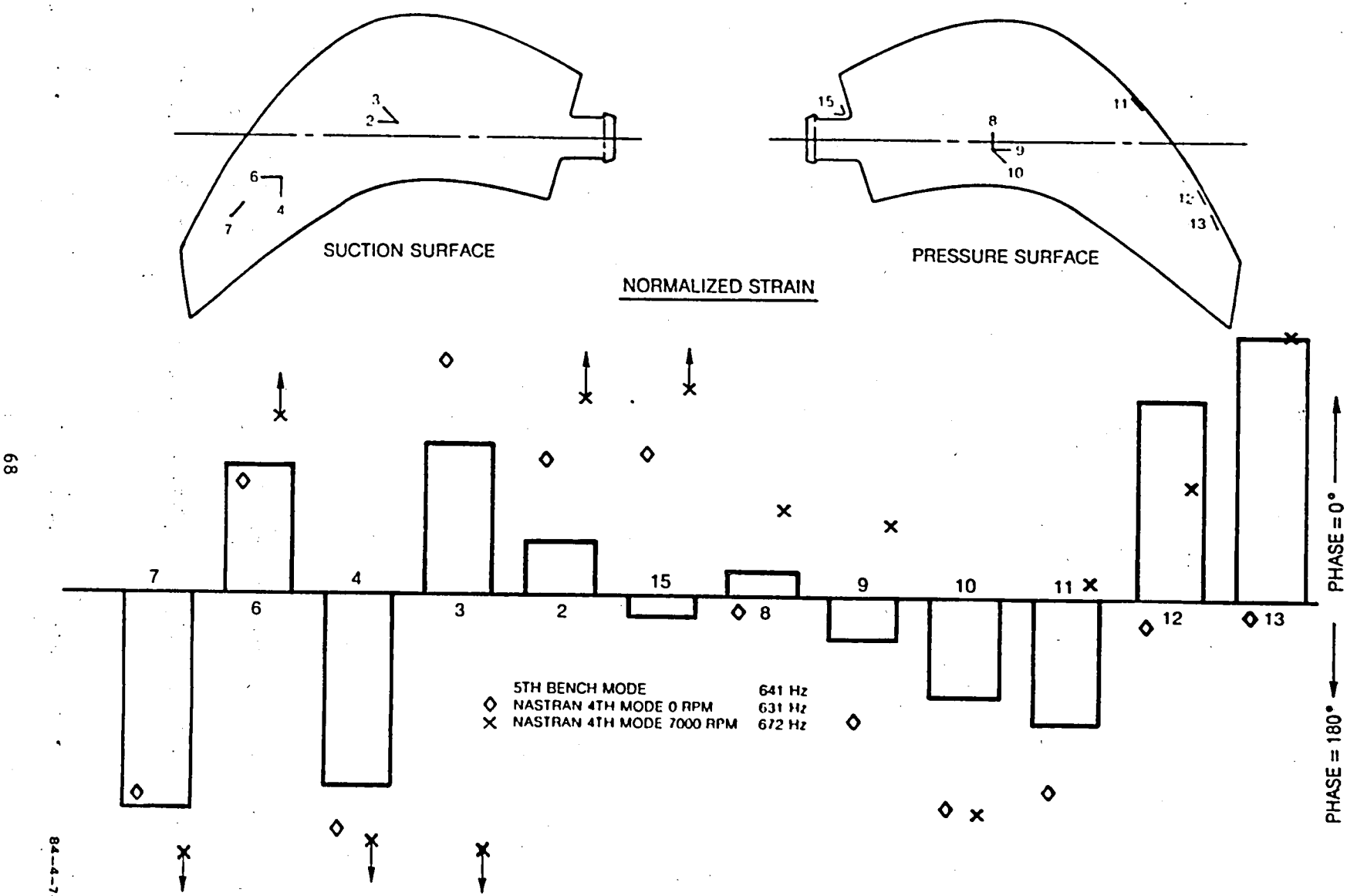

Fig. 36 SR5 Blade Vibratory Strain Distribution Comparison — Mode 5

APPENDIX I

MIRROR/LASER DATA

θ_Y vs. Speed

θ_Z vs. Speed

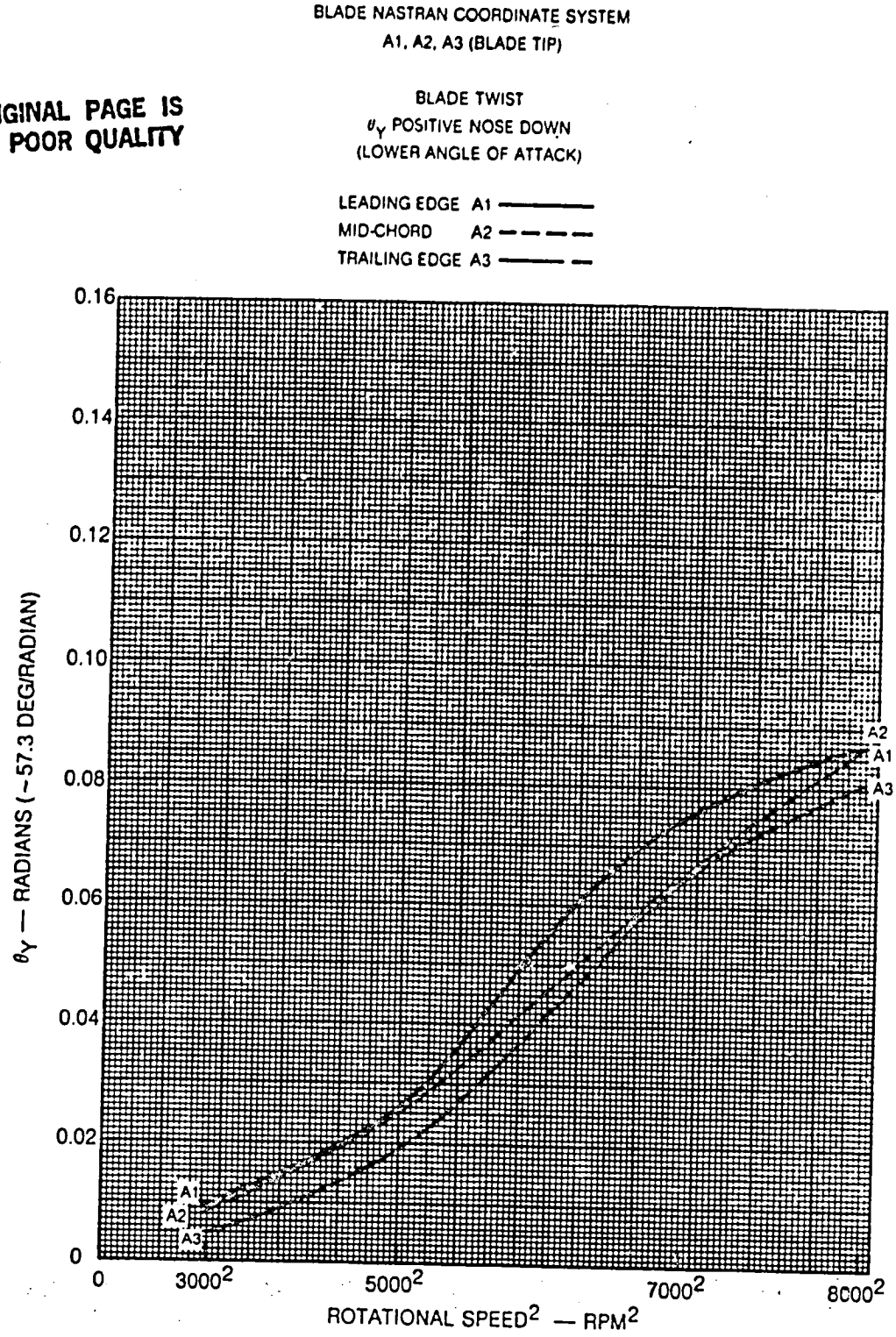

Fig. 1.1 θ_Y vs Rotational Speed^2

84-4-7-24

ORIGINAL PAGE IS
OF POOR QUALITY

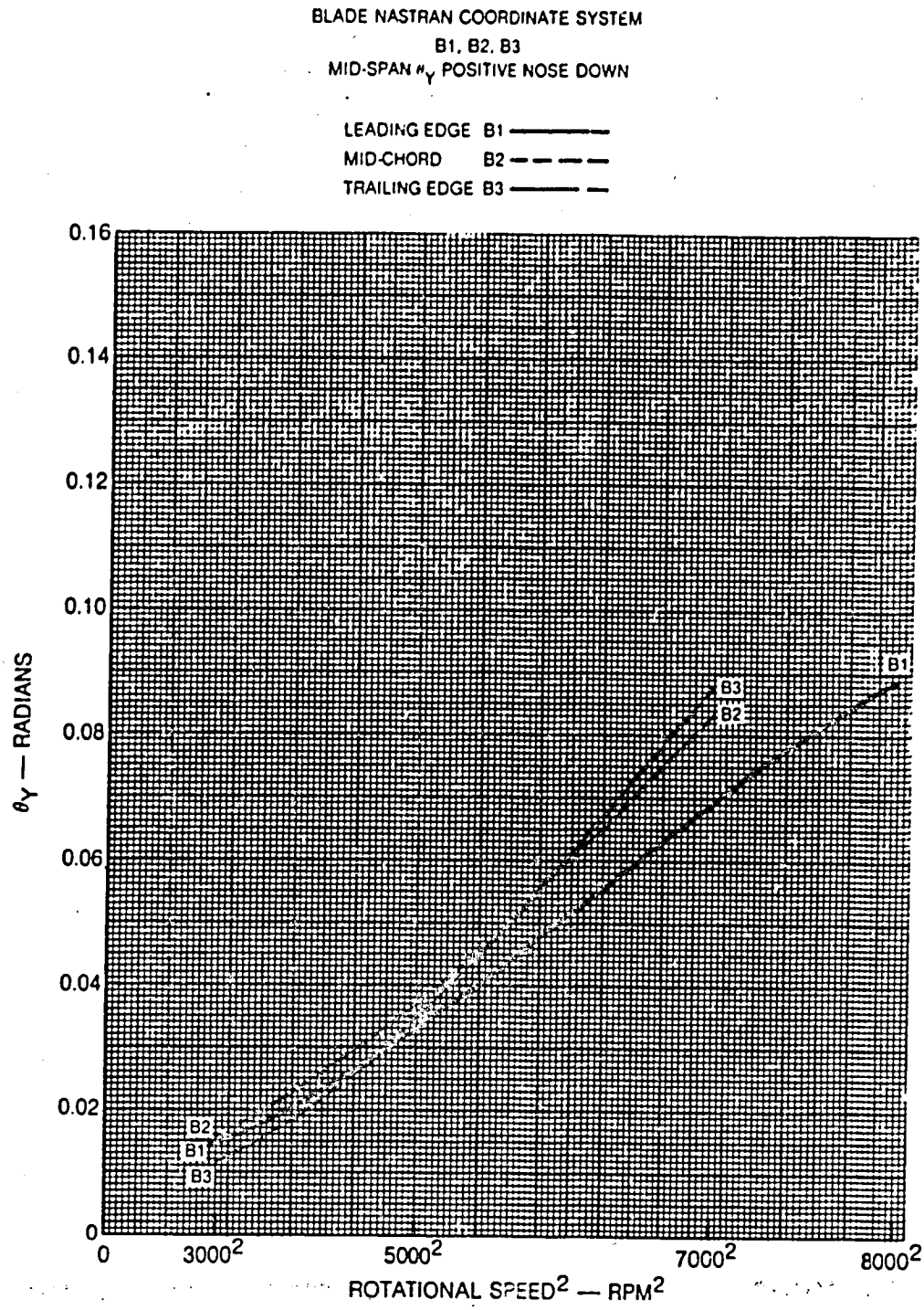

Fig. 1.2 θ_Y vs Rotational Speed^2

84-4-7-25

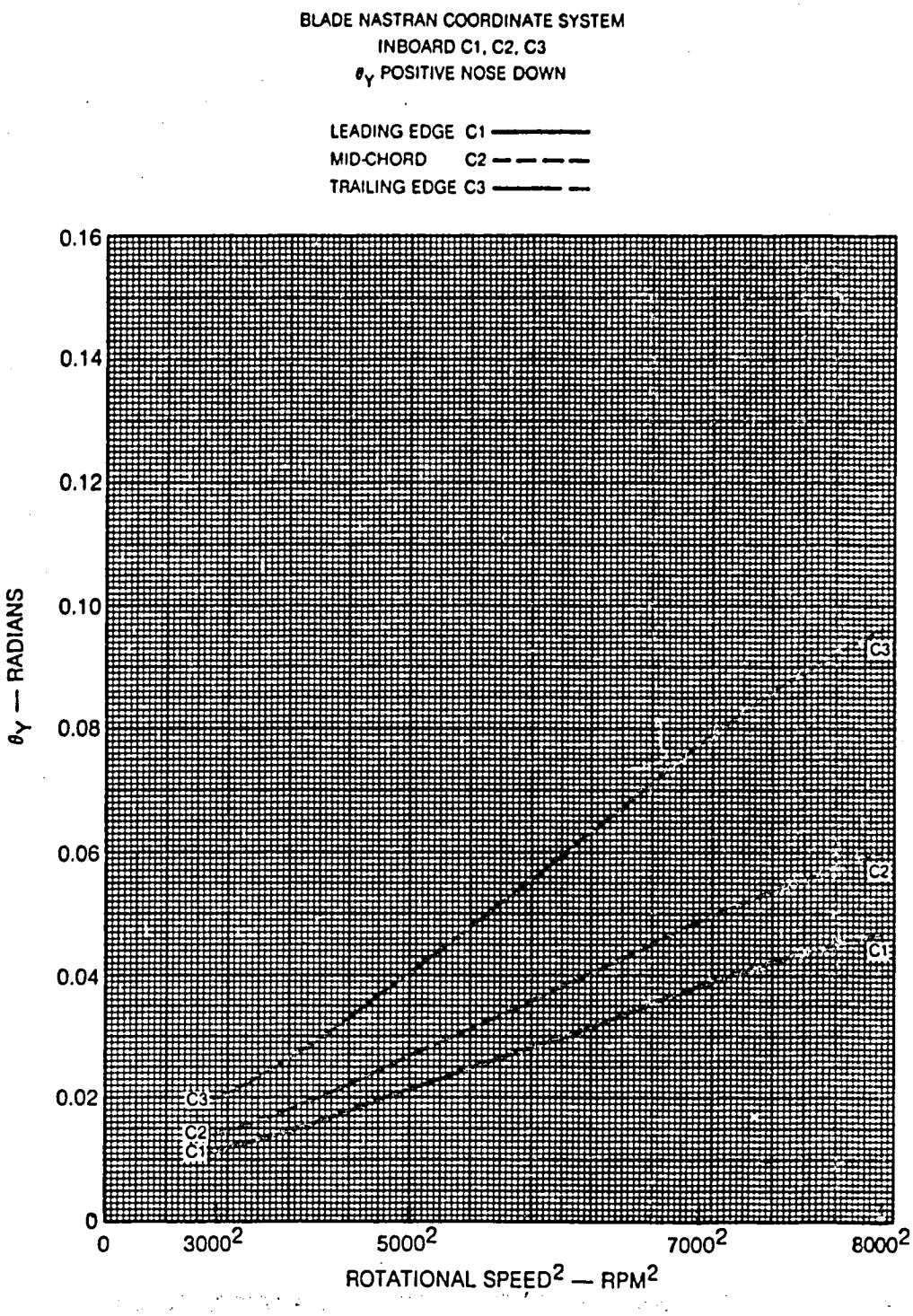

Fig. 1.3 θ_Y vs Rotational Speed^2

84-4-7-26

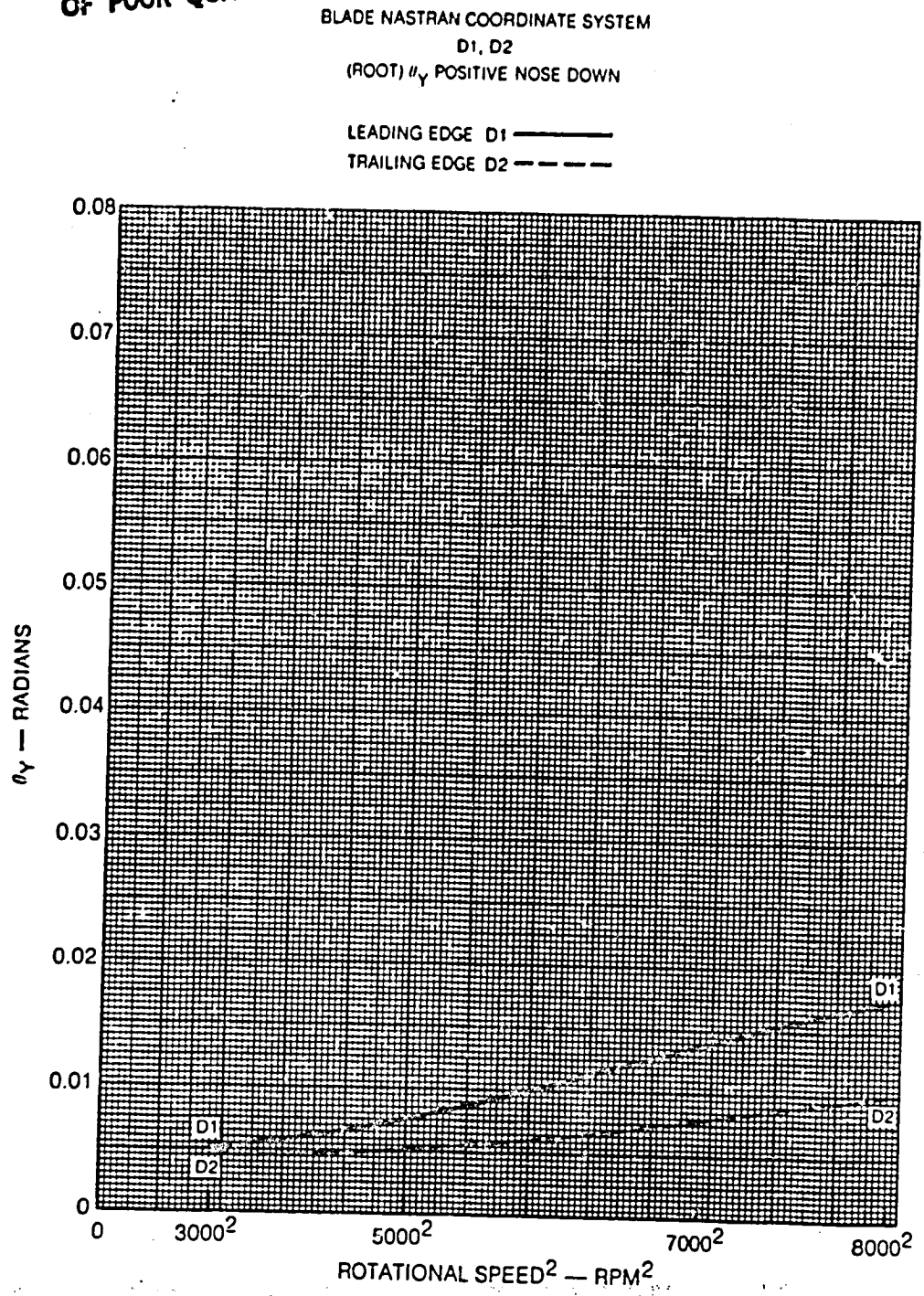

Fig. 1.4 θ_Y vs Rotational Speed^2

84-4-7-27

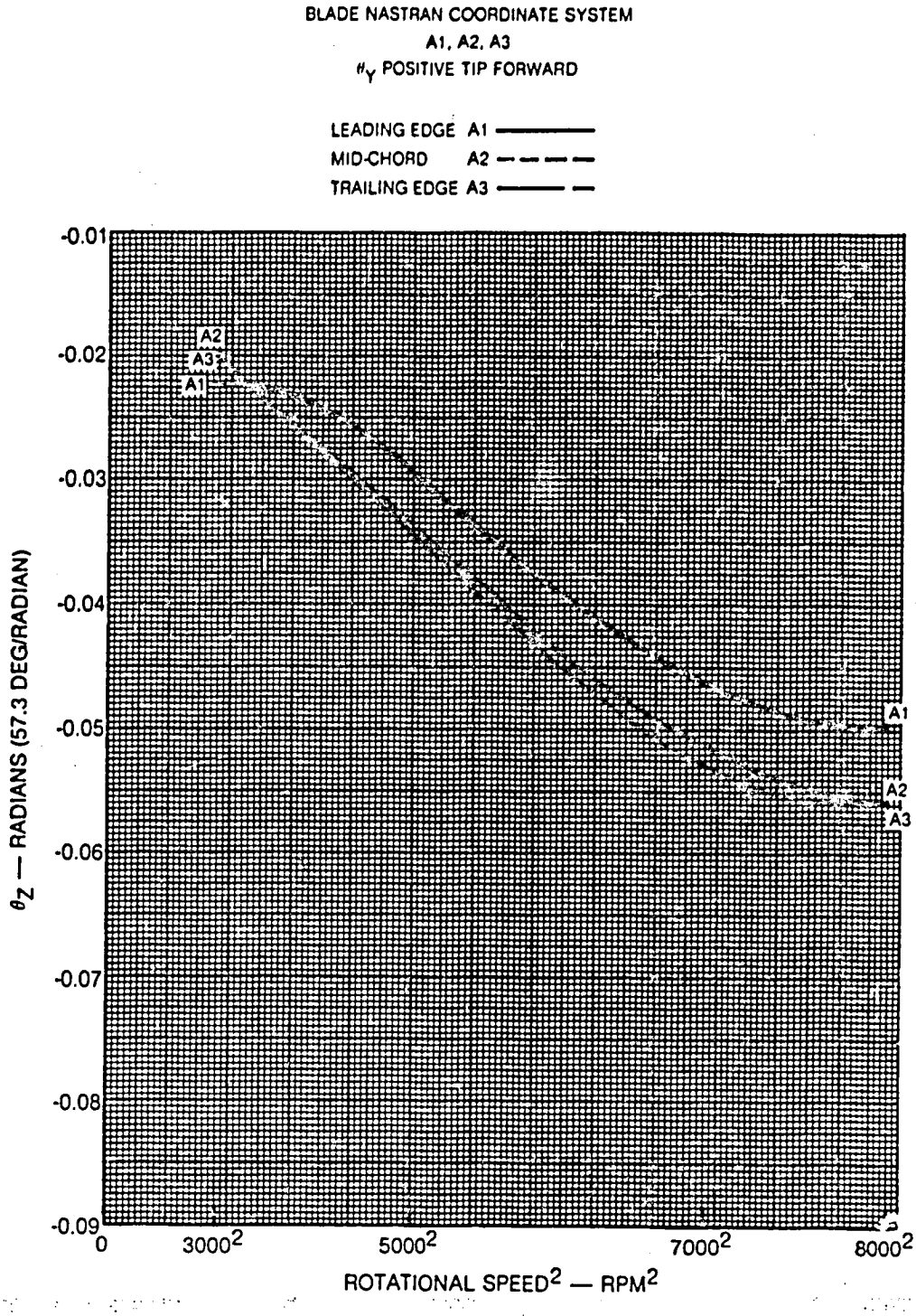

Fig. 1.5 θ_Z vs Rotational Speed^2

84-4-7-28

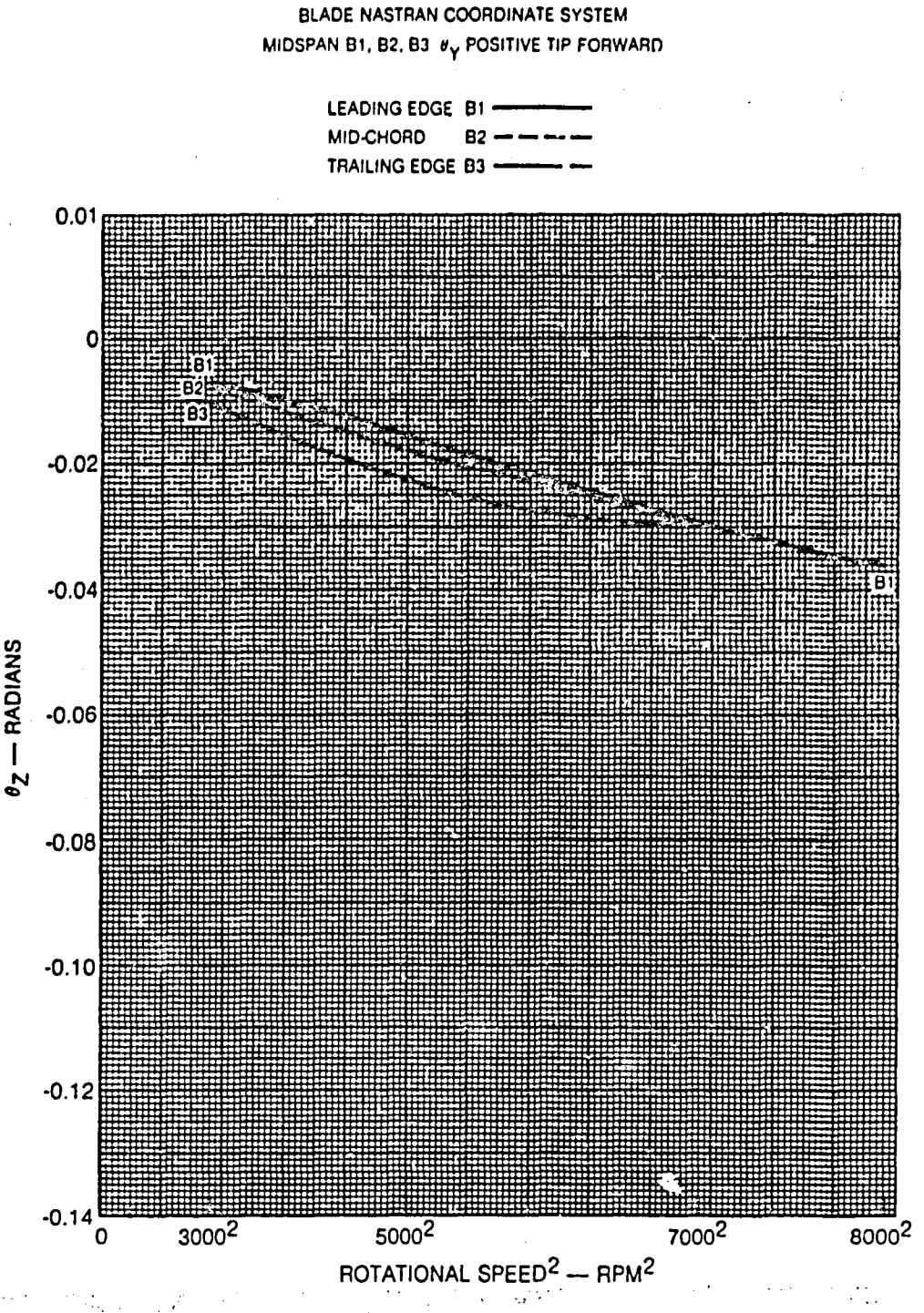

Fig. 1.6 θ_z vs Rotational Speed ^{2}

84-4-7-29

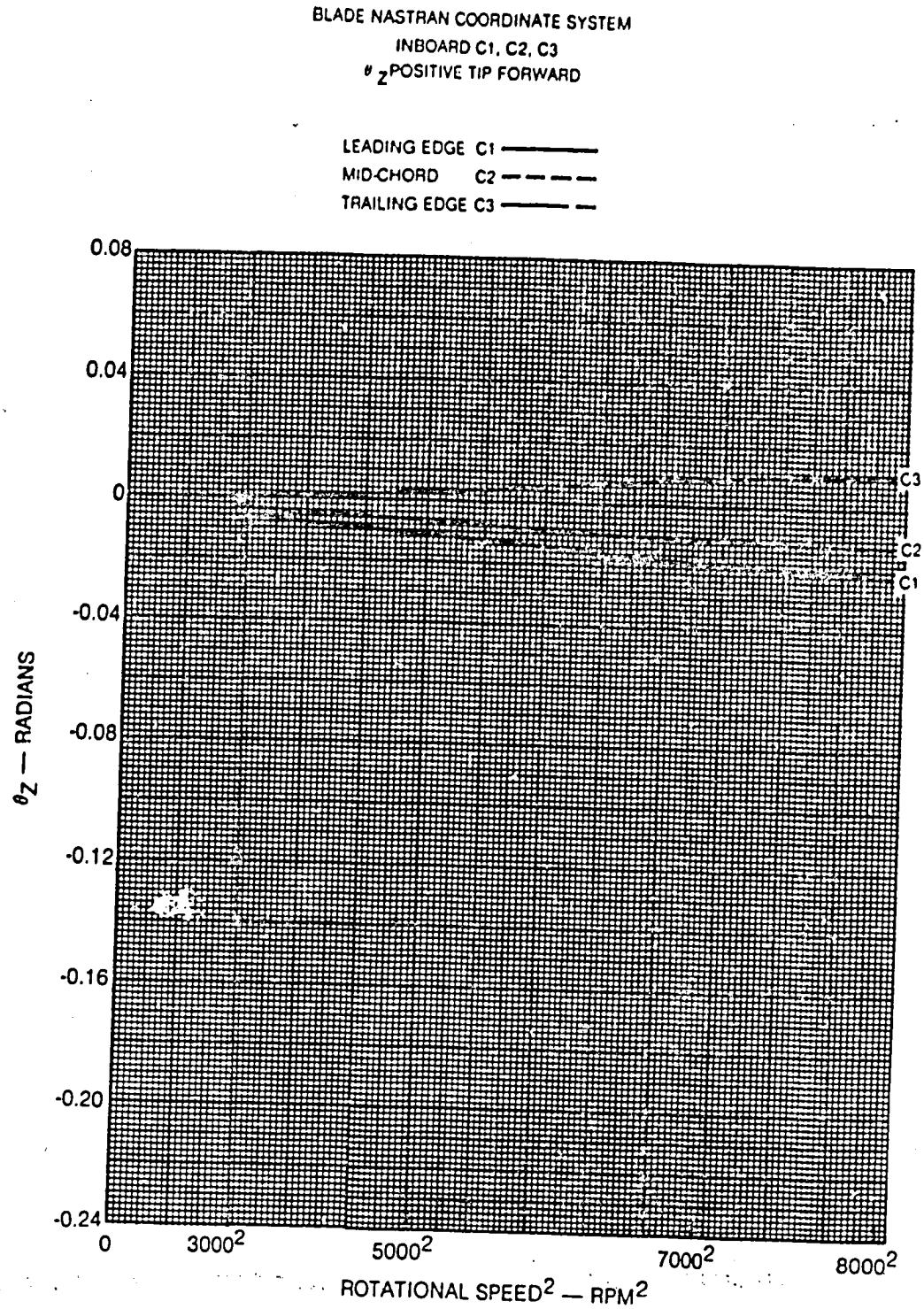

Fig. 1.7 θ_Z vs Rotational Speed^2

84-4-7-30

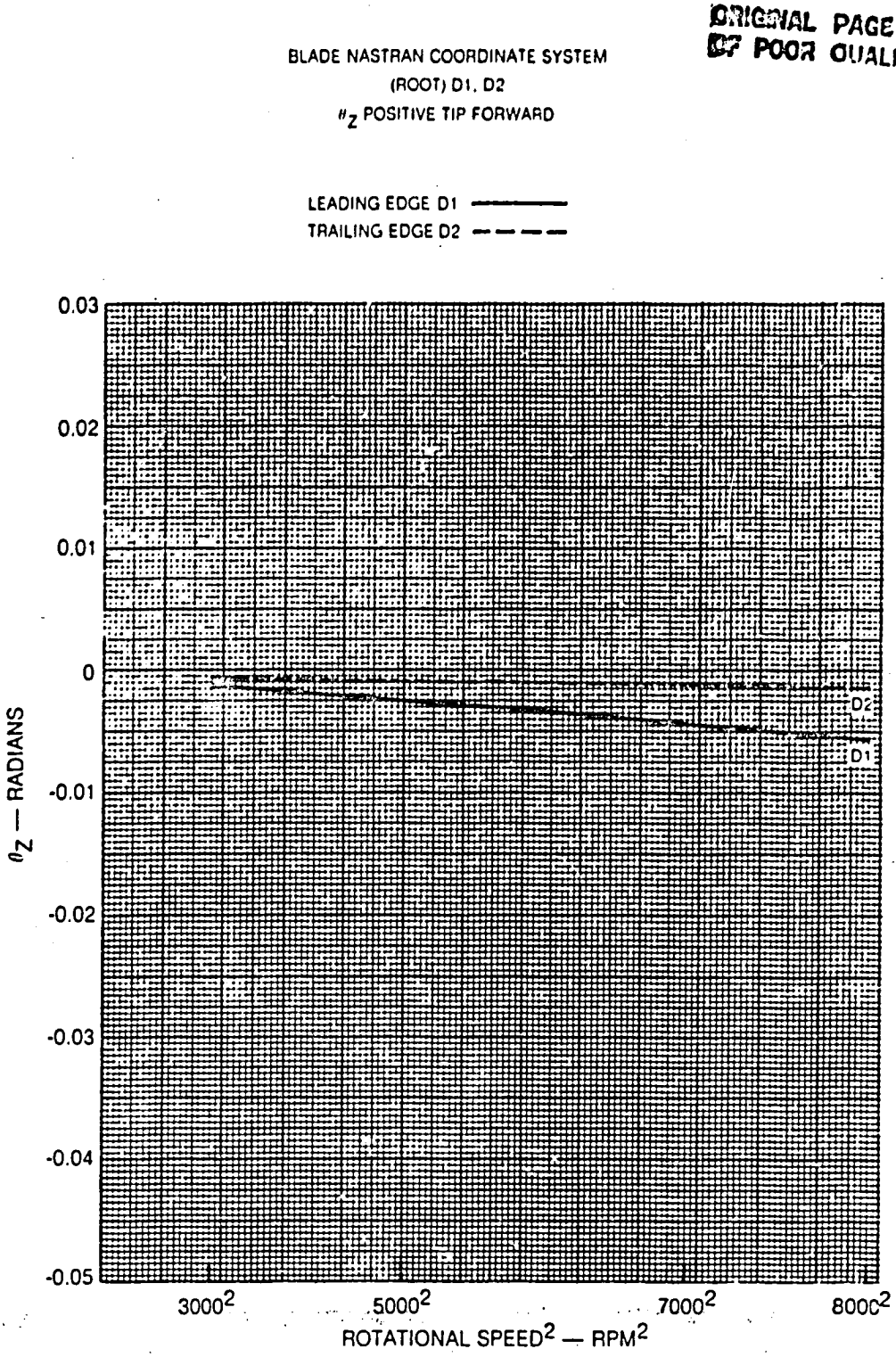

Fig. 1.8 $\overline{\theta}_Z$ vs Rotational Speed ^{2}

84-4-7-31

APPENDIX II

ANALYSIS OF PHOTOGRAPHS OF BLADE TIP VECTORS

The blade tip may be defined by a vector, V, from its leading corner to its trailing corner in an x,y,z coordinate system of the rotor. As shown in Figure 2.1, this coordinate system rotates by an angle ϕ, relative to the x',v',z' coordinate system of the spin rig. The camera was placed with its lens axis along y' and used to record photographs of the blade tip. In the photographs, the three-dimensional blade tip vector is recorded as a two-dimensional image on the surface of the film. The orientation of the image is the same as that of a shadow cast by the tip, through center of the camera lens, onto the film plane. This is a projection along the unit vector $\hat{s}$ in Figure 2.1, which is oblique to the film plane except when the blade tip is at the center of the image field. With the lens axis of the camera in the plane of rotation of the blade tip, the obliquity of $\hat{s}$ is completely defined by γ, the angle between $\hat{s}$ and $\hat{j}'$ in the $y'.z'$ plane.

The blade tip vector on the photographs may be related to the actual blade tip by three transformations. First the tip rotates due to blade deformation. Next, the entire rotor rotates to some position at which the photograph is exposed. Third, during the exposure of the photograph, the vector that results from the previous operations is projected onto the film plane through the center of the lens. Each of these transformations may be described as a matrix that operates on the original blade tip vector, and the total result is the product of the three matrices in the proper sequence.

Let the original blade tip vector be

$$V = \hat{i}V_x + \hat{j}V_y + \hat{k}V_z \ , \qquad (1)$$

where the subscripts x, y, and z denote the respective components of V. Deformation of the blade will rotate a surface element at the tip through an angle θ. If θ is small, the trailing corner will be displaced from its original position relative to the leading corner by a vector Δ where

$$\Delta = \theta \times V \ . \qquad (2)$$

Δ will lie at right angles to V and the new tip vector, V_d, will be

$$V_d = V + \Delta = V + \theta \times V \ . \tag{3}$$

The vector product in Eq. (3) can be written as a matrix operation, and this allows reformulation of the entire equation as follows.

$$V_d = V \ [I-\theta] \ , \tag{4}$$

where

$$[I-\theta] = \begin{bmatrix} 1 & \theta_Z & -\theta_Y \\ -\theta_Z & 1 & \theta_X \\ \theta_Y & -\theta_X & 1 \end{bmatrix} . \tag{5}$$

Note that if the surface element rotates about an axis parallel to the blade tip, the orientation of the tip vector is unchanged.

The rotation of the rotor relative to the laboratory can be described by a coordinate transformation matrix [T].

$$[T] = \begin{bmatrix} 1 & 0 & 0 \\ 0 & \cos\phi & \sin\phi \\ 0 & -\sin\phi & \cos\phi \end{bmatrix} . \tag{6}$$

The deformed and rotated tip vector, V_{dr}, is

$$V_{dr} = V \ [I-\theta][T] \ . \tag{7}$$

The projection V_{dr} through the center of the lens onto the film plane is described by the oblique projection matrix, $[P_{js}]$.

$$[P_{js}] = [I] - \hat{j}' \otimes \hat{s} / \hat{j}' \cdot \hat{s} \ , \tag{8}$$

where $\otimes$ indicates a matric product (dyadic, Ref. 9, p. 170) of the two vectors and $\cdot$ indicates a scalar product. This matrix may be evaluated to be

$$[P_{js}] = \begin{bmatrix} 1 & 0 & 0 \\ 0 & 0 & \tan\gamma \\ 0 & 0 & 1 \end{bmatrix} . \qquad (9)$$

The parameter $\tan\gamma$ accounts for the spherical perspective of the camera. The angle γ is related to the angle ϕ as shown in Figure 2.2. If L and R are the distance respectively from camera lens and the blade tip to the center of the rotor, then

$$\sin\gamma = \sin(\phi-\phi_o)/\left[1+(L/R)^2 - (2L/R)\cos(\phi-\phi_o)\right]^{1/2} . \qquad (10)$$

ϕ_o is the angle at which the blade tip is located in the rotor coordinate system.

The final equation for the image of the blade tip vector may be written as

$$V_c = V[I-\theta][T][P_{js}] . \qquad (11)$$

The matrix products may be evaluated as follows:

$$[T][P_{js}] = \begin{bmatrix} 1 & 0 & 0 \\ 0 & 0 & \sin\phi+\cos\phi\tan\gamma \\ 0 & 0 & \cos\phi-\sin\phi\tan\gamma \end{bmatrix} , \qquad (12)$$

and

$$[I-\theta][T][P_{js}] = \begin{bmatrix} 1 & 0 & \theta_Z(\sin\phi+\cos\phi\tan\gamma) - \theta_Y(\cos\phi-\sin\phi\tan\gamma) \\ -\theta_Z & 0 & (\sin\phi+\cos\phi\tan\gamma) + \theta_X(\cos\phi-\sin\phi\tan\gamma) \\ \theta_Y & 0 & -\theta_X(\sin\phi+\cos\phi\tan\gamma) + (\cos\phi-\sin\phi\tan\gamma) \end{bmatrix} . \qquad (13)$$

Equation (13) may be simplified by the following substitutions.

$C = \sin\phi + \cos\phi\tan\gamma$, and

$D = \cos\phi - \sin\phi\tan\gamma$

Substituting these into Eq. (13) and the result into Eq. (11) gives

$$V_c = \hat{i}\{V_x - V_y\theta_Z + V_z\theta_Y\} + \hat{k}\{C(V_x\theta_Z + V_y - V_z\theta_X) - D(V_x\theta_Y - V_y\theta_X - V_z)\} \quad . \qquad (14)$$

With the additional substitutions,

$A = V_z/V_x$, and

$B = V_y/V_x$,

it is possible to describe the angle of the image of the blade tip in the photograph as,

$$\cot\alpha = \{A(D - C\theta_X) + B(C + D\theta_X) + C\theta_Z - D\theta_Y\}/\{1 - B\theta_Z + A\theta_Y\} \quad . \qquad (15)$$

When the blade deformation is zero, this reduces to

$$\cot\alpha_o = AD + BC \quad . \qquad (16)$$

Photographs were taken of the blade tip at zero speed for various values of rotor angle, ϕ. For each of these, the corresponding value of α was measured on the photograph, and the corresponding parameters C and D could be computed. These sets of values were applied to Eq. (16) and used to generate values of A and B that best fit the data. The components of V were measured on blade 10 in the spin rig and the values of A and B were computed to be -.9118 and -.1471 respectively. The corresponding numbers from the data fit were -.9150 and -.1590 respectively, which show good agreement. Without the perspective correction, the values obtained were approximately -.88 and -.33, which confirms that perspective may not be neglected.

Equation (15) in this analysis shows that the angle α may not be used to measure the component of blade rotation θ_Y unless both parameters B and C are negligible. This is not generally the case, and it is practical only to use Eq. (15) together with other knowledge of θ_Y and θ_Z to solve for θ_X. This results in a complete determination of the deformation that may be compared with numerical analysis.

From Eqs. (15) and (16), and since

$$\frac{d}{d\alpha}\cot\alpha = -\csc^2\alpha, \quad \cot\alpha_o - \cot\alpha\chi(\alpha-\alpha_o)/\sin^2\alpha$$

then

$$[A\cot\alpha+D]\theta_Y = (BD-AC)\theta_X+(C+B\cot\alpha)\theta_Z+(\alpha-\alpha_o)/\sin^2\alpha \qquad (17)$$

Applying Eq. (17) to 7,000 RPM conditions as follows:

$\theta_X = -0.108$ rad		(NASTRAN Calculation)
$\theta_Y = 0.0661$ rad	}	Measured from Laser/Mirror data
$\theta_Z = -0.046$ rad	}	extrapolated to tip
$\varphi = -0.047$ rad		(Avg blades 1,2,8,5)

yields a value for $\alpha-\alpha_o$ of 0.0593 rad as shown in Figure 17.

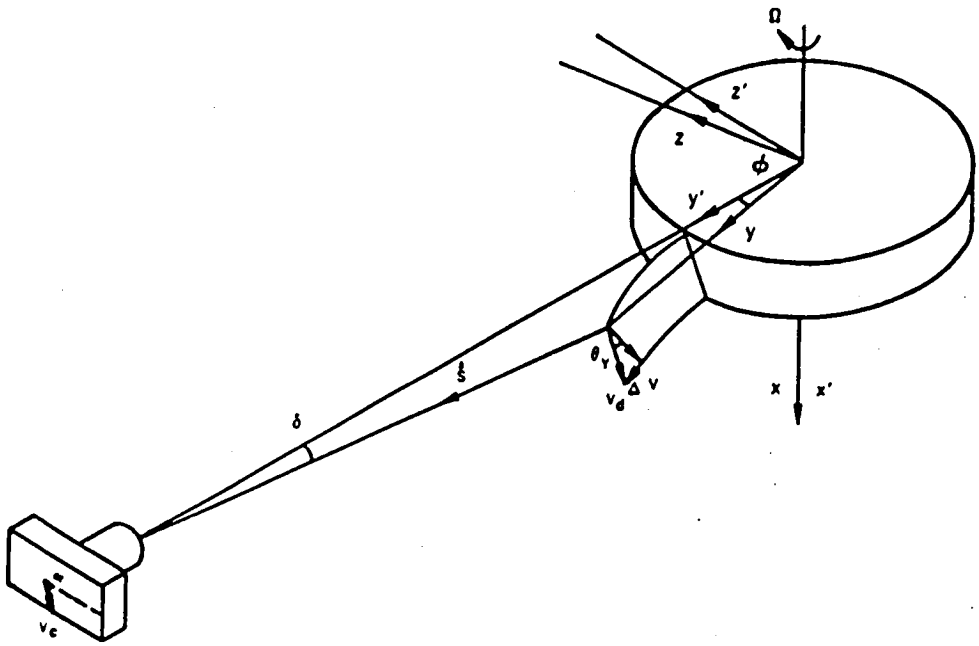

Fig. 2.1 Axis System for Analysis of Tip Photographs

84-4-7-51

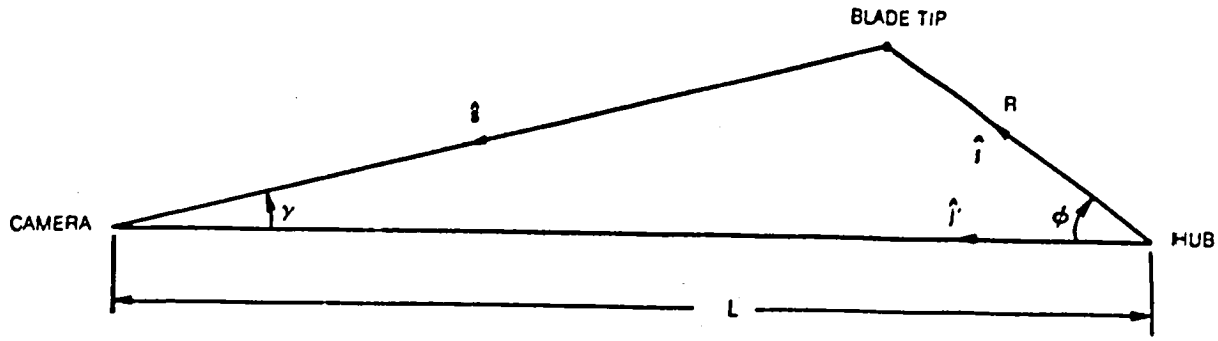

Fig. 2.2 Spherical Perspective Geometry

APPENDIX III

DYNAMIC DATA REDUCTION

As was explained in Section VIII, rotor system dynamic characteristics were recorded during free decay of vibration from an imposed excitation. The identification of modal eigenvalues and eigenfunctions from a digitized time series of strain gage readings was accomplished by an adaptation of the time domain procedure of reference 8. Time Domain Analysis is based on the assumption of a linear system, the free response of which is approximated by the number of modes equal to the number of time steps used in the series. For example, the blade modes of the SR-5 rotor were extracted by selection of data from 12 strain gage outputs. Only 50 of the 1024 time steps were used in a given analysis, consequently, system dynamic properties could be evaluated at several points in the decay.

In the present application, three matrices each 25 x 50 were formed at times, t, $t+\Delta$, and $t+2\Delta t$. For the SR-5 rotor, the 50 time increments covered approximately three cycles of the lowest frequency of interest and approximately twenty cycles of the highest frequency. The delay time, Δt is fifteen time increments. A second delay time $2\Delta t$ is used to enlarge each 12 x 50 array into the 25 x 50 array required, as shown in Figure 3-1.

The time domain forms two 50 x 50 matrices

$$\phi = \begin{bmatrix} X \\ Y \end{bmatrix}$$

$$\hat{\phi} = \begin{bmatrix} X \\ Y \end{bmatrix}$$

and solves the resulting eigenvalue problem

$$\hat{\phi}\,\phi^{-1}\psi_i = e^{\lambda_i \Delta t}\psi_i$$

for the complex eigenvalues λ_i and eigenvectors ψ_i. This problem is closely related to the dynamic eigenvalue problem of the linear system which was assumed as a model, the vectors being identical and the eigenvalues being simply related.

In addition to the modal frequencies, damping factors and normalized complex mode shapes, a modal confidence factor is obtained. This is a measure of the predictability of the actual data from synthesis of the modal structure data fit described above. The modal confidence factor is the ratio of the predicted modal value at a time $2\Delta t$ later to the actual modal data. This complex ratio is expressed as a percent in amplitude and degrees in phase.

$$
X \equiv \begin{bmatrix}
x_t^1 & x_{t+1}^1 & x_{t+2}^1 & \cdots & x_{t+49}^1 \\
\vdots & \vdots & \vdots & \cdots & \vdots \\
x_t^{12} & x_{t+1}^{12} & x_{t+2}^{12} & \cdots & x_{t+49}^{12} \\
- & - & - & - - - & - \\
x_{t+2}^1 & x_{t+3}^1 & x_{t+4}^1 & \cdots & x_{t+51}^1 \\
\vdots & \vdots & \vdots & \cdots & \vdots \\
x_{t+2}^{12} & x_{t+3}^{12} & x_{t+4}^{12} & \cdots & x_{t+51}^{12} \\
- & - & - & - - - & - \\
x_{t+4}^1 & x_{t+5}^1 & x_{t+6}^1 & \cdots & x_{t+53}^1
\end{bmatrix}
$$

$$
Y \equiv \begin{bmatrix}
x_{t+15}^1 & x_{t+16}^1 & x_{t+17}^1 & \cdots & x_{t+64}^1 \\
\vdots & \vdots & \vdots & \cdots & \vdots \\
x_{t+15}^{12} & x_{t+16}^{12} & x_{t+17}^{12} & \cdots & x_{t+64}^{12} \\
- & - & - & - - - & - \\
x_{t+17}^1 & x_{t+18}^1 & x_{t+19}^1 & \cdots & x_{t+66}^1 \\
\vdots & \vdots & \vdots & \cdots & \vdots \\
x_{t+17}^{12} & x_{t+18}^{12} & x_{t+19}^{12} & \cdots & x_{t+66}^{12} \\
- & - & - & - - - & - \\
x_{t+19}^1 & x_{t+20}^1 & x_{t+21}^1 & \cdots & x_{t+68}^1
\end{bmatrix}
$$

$$
Z \equiv \begin{bmatrix}
x_{t+30}^1 & x_{t+31}^1 & x_{t+32}^1 & \cdots & x_{t+79}^1 \\
\vdots & \vdots & \vdots & \cdots & \vdots \\
x_{t+3-}^{12} & x_{t+31}^{12} & x_{t+32}^{12} & \cdots & x_{t+79}^{12} \\
- & - & - & - - - & - \\
x_{t+32}^1 & x_{t+33}^1 & x_{t+34}^1 & \cdots & x_{t+81}^1 \\
\vdots & \vdots & \vdots & \cdots & \vdots \\
x_{t+32}^{12} & x_{t+33}^{12} & x_{t+34}^{12} & \cdots & x_{t+81}^{12} \\
- & - & - & - - - & - \\
x_{t+34}^1 & x_{t+35}^1 & x_{t+36}^1 & \cdots & x_{t+83}^1
\end{bmatrix}
$$

Fig. 3.1 Data Arrays for Blade Modes

84-4-7-40

APPENDIX IV

NASTRAN RESULTS

Charles Lawrence
NASA

NASA Lewis Research Center personnel provided analytical results for SR5 using the finite element program, NASTRAN. These results were obtained to determine the extent of correlation between finite element analysis and experimental tests. The level of correlation between the two approaches is discussed throughout this report. A summary of the NASTRAN steady state displacements, frequencies, and mode shape are presented in this appendix.

The finite element model used for the NASTRAN analysis is shown in Figure 6. This model consists of 882 triangular plate elements (CTRIA3) and 517 node points. The plate element formulations include both membrane and bending action. The base of the blade root is modeled as fully constrained. This constraint does not allow for any coupling that may exist between blades.

NASTRAN Solution sequence 64 was used to compute the blade's steady state displacements produced by the centrifugal loading. Since the turboprop blade is relatively flexible, it responds to loading with relatively large deflections. The computation of these deflections requires a geometrically nonlinear analysis which Solution 64 is capable of performing.

Solution 64 utilizes a modified Newton-Raphson algorithm to solve the geometrically nonlinear problem. The Newton-Raphson algorithm, which is an iterative procedure, required nine iterations to adequately converge. After convergence, the steady state displacements are printed out and the computed structural mass and stiffness matrices are stored for the subsequent frequency analysis. The NASTRAN program is altered so that the centrifugal softening terms, which are normally neglected, are incorporated into the final stiffness matrix.

Figures 4.1 thru 4.6 show the computed blade rotations at the various mirror locations. These rotations can be compared to the experimentally obtained rotations in Figures 1.1 thru 1.7. NASTRAN computed blade displacements in the X and Z direction are shown in Figures 4.7 and 4.8 respectively. The X direction displacements can be compared to the tip photo results in Figure 20.

NASTRAN Solution 63 was used to extract the resonant frequencies and mode shapes from the mass and stiffness matrices generated by the geometrically nonlinear analysis performed in Solution 64. Solution 63 was used for the frequency analysis because it is directly compatible for transferring matrices from Solution 64. The computed frequencies and mode shapes are shown as a function of rotational speed in Figure 4.9.

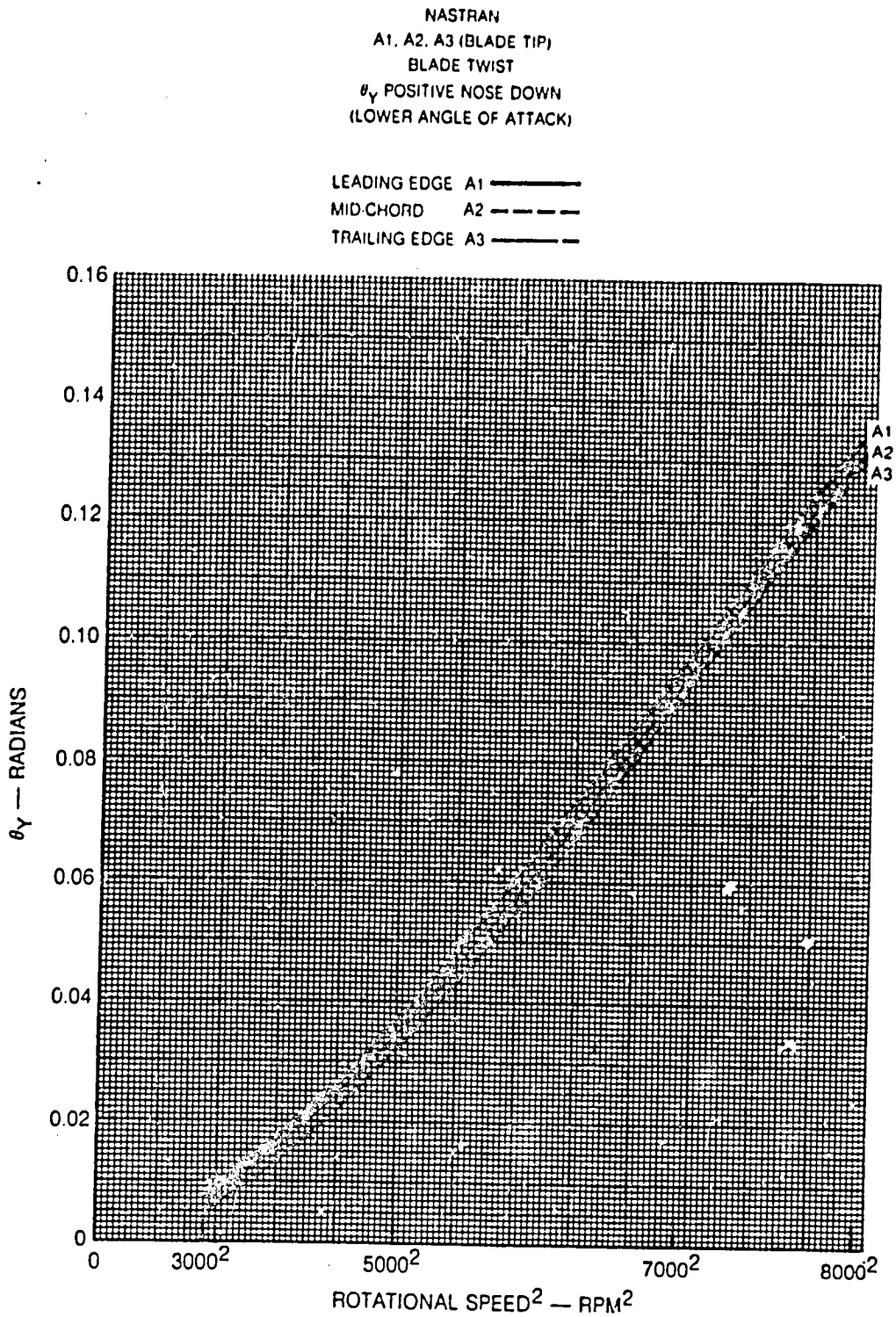

Fig. 4.1 θ_Y vs Rotational Speed^2

84-6-42-1

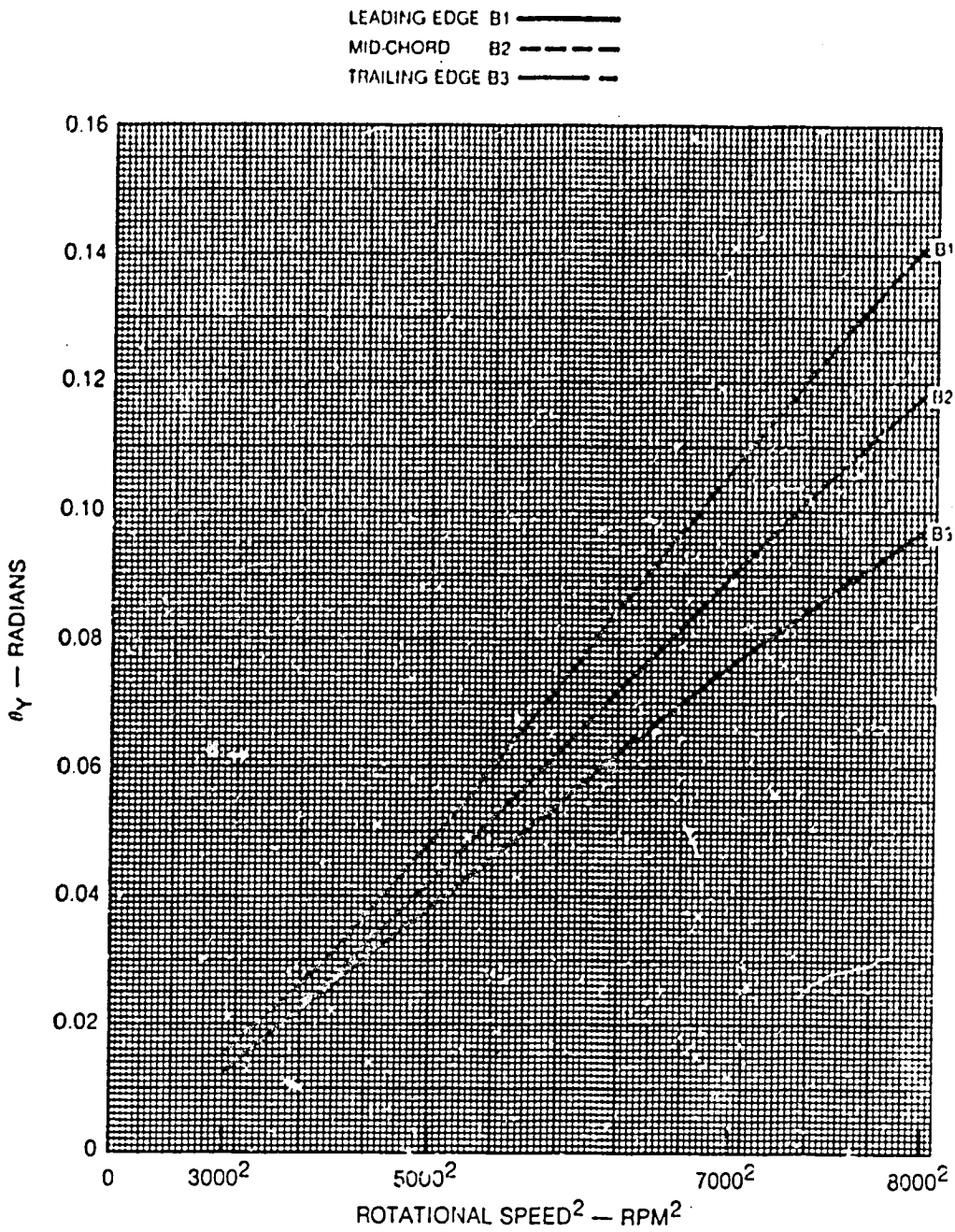

Fig. 4.2 θ_Y vs Rotational Speed^2

84-6-42-2

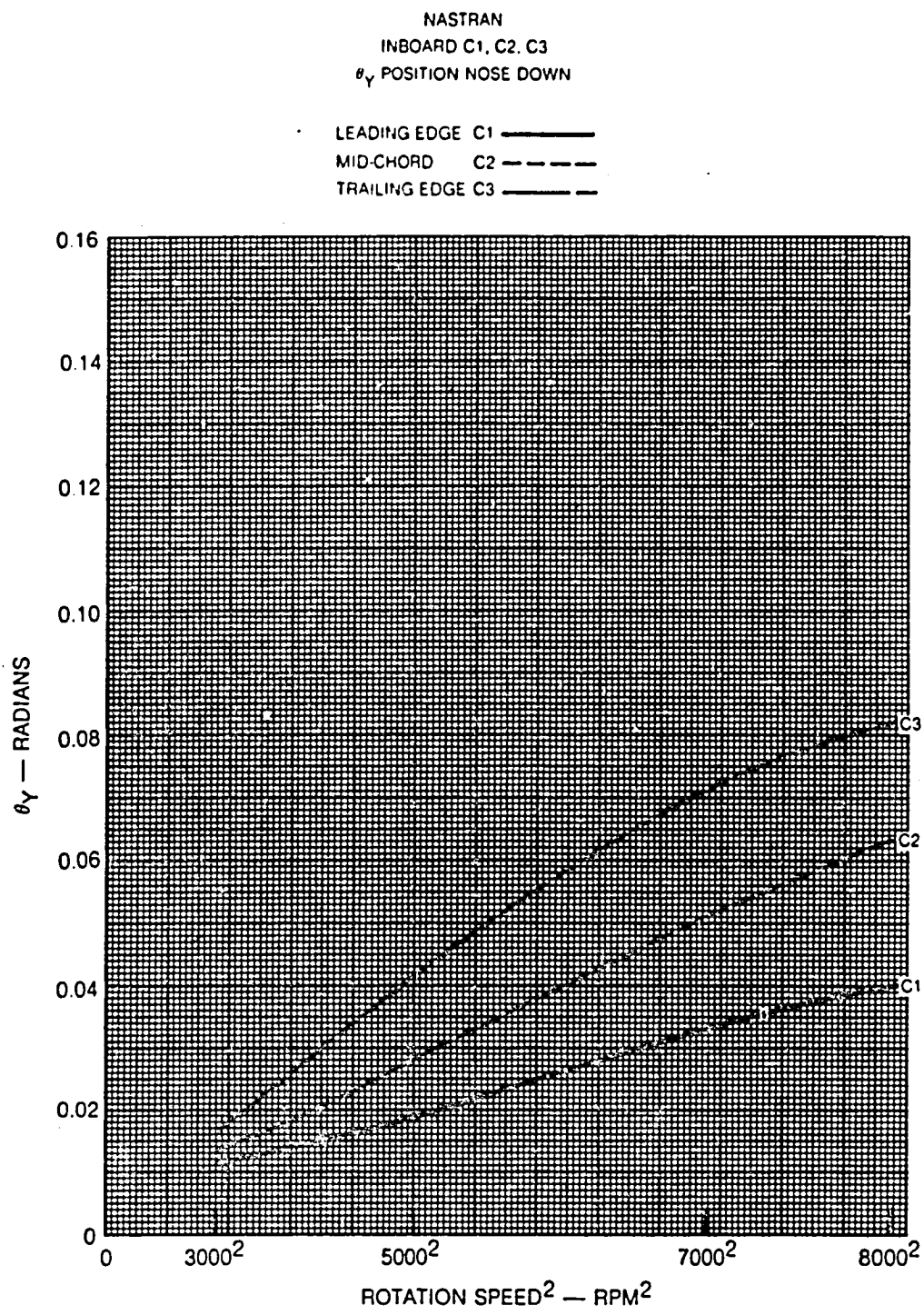

Fig. 4.3 θ_Y vs Rotational Speed^2

C-2

84-6-42-3

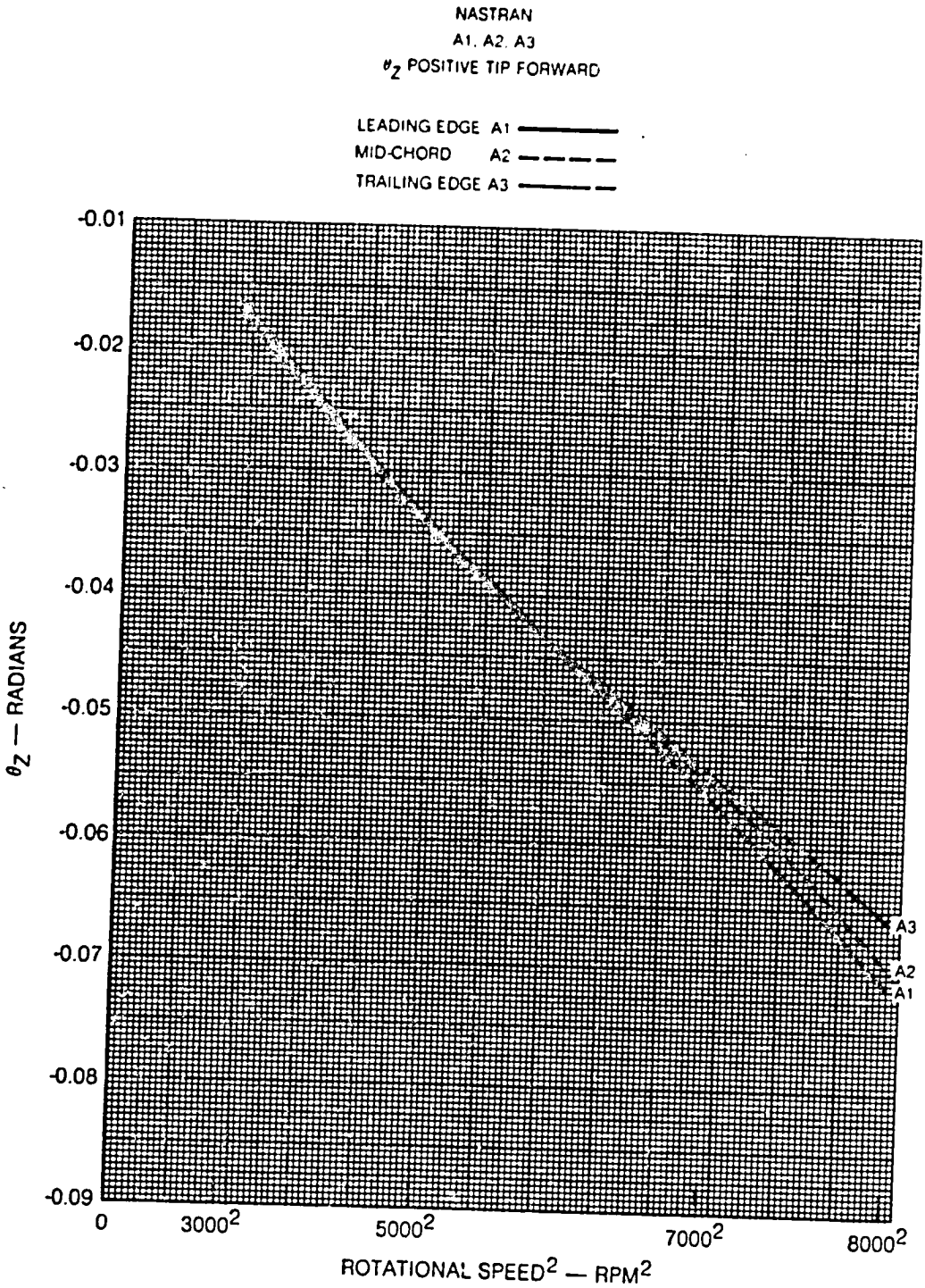

Fig. 4.4 θ_Z vs Rotational Speed^2

84-6-42-4

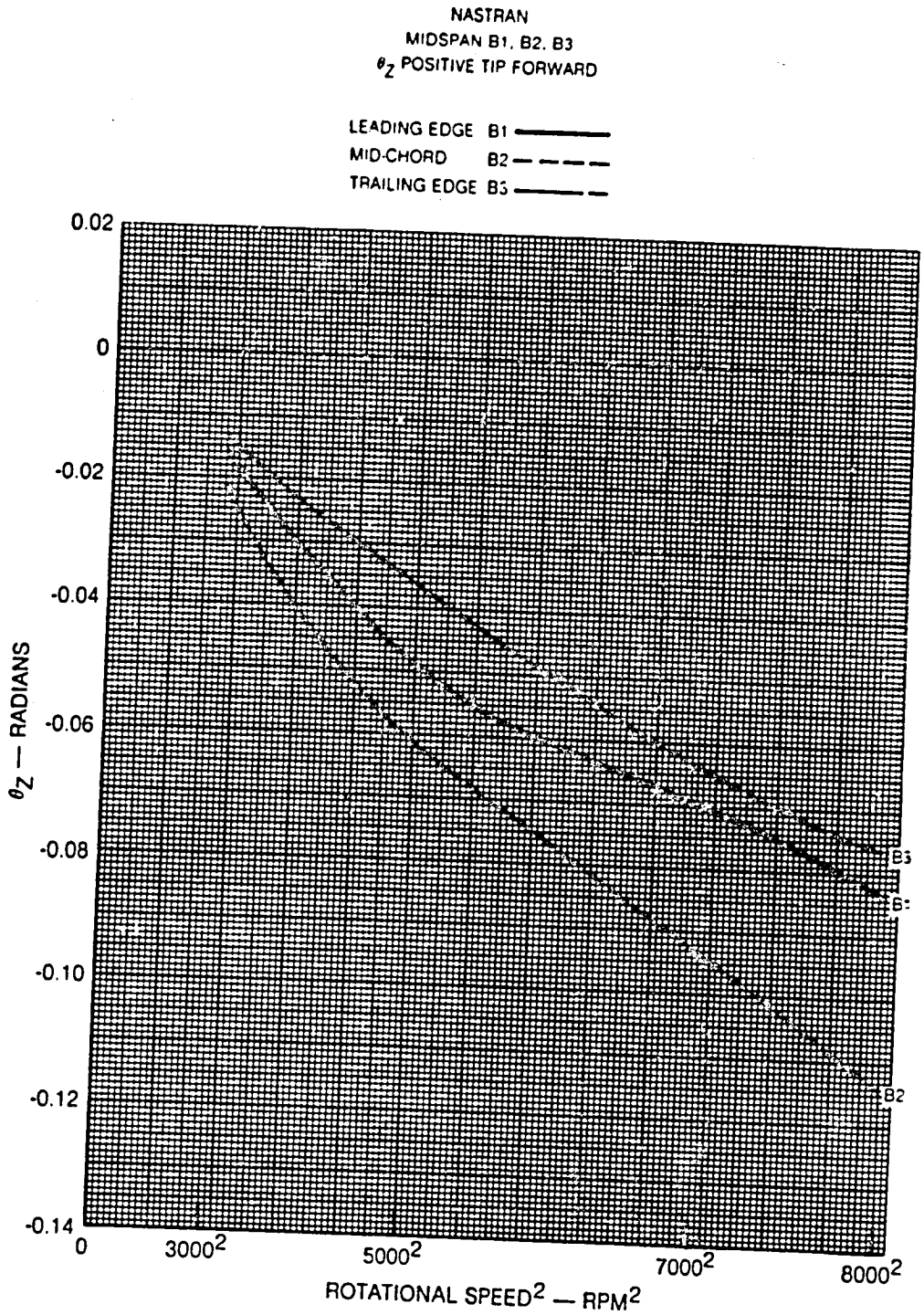

Fig. 4.5 θ_Z vs Rotational Speed^2

84-6-42-5

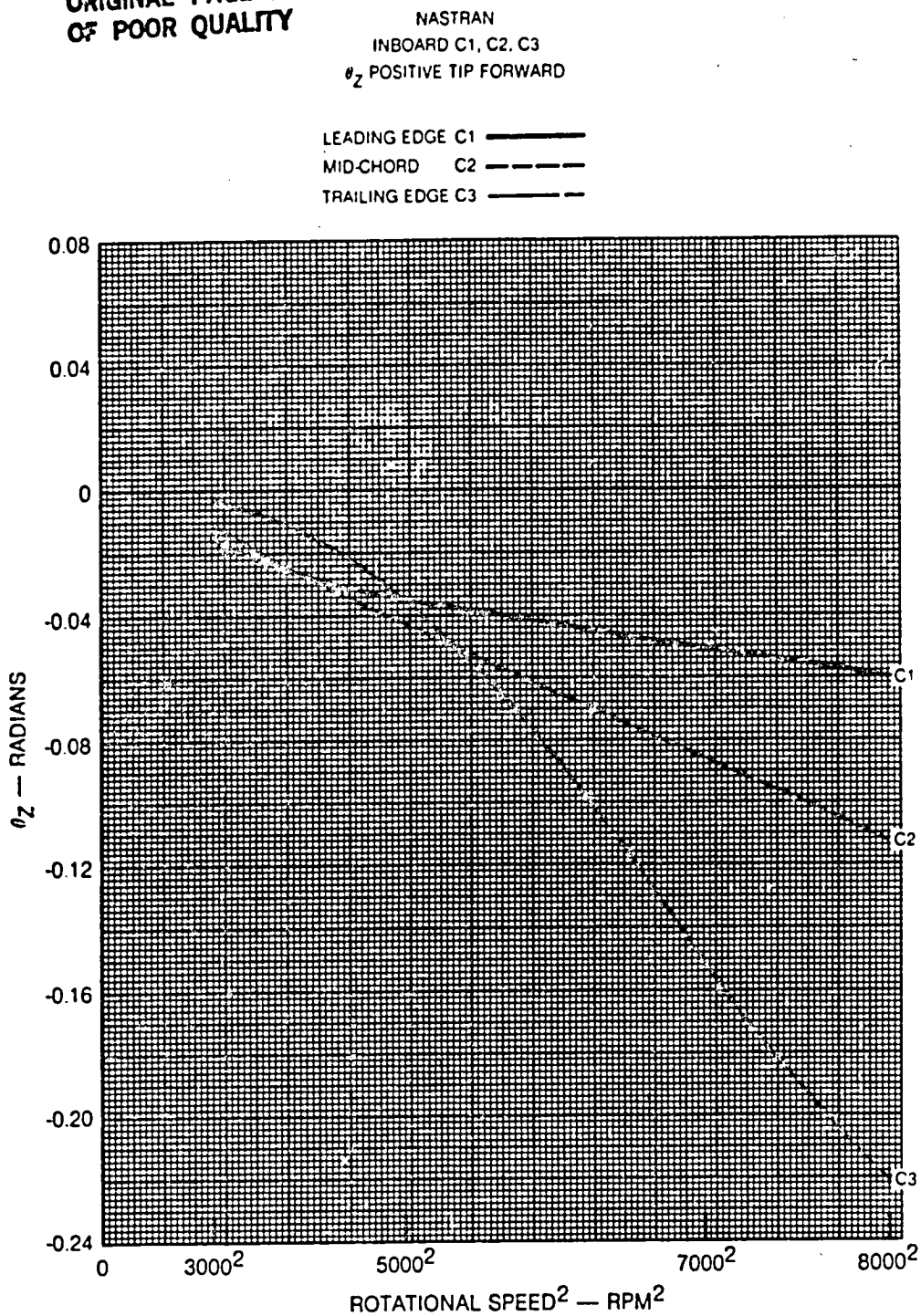

Fig. 4.6 θ_Z vs Rotational Speed^2

84-6-42-6

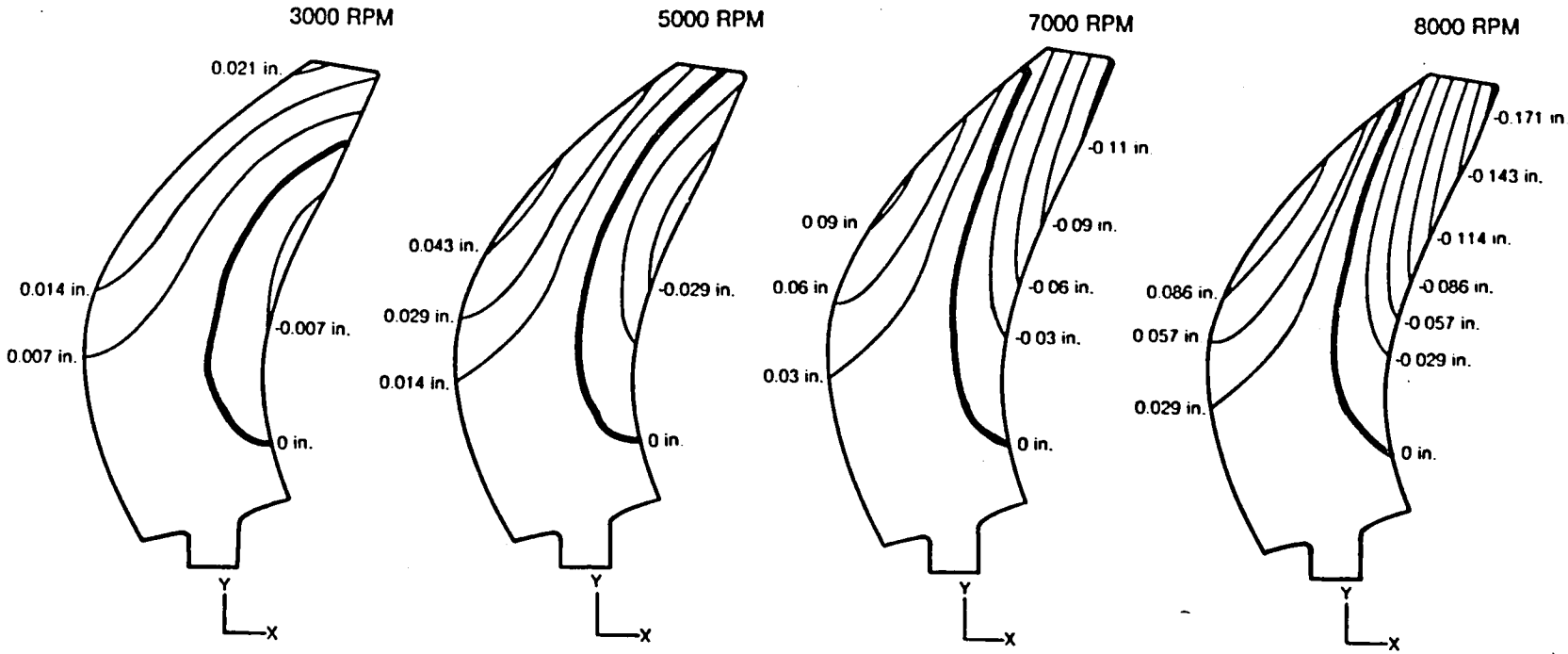

Fig. 4.7 Nastran Displacement Contours X Direction

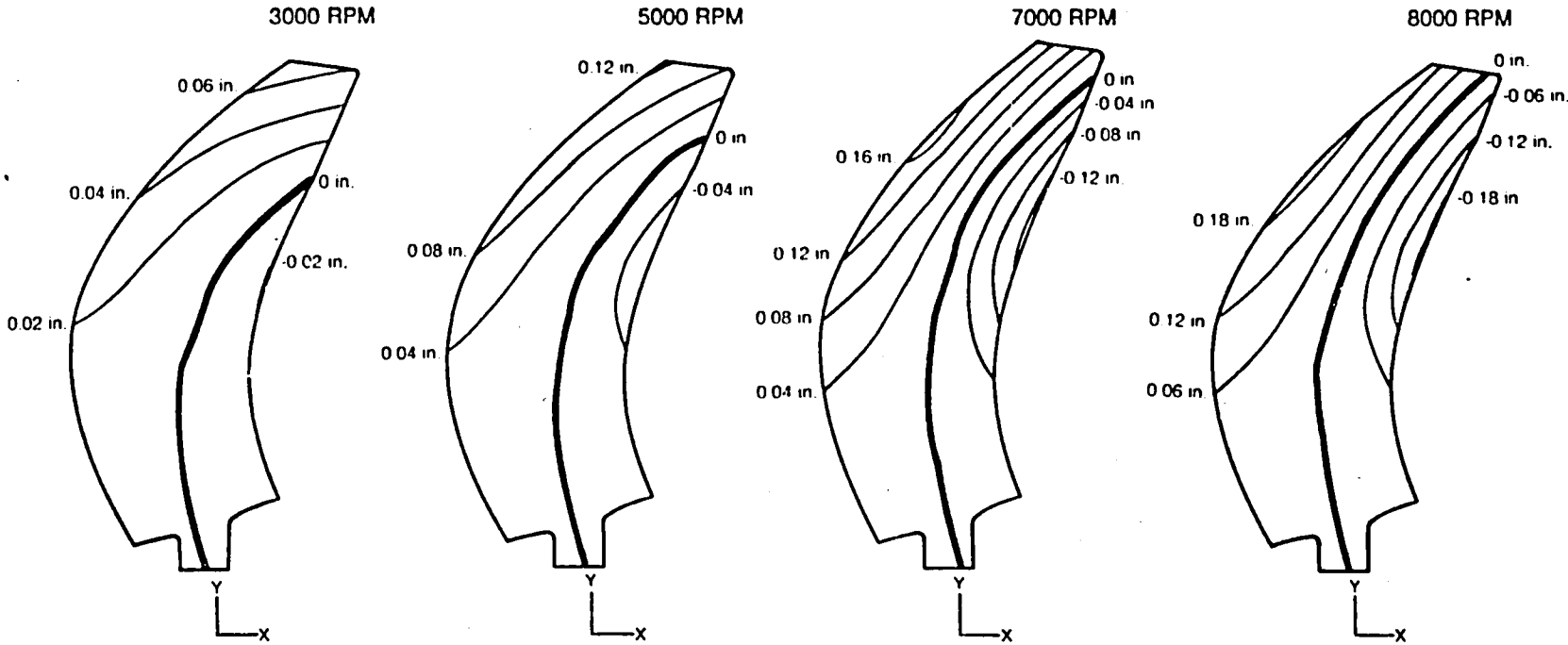

Fig. 4.8 Nastran Displacement Contours Z Direction

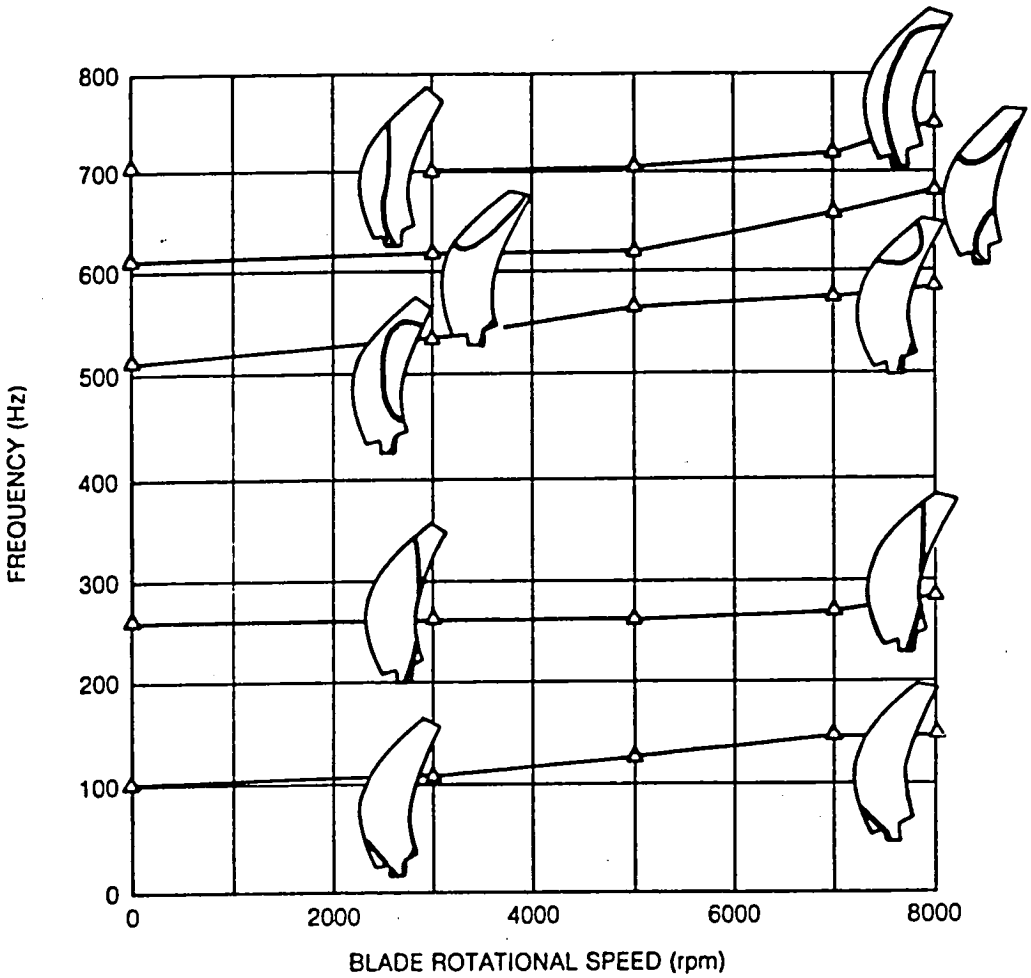

Fig. 4.9 Nastran Frequencies and Position of Node Lines

84-6-42-9

END

DATE

FILMED

JUL 15 1986